ABSTRACT

Title of Document: RFID SENSOR-DRIVEN STRUCTURAL CONDITION MONITORING IN INTEGRATED BUILDING INFORMATION MODELING ENVIRONMENT

Linjia Bai,
Doctor of Philosophy, 2013

Directed By: Yunfeng Zhang, Associate Professor
Department of Civil and Environmental Engineering

Steel structures are very popular structural forms for both buildings and bridges. Under extreme loading such as strong earthquakes or winds, structural members in steel structures could fail in buckling or yielding. In buildings, structural members are often hidden behind fire-proof coating and drywall, and thus buckling or yielding in steel members are very difficult to detect, often requiring removal of coverings and thus time consuming and costly. Fast and accurate assessment of damage conditions is important to the occupant safety and uninterrupted use. This research presents a method for integrating Building Information Modeling (BIM) and Radio Frequency Identification (RFID) based wireless strain sensor technologies to enable automated structural condition assessment. BIM can serve as an ideal 4-dimensional graphical computing environment for integrating structural health monitoring (SHM) with management practice, which often involves considerable amounts of sensor data of different modalities and changes of structural condition over time. To detect the

exceedence of preset threshold strain levels, this research custom designed a novel breakage-triggered (BT) strain sensor for detection of threshold strain levels. This BT strain sensor uses RFID tag for wireless communication with RFID reader. With a special design, the sensor breaks at pre-set strain level and the connected RFID tag is activated. By altering its configuration to include multiple threshold strain levels, actual strain at the monitored location can be estimated after hazardous events. This system can rapidly identify and locate the spot where pre-set strain or crack has happened and the corresponding structure element of the BIM model is automatically highlighted to provide alert signal. Such damage spots require immediate action after hazardous events such as earthquake or extreme wind. The RFID tag can be scanned from a distance up to several meters by using an RFID reader. This system is highly automated, low power consumption, and low cost.

A custom developed middleware was developed to enable automated sensor data entry into BIM environment and thus avoid possible human related errors. The BIM environment allows for capturing, organizing, processing (cleansing, fusion, mining, etc.), visualizing the sensor data from the monitoring system, updating relevant models and running finite element analysis for structural response and reliability computation as well as structural health prognosis. Process (inspection scheme) and work-flow automation can be realized. Therefore, the proposed method would lead to more user-friendly, highly automated and more economical way for structural condition assessment and SHM information management.

RFID SENSOR-DRIVEN STRUCTURAL CONDITION MONITORING IN INTEGRATED BUILDING INFORMATION MODELING ENVIRONMENT

By

Linjia Bai

Dissertation submitted to the Faculty of the Graduate School of the
University of Maryland, College Park, in partial fulfillment
of the requirements for the degree of
Doctor of Philosophy
2013

Advisory Committee:

Associate Professor Yunfeng Zhang, Chair/Advisor

Professor Amde M. Amde

Professor M. Sherif Aggour

Research Professor Chung C. Fu

Professor Sung W. Lee

Acknowledgements

The research presented in this dissertation was conducted at Department of Civil and Environmental Engineering, University of Maryland, College Park, Maryland.

I would like to take this opportunity to express my sincerest appreciation to my advisor, Dr. Yunfeng Zhang, who has always provided guidance and direction to me. And I also appreciate the contributions of my other committee members, Dr. Amde M. Amde, Dr. M. Sherif Aggour, Dr. Chung C. Fu and Dr. Sung W. Lee.

I would also like to express my gratitude to Department of Civil and Environmental Engineering for providing me with the great experience of teaching assistantship, and for the Structural Engineering Laboratory facilities in which the experimental tests of this study were conducted.

Financial support from National Science Foundation and US Department of Transportation's RITA Program is greatly appreciated.

My friends, Zhen Li, Changjiang Zhou, Feng Shi and Ruipeng Li have been very helpful to me during my study. I would like to extend thanks to my friends at University of Maryland.

Finally, I am deeply indebted to my family without whom I would never have accomplished my study. I cannot be grateful enough for their support. This dissertation is dedicated to my parents, Suqi Bai and Yuan Zhang, my dear wife, Hua Ge and my daughter, Emilly Bai.

Table of Contents

List of Tables

List of Figures

Chapter 1: Introduction

1.1. General

There is a strong and growing interest in on-line structural health monitoring (SHM) systems among engineers, researchers, and decision makers in civil engineering applications. On-line SHM enables automatic collection of vital information about civil infrastructures' operating condition and in the aftermath of a catastrophic event such as strong earthquake, its ability to continue to carry the design load. Sensor data from SHM systems provides the base data for real-time updating of the structural condition and reliability. For example, probabilistic health prognosis method uses sensor data for system reliability updating, which can then be utilized for risk analysis and maintenance scheduling of engineering systems. However, the incompatibilities in user interface, data format, and computing environment in many current (mostly custom built) SHM software applications make it difficult if not impossible for most users to take advantage of the full set of resources available for SHM. With emerging monitoring system featuring continuous and online data collection, 3-dimensional graphical computing environment needs to be developed to enable effective communication of information between users at different levels in sensor-driven SHM practice.

BIM has seen increasing popularity and implementation in the construction industry to produce data-rich models of buildings and structures (Wong *et al*. 2011; Eastman *et al*. 2011). In the USA, several government agencies including General Services

Administration (GSA) have been actively promoting the BIM implementation for all major projects (GSA 2007). The U.S. GSA began using BIM in 2003. In July 2009, the state of Wisconsin issued guidelines to AE firms requiring the use of BIM on all projects totaling more than $5 million and new construction projects of more than $2.5 million (Beck 2012). BIM provides an integrative visual platform for information exchange between different modules of the system as well as a shared, coordinated repository for the structure's lifecycle information. This addresses the needs for improvement in structural condition monitoring/assessment productivity, especially after hazardous events, when resources such as experts and timeline requirement are tight. The models are continually updated to reflect project-related adjustments. Accurate and comprehensive information, such as the digital information from a BIM model about a structure, its construction, its life-cycle maintenance and loading data, can be very beneficial to SHM and decision making in infrastructure operation. Therefore, BIM model can be leveraged as an integrative platform for other professional services such as sensor-driven SHM applications.

This chapter presents the background information related to BIM with SHM system. It is followed by the motivation and objectives of the research and the organization of the dissertation.

1.2. Objective

This research aims to integrate the RFID and BIM technologies with SHM for an automated and graphical approach to structural condition monitoring, prognosis and health management to facilitate the implementation of resilient structure concept.

Ability of rapid structural condition assessment after major hazardous events reduces the time to recovery and thus increases the resilience in disaster recovery. SHM is a cross-disciplinary field of emerging importance that involves different disciplines such as structural analysis, sensor technology, data fusion, and etc. In the past, ad hoc SHM systems with custom developed virtual user interface have been built for a variety of projects. Thus lack of universal virtual user interface and computing environment poses an impediment to wide adoption of SHM system and unnecessarily increases the cost to build SHM system for a project. BIM presents itself as a perfect solution to address this need. Many important infrastructure projects already have BIM model right from the start of the project design and construction phase; the availability of such BIM models can be taken advantage of by integrating the BIM with sensors and SHM technologies. BIM can integrate all types of condition assessment information collected in the life cycle of civil infrastructures. For example, information about sensors and monitoring equipments - model number, specification data, calibration history, can be readily accessed by selecting an object in the BIM model. The data displayed will reside and be maintained in a database. In this graphical computing environment, SHM data can be shared in the BIM environment with other disciplinary applications in the infrastructure's life cycle. There are many issues that come along with this new capability and the key modules for a functional BIM computing environment for SHM application are examined in this research. Specifically, the proposed BIM for SHM portal is linked to a database, finite element analysis software, providing the visual data displaying mechanisms that make the SHM information easily understandable and actionable.

1.3. Dissertation organization

The dissertation is organized into eight chapters including this introduction chapter. The other seven chapters are organized as follows.

- Chapter Two briefly introduces the concept and characteristics of BIM, followed by a review of current adoption of BIM in Architecture, Engineering, and Construction (AEC) Industries and current research in RFID assisted BIM technology. The potential of integrating BIM with RFID based wireless sensor and SHM as well as the challenges and important issues in their integration are discussed. A general framework for sensor-driven SHM integrated into the BIM environment is presented in this chapter.
- Chapter Three presents a novel breakage-triggered (BT) strain sensor for detection of preset threshold strain levels. The BT strain sensor uses RFID tag for wireless communication with BIM-based SHM software program via a RFID reader device and a custom developed middleware. The principle of operation for the BT strain sensor is described and finite element (FE) analysis results is presented to gain insight on how to tune the design parameters to optimize its performance in strain sensing. The performance of the BT strain sensor is validated and characterized with experimental tests. Different threshold strain levels can be set to the BT strain sensor design by adjusting the geometry and size of the brittle bar in the sensor. Two types of brittle materials, acrylic sheet and epoxy paint, were tested for use in the BT strain sensor. Additionally, use of epoxy paint patch to detect local buckling in steel structures was explored in this study and pilot test results are presented

in this chapter. The BT strain sensor will be incorporated into the wireless structural condition assessment (WSCA) system to provide information on structural damage conditions such as yielding or buckling. In this chapter, the sensor technology components part of the BIM based WSCA system is established.

- Chapter Four provides an overview of the sensor-driven SHM integrated into the BIM environment. Integration of various SHM components including RFID based sensors, FE analysis, database, condition assessment and interaction between these components are discussed in detail. Although many BIM software programs are available on the market for which the proposed framework can be equally well applied, Revit Structure is selected in this research to demonstrate the proposed technology. A case study of highway steel bridge located in Maryland is presented to illustrate the different aspects of the sensor-driven SHM system integrated into the BIM environment. This chapter focuses on the software part of the proposed WSCA system.
- Chapter Five is related to the concept of resilient structure design by concentrating SHM on fuse members. New design trends for seismically resilient structure is to incorporate fuse members into structures so that only fuse members are to be damaged while other parts of the structure remain linear elastic during strong earthquakes. This resilient structure design is also appealing to SHM since condition assessment or monitoring work can now be focused on a limited number of fuse members instrumented with dense sensor networks. A steel arch truss with strategically selected fuse regions under

earthquake is used as a prototype structure to demonstrate that damages could be concentrated within pre-selected damage zone to facilitate efficient condition assessment.

- Chapter Six presents a hybrid test study on a truss structure to validate the WSCA system in a more realistic working condition. Test of BT strain sensor on a PVC tube before the hybrid test was first conducted to validate the sensor and debug any potential problem associated with implementing the BT strain sensor on a tubular member. In the hybrid test, the hardware and software components of the WSCA system were examined for their performance (individual and interaction) as a whole.
- In Chapter Seven, the concept of resilient structure with focused SHM enabled by implementing the WSCA system is demonstrated using an eccentrically braced frame (EBF) building as a prototype structure. In EBF, shear links are considered as the fuse members that will develop large plastic deformation to provide the desired level of ductility and energy dissipation. To guide the design of BT strain sensors in the WSCA system implemented into the shear links, nonlinear time history analysis of EBF as well as FE analysis of shear link with BT strain sensors were performed. A reduced-scale shear link specimen was tested to validate and characterize the performance of the WSCA system in steel structures.
- Lastly, Chapter Eight presents a summary of the research, conclusions and recommendations for future research work.

Chapter 2: BIM for Structural Health Monitoring (SHM)

2.1. Introduction on BIM

The concept of Building Information Model (BIM) has existed since the 1970s (Eastman at al. 1974). The term BIM first appeared in a paper by van Nederveen *et al*. (1992). According to the National BIM Standards Committee (NBIMS 2007), BIM's overall scope is broad and can be described within the relations of three categorizations: (1) BIM as "a product" of digital representation of physical and functional characteristics of a facility; (2) BIM as "a collaborative process" which covers business drivers, automated process capabilities, and open information standards use to information sustainability and fidelity, and (3) BIM as "a facility lifecycle management tool" of well understood information exchanges, workflows and procedures.

Traditional building design was largely reliant upon two-dimensional drawings (plans, elevations, sections, etc.). BIM extends this beyond 3-D, augmenting the three primary spatial dimensions (width, height and depth - X, Y and Z) with time as the fourth dimension and cost as the fifth. BIM therefore covers more than just geometry. It also covers spatial relationships, light analysis, geographic information, and quantities and properties of building components.

A three-dimensional model of building geometry alone that is used only in visualization is usually not a BIM (Bazjanac 2004). BIM involves representing a design as combinations of "objects" – vague and undefined, generic or product-

specific, solid shapes or void-space oriented (like the shape of a room), that carry their geometry, relations and attributes. Building components are represented with digital "objects" that carry computable graphic data attributes. BIM design tools allow extraction of different views from a building model for drawing production and other uses. Building models are consistent and non redundant such that changes to component data are represented in all views of component and the assemblies. Parametric object is an important concept in BIM. The objects in BIM are defined as parameters and could be modified and related to other objects parametrically. If one object is modified, other related objects will also update automatically according to their defined relations (Eastman *et al*. 2011).

2.2. Current use of BIM in Architecture, Engineering, and Construction (AEC) industries

The Architecture, Engineering and Construction (AEC) industries have long sought techniques to decrease project cost, increase productivity and quality, and reduce project delivery time. BIM offers the potential to achieve these objectives (Azhar *et al*. 2008).

Most complex projects in the AEC industries involve multidisciplinary collaboration and the exchange of large building data set. Traditionally, the collaboration efforts across the disciplines have been based on the frequent exchange of 2D drawings and documents. However, during the past decade, the widespread adoption of object-oriented Computer-aided Design (CAD) tools has generated more interests in BIM. A number of BIM-compliant applications such as analysis tools, model checkers and facility management applications are being developed (Singh *et al*. 2011).

Typically, the inter-disciplinary collaboration in ACE industries has revolved around the exchange of 2D drawings and documents. Even though the separate design disciplines have been using 3D models and applications for visualization and design development, the collaboration practices have remained more or less 2D-based until recently (Singh *et al*. 2011).

The current application of BIM in the AEC industries includes: 3d visualization; fabrication/shop drawings; code reviews; cost estimating; construction sequencing; conflict, interference, and collision detection; forensic analysis; and facility management (Azhar 2011).

2.3. Current research on RFID assisted BIM technology

RFID based systems have been used in different applications in construction and maintenance, such as component tracking and locating, inventory management, equipment monitoring, progress management, facilities and maintenance management, tool tracking and quality control (Motamedi and Hammad 2009).

The use of attached RFID tags for lifecycle ID and data management in the aerospace sector has been proposed by Harrison and Parlikad (2006). The information to be stored includes unique ID and important lifecycle information on tags attached to aircraft parts for enhancing inspection and repair processes. They demonstrated that the RFID enable more efficient and complete data capture in various maintenance processes, with the benefit of reducing human error, and also generating information in electronic format for record-keeping and further analysis (Harrison and Parlikad, 2006).

Ergen *et al*. (2007) proposed using RFID tags attached to engineered-to-order (ETO) components and explored the technical feasibility of such system by analyzing component-related information flow patterns in ETO supply chains. Their experiments demonstrated that it is technically feasible to have intelligent components in construction supply chains by using RFID technology; that status information can be collected automatically; and that maintenance information can be stored and retrieved during the service life of a facility.

Motamedi and Hammad (2009) proposed permanently attaching tags to components in the manufacturing stage as an integrated part of the components. Having the tags permanently attached, where the information on the tags is gradually updated with accumulated lifecycle information, is beneficial for all the stakeholders throughout the stages of the lifecycle, from procurement and supply chain management to maintenance and disposal. They also proposed to include broader data types on the RFID tags that are attached to building components and are spread in a building. In the proposed approach, the information on the tags represents chunks of the BIM as a distributed database. This coupling between the BIM and the RFID information would allow reconstructing the database of the BIM (or part of it) based on the pieces of information distributed in all the attached tags.

2.4. Potential of integrating BIM with SHM

The advantages of 3D graphical display and model digitization make BIM a promising computing environment for integrating different components of an SHM system. The potential issues in the integration process are discussed next.

An interchangeable data format becomes an important prerequisite for BIM-SHM integration due to the intensive need of data exchange in an SHM system. However, poor software interoperability has long been regarded as an obstacle to industry efficiency in general and to BIM adoption in particular (Wikipedia 2013).

Isikdag *et al*. (2007) summarized five storage, sharing and exchange methods for different BIM models: (1) Data exchange by using physical file; (2) Data sharing through application programming interfaces (APIs); (3) Data sharing through central project database; (4) Data sharing through federated project database, and (5) Data sharing by web services.

The problems of interoperability between engineering software systems have existed since the introduction of computer-aided design (CAD) in the 1970s (Pratt 1993). File-based data exchange methods such as DXF, IGES, and SAT were developed to exchange geometric entities between one CAD system and another. However, as CAD systems became more sophisticated and evolved into parametric and object-based modeling, the limitations of existing file-based methods became apparent. Parametric modeling involves rules and constraints that define how shapes are to be generated or modified in various conditions; CAD systems became object-based and included attributes and relations between objects as well as geometry (Light and Gossard 1982). There was no standard way of representing these aspects with existing geometry exchange standards (Eastman *et al*. 2010).

IFC format is one of the open standards, which was developed by BuildingSMART (the former International Alliance for Interoperability (IAI)). In September 2007 the

Charles Pankow Foundation awarded the Applied Technology Council (ATC) a research grant for the development of Industry Foundation Classes (IFCs) for the structural domain (ATC-75 project). The goal of the ATC-75 project (ATC 2013) was to develop a basis for incorporating and integrating structural design parameters, codes, analysis tools and methods into the Industry Foundation Class (IFC) data model, an open-source object-oriented exchange language (file format) that is being developed by the IAI for Building Information Modeling (BIM) software (ATC 2013). Its main purpose of IFC is to provide CAD users with the ability to exchange data between different CAD softwares. The IFC provides a set of definitions for all object element types and a text-based structure for storing those definitions in a data file.

To implement the IFC standard, the individual CAD software has to provide a command to export/import IFC format files so that could enable data exchange between them. Unless each information exchange within the project workflows has its specific contents and level of detail defined, the breadth and flexibility of the IFC schema leaves room for errors (Eastman *et al*. 2010). The IFC is so far the most promising standard for inter-platforms data exchange in BIM industry. Part of the reasons for this is because it uses a plain text file (.txt file), the only truly universal computer data format (Goldberg 2003).

Despite all this, there are still some barriers that make integration between BIM and SHM has not been fulfilled yet. IFC takes a lowest common dominator approach to BIM. So even though some BIM software has IFC certified importers and exporters, there is invariably a loss of data fidelity (Golabchi and Kamat 2012). No single IFC

adapter could be developed to connect all the software in SHM system. For specific software, an IFC adapter has to be developed to fit its complex architecture. It's rather inconvenient for SHM end users to develop IFC adapter and incorporate it to each software components in the SHM system.

The results of the IFC, on the other hand, have been difficult to implement and utilize because the use cases in which exchanges are to be made have not yet been clearly defined. For a building model framework schema such as IFC, lack of definition of specific task-oriented exchange content leads to implementation of translators that may be technically correct, but generate incomplete and incompatible data exchanges for specific tasks, because of lack of coordination regarding what specific information is to be included in the IFC (Eastman *et al*. 2010).

A proposed solution to these problems is to define the workflows used in practice, the specific information exchanges they require, and define appropriate model views for the exchanges. The national BIM standard (NBIMS 2007) approach for resolving the incompatible event of information exchange is based on "use cases", which precisely define the data required in each information exchange between disciplines in engineering workflows (Eastman *et al*. 2010). The details of use case approach could be found in NBIMS (2007), administered by BuildingSMART within the National Institute of Building Sciences (NIBS). According to this "use case" approach, in the case of BIM-SHM integration, the SHM industry specialists who know the workflows and their information flows required for information technology exchange could write appropriate export and import translators for their softwares.

Following the NBIMS "use case" approach, a middleware program termed as BIM for SHM portal was developed in this study following a structure similar to that of Isikdag *et al*. (2007). The middleware program utilizes the Autodesk Revit API to access the BIM database and automatically update and store SHM data in a database such as Microsoft Access. The details of this BIM for SHM portal can be found in Chapter 4.

Chapter 3: Breakage-triggered (BT) Strain Sensor for Detection of Threshold Strains

3.1. Introduction

Strain measurement is essential to the condition assessment of structures since structural members are usually designed to work under a certain strain level to prevent overloading. A structural health monitoring (SHM) system should generate an alarm signal whenever the strain exceeds this limit. Furthermore, ductile seismic design emphasizes utilizing the inelastic deformation capacity of some structural members (e.g., fuse members) to provide the desired ductility and energy dissipation. Therefore, after earthquake, knowing the actual strain sustained by these deformation-controlled structural members is critical to judge their remaining ductility capacity. Strain measurements over a pre-specified level usually suggest a limit state is likely to be reached locally and engineers needs to be immediately alerted for timely action.

Several types of sensors are available for strain measurement including metal foil strain gage, vibrating wire strain gage, fiber optic sensors, and etc. However, these strain sensors require power supply and signal conditioning circuit to operate. Moreover, with the growing use of steel-concrete composite structures in high-rise buildings and bridges, strain monitoring of the steel member embedded in concrete or hidden behind fire-proof coating or drywall poses new challenges for conventional strain sensor technologies. Acquiring data from these strain sensors often requires time-consuming setup procedure, which might hinder the post-earthquake condition

assessment process. In addition, power blackout is very likely to happen during earthquakes, limited power from accompanying battery poses another service challenges since they have to be checked frequently to ensure proper function in the next earthquake event.

To address the above need for embeddable sensors that can operate without power supply, a passive wireless, low-cost breakage-triggered (BT) strain sensor for detection of threshold strains is proposed and its performance is characterized in this chapter. This BT strain sensor uses RFID (radio frequency identification) technology in wireless communication with BIM-based SHM software program and requires no power in detecting the threshold strain level experienced by the structural members. The principle of operation of the BT strain sensor and results of experimental demonstration are discussed in this chapter.

3.2. RFID-based strain sensor: overview

Among many new SHM technologies, wireless sensing can help to significantly reduce instrumentation time and system cost (Lynch and Loh 2006). Such wireless sensors often require battery to supply the power.

In recent years, Radio frequency identification (RFID) has received growing attentions for its fast development in many fields such as asset management, access control, transportation and logistics. Because of its passive wireless feature, researchers (e.g., Yi *et al*. 2013) are also looking into its potential to incorporate RFID technology into passive wireless strain sensors. Three types of such RFID-based strain sensors are shown in Figure 3-1. A passive wireless antenna sensor based

on RFID technology was recently developed by Yi *et al*. (2013) for strain and crack sensing. In the device developed by Yi *et al*. (2013), when the antenna experiences deformation, the antenna shape changes, causing a shift in the electromagnetic resonance frequency of the antenna. A radio frequency identification (RFID) chip is adopted for antenna signal modulation, so that a wireless reader can easily distinguish the backscattered sensor signal from unwanted environmental reflections. The RFID chip captures its operating power from an interrogation electromagnetic wave emitted by the reader, which allows the antenna sensor to be passive (battery-free). Some other wireless passive strain sensors have also been proposed based on inductive coupling between two adjacent inductors (Butler *et al*. 2002; Loh *et al*. 2008; Jia *et al*. 2006; Daliri *et al*. 2012). The interrogation distance achieved by inductive coupling is usually limited to several inches, which is inconvenient for practical applications. Because of the large scale in civil infrastructures, many locations are either inaccessible or difficult to reach.

Morita and Noguchi (2008) developed a crack detection sensor using RFID tag and electrically conductive paint or printed sheet. When a crack occurs, the paint or printed sheet is broken, resulting in an increase in resistance. Crack width can be estimated by the ability of an RFID reader to communicate with the RFID tag. The crack detection sensor was experimentally studied by bending test of a concrete beam.

Chin *et al*. (2009) developed a gage which is embedded into a passive RFID tag, so that its status can be queried by a nearby RFID reader. Their RFID tag consists of an antenna loop and a small microchip containing a small amount of information. The

conductor bar is broken when significant cracks form across a gage. Communication with the tag attached to the gage is then lost. The loss of communication is reported to indicate the presence of the cracks.

Yi *et al*. (2011, 2013) developed strain and crack sensors using an RFID-based folded patch antenna. They found that when strain stretches the patch antenna, the antenna's electromagnetic resonance frequency changes accordingly. They did experimental study to correlate the change in the antenna's electromagnetic resonance frequency to the crack width on the structure element so that the crack length could be obtained by the change of resonance frequency. The resonance frequency change can be interrogated and recorded by an RFID reader.

RFID technology operates on the basis of radio-frequency electromagnetic field to wirelessly (up to several meters away) interrogate an RFID tag which contains electronically stored information. Each RFID tag is assigned a unique ID, which makes it popular for identification applications such as asset management. Most notable is that the RFID tag does not need to be within the line of sight of the RFID reader and can be read through many non-metallic materials (Shepard 2005, Glover 2006). An RFID tag reading penetration test has been reported by Morita and Noguchi (2008), in which several fire-resistant materials were tested, such as pearlite board, rock wool board, and ceramic wool. The maximum readable distance varies depending on material thickness, although all materials allow tags to be read up to a distance of 100-110 cm (Morita and Noguchi 2008).

In choosing the proper type of RFID hardware for strain sensing or crack detection, a few key parameters including the read range and data transfer rate should be evaluated. In this study, the read range of the prototype RFID tag is the first and foremost important parameter to consider. The maximum read range depends on a variety of factors including the output power of RFID reader, antenna type and size, working frequency range and environmental factors. Because of civil engineering structures' large scale, wireless interrogation of RFID tags installed on the structures is often desired, especially for locations difficult to access. Therefore, RFID tag that can be interrogated from a distance of several meters is preferred for this application. Additionally, the ease of modifying the tag antenna for impedance adjustment is also taken into account. UHF RFID has a greater read range and broader working frequency range. Therefore, UHF RFID tag suffers less effect when more than one tag needs to be read at a time. Considering all these issues in selecting the RFID tag, a UHF RFID tag (model #: Avery AD-224 RFID tag) has been selected in this study.

This research aims to develop a wireless BT strain sensor that uses RFID for wireless communication with BIM-based SHM system. The strain sensor can be custom designed to detect whether the pre-specified strain threshold level has been surpassed or not. It is hoped that this strain information can assist engineers to infer whether the safety of the structure (e.g., due to yielding or fracture) is at issue. The proposed breakage-triggered wireless strain sensor is low cost, low power and requires very little maintenance in use. By using the RFID technology, the damage status of key structural components such as structural fuse elements can be rapidly assessed simply

through scanning, which is highly desired for post-earthquake inspection. The salient features of this RFID-based passive wireless strain sensor are summarized as follows:

- No power requirement: By using RFID tags, no external power supply is needed to power the RFID tags. In this way, the cost at installation and maintenance would be much lower compared with other types of strain sensor. More importantly, power outage is very likely during or after natural disasters like earthquake when sensors requiring power supply to function would become dysfunctional and no data would be collected.
- On-demand strain data acquisition: Passive RFID tags do not emit any data signals unless the user scans the tag using an RFID reader. This feature is desirable for structural health monitoring to avoid radio frequency signal interference.
- Programmable sensor with key SHM information stored: RFID tags can be programmed in advance to store key SHM data such as sensor location/specification and structural member parameters. Passive RFID tags can have up to 1 kilobyte of non-volatile memory available for such data storage. The stored data is allowed to be altered later to include updated data.
- Do not require line-of-sight scanners for data reading from the RFID tags.

3.3. Basics of RFID antenna design

This section gives a brief discussion of fundamental RFID antenna parameters and the key characteristics of an antenna. This introductory description provides a necessary theoretical background on UHF (ultra high frequency) RFID antenna design.

3.3.1. Impedance match between RFID IC chip and antenna

Passive UHF RFID tag consists of an IC chip attached directly to an antenna. Proper impedance match between the antenna and the chip is crucial in RFID tag design. It directly influences RFID system performance characteristics such as the reading/writing range of a tag (Nikitin and Rao 2006). It is known that a RFID microchip is a nonlinear load whose complex impedance in each state varies with the frequency and the input power (Loo *et al*. 2008). The chip circuitry requires certain minimum voltage or power to function. The variation of the chip impedance with power and frequency can drastically affect the performance of the RFID tag. Usually, in order to maximize the tag range, the antenna impedance is matched to the chip impedance at the minimum power level required for the chip to work. The better the matching, the less power is reflected on the connection between IC bumps and antenna pads. This will result in a maximum power transfer to the IC.

The complex impedance of antenna and IC can be expresses as:

$$Z_a = R_a + jX_a, \qquad Z_c = R_c + jX_c \tag{3-1}$$

Where Z_a is the antenna impedance and Z_c is the IC impedance. The antenna impedance is the parameter describing the antenna input behavior as a circuit element. As usual in electronic circuit design, it is important to match this antenna impedance (Z_a) to a given source impedance, which is the IC chip impedance (Z_c) in the case of RFID applications (Balanis 2004).

The maximum power delivered from the source to the antenna is given if the antenna impedance is complex conjugate to the chip impedance (Dobkin 2008):

$$Z_a = \bar{Z}_c \tag{3-2}$$

By adding a circuit to the antenna to bypass the IC, the impedance of the antenna will be altered and the impedance matching between the antenna and IC chip is voided. Due to this impedance mismatching, the reading range of the RFID tag would be altered. Therefore, the change of antenna status can be used to signify the status of breakage-triggered strain sensor. The reading range of the modified RFID tag is normally made shorter because the antenna of RFID tag is designed to reach the maximum reading range at impedance matching.

3.3.2. RFID antenna tuning parameters

Considering the above described impedance matching and the impact of each part on the matching between antenna and IC chip, three parameters can be adjusted to tune the antenna parameters: Loop size (Area), Dipole length (L), Dipole distance (D), as illustrated in Figure 3-2. To adjust the impedance of the RFID tag antenna, some changes need to be made to the RFID tag antenna. Clearly, these two parameters, L and D, are not convenient to adjust and relate to the strain (deformation) sustained by the structure. However, the loop size could be adjusted by adding a by-pass over the two terminals of the RFID IC chip, as shown in Figure 3-3. When the by-pass is closed, the loop size is reduced to almost zero, which

deactivates the RFID tag. After the by-pass is broken, the impedance of the RFID tag is restored to its normal operating value.

To test the effect of by-pass on the RFID tag, wireless interrogation was conducted on the RFID tag. In this wireless interrogation test, the RFID reader swept through a pre-defined interrogation frequency range (902 to 927 MHz, which is allocated for RFID UHF bandwidth in North America) with a frequency interval of 1 MHz. At each interrogation frequency, the output power of RFID reader is increased at 0.1 dBm interval until the RFID tag is detected to identify the output power threshold, which is the minimum power level to activate the RFID tag. Through a USB 2.0 port, a computer interface is used to operate and retrieve measurement data from the RFID reader. The configuration of the RFID tag and by-passes are shown in Figure 3-4. The bypass was added to the antenna at difference distance respectively in order to form different loop area. It can be seen from the interrogation results that by adding the bypass, the responding power threshold of the RFID tags is increased to higher level, that is, without changing the reading distance and antenna orientation, higher power level is now required to communicate with the RFID tag after adding the bypass to the IC chip in the RFID tag. The closer the bypass to the chip, the higher power level is required for the RFID reader to talk to the tag. This feature can be utilized to identify the close or open status of the bypass which is part of the BT strain sensor proposed in this study. The results of the wireless interrogation test are shown in Figure 3-5. It's noted that the RFID reader's output power range is 10 to 27 dBm. If the responding power threshold is higher than the maximum power level

(i.e., 27 dBm), the RFID reader would not be able to detect the tag and the RFID tag is completely deactivated by the bypass.

The Skyetek M9 UHF RFID reader is a multi-protocol ETSI 302 208 compliant UHF (862 - 955 MHz) RFID reader platform that supports a wide variety of UHF RFID tags. It can read and write based on the EPC Class1 Gen1, ISO 18000-6B and ISO 18000-6C (EPC C1G2/Gen2) air interface and communications standards. The RF output power of the M9 is software-adjustable from 10 to 27 dBm (Skyetek 2012).

3.4. Breakage-triggered strain range sensor: device mechanics

3.4.1. Mechanics of BT strain sensor

The working principle of the BT strain sensor for detection of threshold strains is to connect a crack-sensitive brittle bar with an RFID tag which changes the impedance of the tag by short-circuiting the IC chip. Because of this impedance mismatch, the RFID tag is no longer able to communicate with the RFID reader at previously set output power level. When the pre-set strain threshold is surpassed in the brittle bar due to increasing deformation in the monitored structure, the bypass to the IC chip is broken and the normal communication between the RFID reader and tag attached to the brittle bar is restored. Therefore, the breakage of the brittle bar triggers the restored capability of RFID tag to communicate with RFID reader about the updated status of threshold strain being surpassed in the BT strain sensor.

The overall structure of the threshold strain detection system with BT strain sensors mounted on the monitored structure (e.g., an I-section beam) is shown in Figure 3-6. The C mark in Figure 3-6 indicates the proposed BT strain sensor which would break

and open the bypass once a pre-set strain is surpassed. It thus acts as a threshold strain sensor which uses RFID tag for wireless communication. Before the breakage of the BT strain sensor, the voltage or power on the IC chip would fall below its minimum threshold power level for the RFID reader to communicate with the RFID tag even if it's within its nominal reading range. If the structure member yields due to the extreme load and the strain at point C reaches the sensor's breakage threshold strain level, then the RFID circuit resumes to its normal state and the voltage between point A and B returns to be the normal level for the RFID tag to communicate with the RFID reader. The RFID reader can detect the tag and send the tag ID to the corresponding reader software. Also, by retrieving the other information from the RFID tag, it provides important information about the damage locations that need attention and repairs.

3.4.2. Brittle bar design

The following characteristics are desired for BT strain sensor design: 1) conductive trace is broken once the brittle bar is fractured. 2) low-cost strength material for the brittle bar; 3) ease of application. The most important requirement is the brittle bar breaks at the pre-set strain level. The crack propagation must be fast so that the conductive trace will break immediately after the breakage of the brittle bar.

Conductive paint is applied on the brittle bar to form a conductive trace which is connected to the RFID tag at Point A and A' in Figure 3-7. When the brittle component is fractured due to strain on the structural member, the RFID tag is made

active and its stored data can be interrogated by a RFID reader. The design for the brittle bar in the BT strain sensor is shown in Figure 3-7.

The gage length between the two end fixtures of the BT strain sensor, *Ls*, determines how large the monitored area would be. The BT strain sensor is attached to the structural element at these two end fixtures. Also the threshold strain can be adjusted by changing the value of *Ls*. The threshold strain is defined as the relative displacement between the two ends fixtures divided by the gage length *Ls* at the time point of breakage. The width and height of the brittle bar (typically with a rectangular cross-section shape) is denoted as *W* and *H* respectively. The values of these two parameters should be determined in such a way that the brittle bar fractures when the overall deformation over the sensor gage length surpasses a pre-determined threshold strain value. Additionally, other parts in the sensor should be made much stronger and stiffer so that the deformation in the brittle bar contributes almost exclusively to the strain sustained by the sensor.

Conductive paint is applied to cover the side area of the brittle bar and the two terminal pads (marked A and A' in Figure 3-7) of the conductive trace are connected to the RFID tag. Therefore, the conductive trace completes the bypass to the IC chip but would open the bypass immediately after crack is formed in the underlying brittle bar. This way, by checking the status of the corresponding RFID tag, the BT strain sensor should yield the information as to whether threshold strain levels have been surpassed in the monitored structure.

3.4.3. Numerical simulation based design validation

To obtain the deformation of the brittle bar right before it breaks, a finite element (FE) analysis was conducted to guide the design. A FE analysis software program – ANSYS v13 was used for this purpose in this study. Acrylic was selected as the brittle bar material used in this study. For acrylic sheet, the tensile strain at break is assumed to be 3%. In this study, threshold strain for the BT sensor is defined as sensor strain at the breakage point when the first principal strain in the brittle bar reaches 3%. The overall deformation of the sensor at breakage is called critical displacement.

The overall dimensions of the sensor are, Hs=37 and Ls=30 mm. The width and height of the brittle bar is varied to achieve different values of the ratio between its local principal strain and the sensor strain. For convenience in notation, each design is denoted as HxWy, where x is the height value of the brittle bar and y is the width value with a unit of mm. The left side of the sensor is fixed in both the vertical and horizontal degree-of-freedoms while the right side of the sensor is allowed to move in the horizontal direction. The sensor strain is calculated as the ratio of the horizontal displacement underwent by the right side of the sensor over a gage length of Ls equal to 30 mm. Figure 3-8 shows the meshing scheme for the H9W2 model in ANSYS. To achieve better accuracy, elements were refined at the brittle bar and surrounding areas.

According to the Maximum Normal Stress Theory (Rankine 1857), a brittle material will fail when the maximum principal stress exceeds some value, independent of

other stress components present. Therefore, the failure criteria for the brittle bar adopted in this study is that first principal strain reaches the fracture strain in a simple tension test. For example, the acrylic brittle bar will fail by fracturing whenever the maximum first principal strain around the corner surpasses 3%. For brittle material, the first principal strain is defined as the first principal stress divided by the modulus of elasticity (E) of the material, that is, $\varepsilon_1 = \sigma_1/E$.

Contour plots of the first principal strain for each of the three brittle bar designs from a linear elastic FE analysis are shown in Figures 3-9 to 3-11 respectively. The first principal strain for the three cases always occurs at the corners where cracks are observed to first appear. The strains in other parts of the brittle bar are found to be much smaller by several orders of magnitude. The FE simulation results suggest that for the proposed configuration of brittle bar, a significant amount of stress concentration is seen near the corner region which makes the failure mode (break point and deformation) predictable and repeatable for brittle materials. The critical displacements which correspond to the first principal strain of 3% in the brittle bar for each design are listed in Table 3-1. It is seen that the critical displacements at the breakage point are: 0.295 mm, 0.430 mm, and 0.600 mm for H6W4, H8W3 and H9W2 respectively. When connected with an RFID tag, BT strain sensor with these three designs can detect three different threshold strain levels so that the actual strain range in the structure can be estimated by scanning the BT strain sensors. To visualize the first principal strain distribution in different designs, a constant displacement of 0.3 mm (corresponding to 1% sensor strain with a gage length of 30 mm) is imposed to the right-hand side of the BT strain sensor. The contours of the

first principle strain in the corresponding brittle bar are shown in Figure 3-12. The first principal strain observed in the FE model of H9W2, H8W2, H6W4 are 1.5%, 2.15%, and 3% respectively.

3.4.4. Experimental characterization test

To experimentally characterize the BT strain sensor, a test setup shown in Figure 3-13 was used. The test setup includes a hand-driven precision slide to impose the displacement on the test specimen and attaching fixtures. The linear motion slide has an accuracy of 0.001 inches (0.0254 mm) in measuring linear excursion distance. The BT strain sensor was attached to the linear motion slide with four screws.

Test specimens are shown in Figure 3-13. In this study, two types of brittle materials were used for the brittle bar in the BT strain sensor: (i) The first material is acrylic sheet with a thickness of 2.54 mm (0.1 inches). The acrylic specimens were cut from a 6 x 12 inches acrylic sheet using a carbon dioxide laser cutter (CO2 cutter). (ii) The other material is an epoxy paint that was custom made by mixing epoxy with fine calcium carbonate powder. The calcium carbonate powder is added to the epoxy resin mixture to increase the brittleness of cured epoxy paint. One advantage of using epoxy paint is that its fracture strain can be adjusted by changing the mix ratio of carbon carbonate powder in the paint. To degas the epoxy paint, vacuum pump was used to suck air bubbles out of the fresh paint mixtures. The fresh epoxy paint mixture was cast in a pre-fabricated mold and it generally took 72 hours for the epoxy paint to cure. As shown in Figure 3-14, the test specimens made of epoxy paint were comprised of two parts: the brittle bar is made of epoxy paint and the rest part is made

from acrylic sheet. The two ends of the conductive trace were connected to the two terminals of the IC chip in the RFID tag. SPI flash-dry silver paint was used in this study to form the conductive trace. This silver paint is a highly concentrated suspension (43% silver solids by weight) of silver powders combined with an organic suspending and binder system.

Figures 3-15 shows the cracks in the acrylic test specimen along with superimposed vector plots of first principal stress in the brittle bar. The vector plots are based on a linear elastic FE analysis of the brittle bar at breakage point. Clearly, the first principal stress orientation at the corner of the brittle bar agrees well with the crack direction at the same location. Figures 3-16 shows the cracks in the epoxy paint test specimen.

The test results of the critical displacement corresponding to the first breakage of the brittle bar (thus the bypass to the IC chip is eliminated due to broken conductive trace) are list in Table 3-2. It is seen that for the acrylic material, the standard deviation of the test results on critical displacement are 8.15% and 7.27% for H9W2 and H8W3, while this becomes 10.95% for H6W4. This might be partly due to the variation in the pre-tension of the test specimen induced by unevenly tightening the screws in different tests. Cracks in the brittle bar seen using a digital microscope (65x magnification factor) are shown in Figure 3-15. The histogram of the test results for acrylic BT strain sensor is shown in Figure 3-17. The brittle bar was found to fracture quickly after the initiation of the crack at the corner. No slow fracture process was observed in all the tests conducted in this study. As the conductive trace was deposited over one side of the brittle band, the conductive trace broke immediately

after the crack was formed, which led to the disconnection between the bypass and the RFID tag and RFID tag is restored to normal working condition due to removal of the short-circuit. For each design, 15 tests were repeated to get statistics of the BT strain sensor performance. Even greater standard deviation values are observed in the epoxy paint specimens as listed in Table 3-2. This might be due to the random material defects in the epoxy paint material such as micron-size air voids trapped in the paint. The histogram of the test results for the epoxy paint based BT strain sensor is shown in Figure 3-18.

3.5. BT strain sensor design for detection of multiple threshold strains

The test results described in the preceding section validate the BT strain sensors for detecting single threshold strain level although different design can be used for different threshold strains. In this section, a BT strain sensor with multiple brittle bars on a single device is proposed to detect multiple threshold strain levels. One of the advantages of such BT strain sensor with multiple brittle bars is to occupy smaller space at installation location in the monitored structure. The configuration of a BT strain sensor with two brittle bars is shown in Figure 3-19. It's worth noting that due to the space limit and load capacity of the linear motion slide, only two threshold strains levels were considered in this device. The test results of the critical displacement of this sensor design are listed in Table 3-3. The histogram of the test results on the critical displacement of the BT strain sensor with two brittle bars is shown in Figure 3-20. It is seen that the mean value of critical displacements is 0.34 mm for H6W4 and 0.69 mm for H9W2 respectively. By assuming a gage length of 2

inches (50.8 mm), the two threshold strain levels of this BT strain sensor are 0.66% and 1.3%.

3.6. Pilot study of buckling detector for tube

The BT strain sensor with brittle bar design was validated in the above described laboratory tests. It has been demonstrated that it's capable of detecting pre-set threshold strain levels and this information can be acquired wirelessly with an RFID reader. The threshold strain recordings are repeatable with a small tolerable variance. However, one of the limitations of the BT strain sensor is its difficulty to detect the buckling or local buckling in structures members such as global buckling of tubular members. This is because the above presented brittle bar design is intended to work under longitudinal deformation of the sensor without out of plane bending. Out of plane bending will cause torsion in the brittle bar and thus complication in quantifying the threshold strain.

To overcome the difficulty associated with buckling detection, particularly on structures with curved surface such as tubular members, another design for buckling detection is proposed here using epoxy paint patch. In this pilot study, this epoxy paint patch based buckling sensor can only tell whether buckling occurs or not. Further research works need to be done to quantifying the strain sustained by the epoxy paint patch during the buckling process.

A schematic of the epoxy paint patches installed on a paint bucket are given in Figure 3-21. The epoxy paint patch is cut into proper size and is attached to the tubular specimen when it's still flexible before fully cured. The test specimen in this test is a

1-qt. paint bucket with lid (diameter = 4.35 inches, height = 5 inches). To detect the breakage of the epoxy paint patch due to buckling of the bucket, silver paint was deposited to form conductive traces on the surface of the paint patch, as shown in Figure 3-21. When the epoxy paint patch breaks, the conductive trace also breaks and thus the RFID tag connected to the conductive trace will be restored to normal operation condition.

Four equally-spaced epoxy paint patches were bonded to each bucket specimen at their upper and lower sides using M-bond from Vishay. The experiment setup is shown in Figure 3-22. The RFID reader is placed 34 inches (86.4 cm) away from the center of the bucket specimen during the test. The servo-controlled SATEC universal test machine was used to applied axial load to the bucket specimen. The epoxy paint patches in test #1 after breakage are shown in Figure 3-23. A total of five tests were conducted. The epoxy paint patches are numbered as X-Y, number X denotes test number (1 to 5) and number Y denotes the epoxy paint patch number on each bucket (1 to 4). The test results of these five tests are listed in Table 3-4. It can be seen that for a bucket with obvious bucking, it's likely that some epoxy paint patches on the bucket may not break. However, at least one epoxy paint patch was found to break in all tests.

3.7. Summary

From the results presented in this chapter, it is shown that by modifying the RFID antenna, its responding power to the RFID reader would change. This feature can be utilized to detect whether a threshold strain is surpassed in the monitored structure by

relating the strain to the change in the RFID antenna property. The two brittle materials used in this study each have their own advantages and limitations. For the acrylic sheet, its physical properties are more uniform compared with custom-formulated epoxy paint. This yields the test results that acrylic specimens have smaller variance. However, the drawback of acrylic sheet is that acrylic strain sensors are difficult to mount on curved structural surface. For epoxy paint, any arbitrary shape is possible to form and can be made to conform to curved surface. If air void in the paint can be completely removed by adopting a professional degassing process, its physical properties after full cure should be more uniform and repeatable. In this study, both materials have been demonstrated that they could break at a pre-determined threshold strain level and can be satisfactorily used for the BT strain sensor. In conjunction with the RFID technology, the BT strain sensor can fulfill the goal of rapidly scanning the strain condition at the monitoring location and wirelessly transfer the data to BIM database at request.

Table 3- 1. Critical displacements for each brittle bar design derived from linear FE analysis (gage length 30 mm)

Design	Critical displacement (unit: mm)	First principal strain in the model	Sensor strain	Force (N)
H9W2	0.60	3.00%	2.00%	10.1
H8W3	0.43	3.01%	1.40%	24.6
H6W4	0.30	3.01%	0.98%	39.8

Table 3- 2. Experimental characterization test results of the critical displacement of BT strain sensor for detection of single threshold strain level (unit: mm)

	Acrylic plate (thickness = 2.54 mm)			Epoxy paint (thickness = 2.03 mm)	
Test No.	H6W4	H8W3	H9W2	H8W3	H9W2
1	0.25	0.46	0.69	0.53	0.58
2	0.30	0.53	0.61	0.43	0.76
3	0.33	0.48	0.66	0.51	0.64
4	0.36	0.56	0.64	0.46	0.86
5	0.36	0.53	0.61	0.53	0.74
6	0.30	0.48	0.69	0.53	0.76
7	0.36	0.53	0.66	0.56	0.66
8	0.36	0.43	0.76	0.41	0.64
9	0.41	0.48	0.74	0.56	0.79
10	0.38	0.51	0.71	0.53	0.76
11	0.33	0.48	0.61	0.56	0.81
12	0.36	0.58	0.66	0.48	0.84
13	0.36	0.56	0.74	0.43	0.81
14	0.38	0.51	0.64	0.51	0.74
15	0.38	0.53	0.66	0.43	0.71
Max.	0.41	0.58	0.76	0.56	0.86
Min.	0.25	0.43	0.61	0.41	0.58
Mean	0.35	0.51	0.67	0.50	0.74
Std. Dev.	0.04	0.04	0.05	0.05	0.08

Table 3- 3. Experimental characterization test results of BT strain sensor capable of detecting two threshold strain levels (unit: mm)

	Acrylic plate (thickness = 2.54 mm)	
Test No.	H6W4	H9W2
1	0.33	0.66
2	0.43	0.71
3	0.33	0.69
4	0.25	0.71
5	0.38	0.66
6	0.33	0.71
7	0.30	0.74
8	0.30	0.61
9	0.30	0.69
10	0.28	0.66
11	0.36	0.69
12	0.41	0.69
13	0.28	0.71
14	0.36	0.64
15	0.38	0.74
Max.	0.43	0.74
Min.	0.25	0.61
Mean	0.34	0.69
Std. Dev.	0.05	0.04

Table 3- 4. Summary of the test results from epoxy paint patch tests

("X"- Epoxy paint patch broke, "-"- No breaking)

Test No.	1-1	1-2	1-3	1-4
Results	X	-	X	X
Test No.	2-1	2-2	2-3	2-4
Results	X	X	X	X
Test No.	3-1	3-2	3-3	3-4
Results	X	X	-	X
Test No.	4-1	4-2	4-3	4-4
Results	X	X	-	-
Test No.	5-1	5-2	5-3	5-4
Results	X	X	X	X

(a)

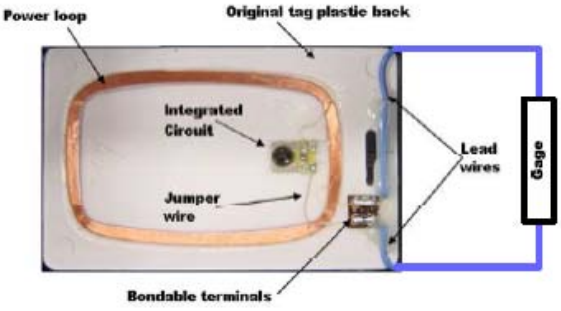

(b)

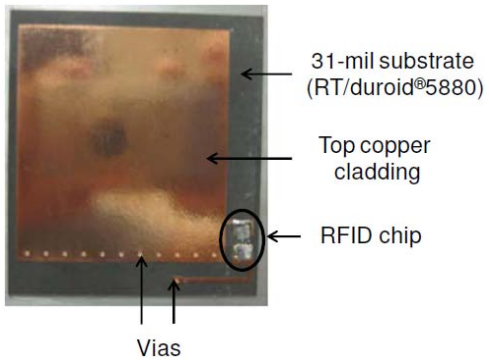

(c)

Figure 3- 1. RFID-based wireless strain or crack sensing devices developed by other researchers: (a) Morita and Noguchi (2008); (b) Chin *et al.* (2009); (c) Yi *et al.* (2011)

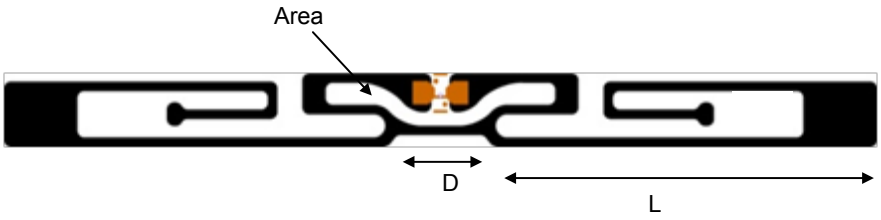

Figure 3- 2. Illustration of antenna tuning parameters

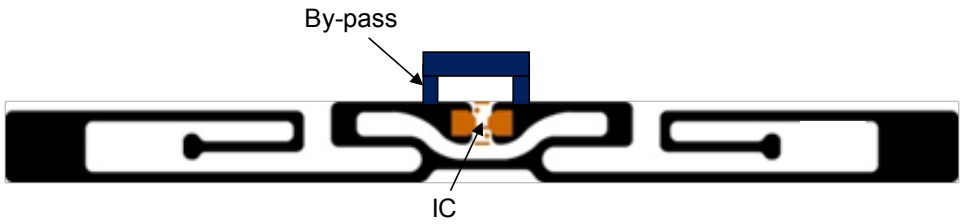

Figure 3- 3. Schematics of modifying RFID tag by adding by-pass to IC chip

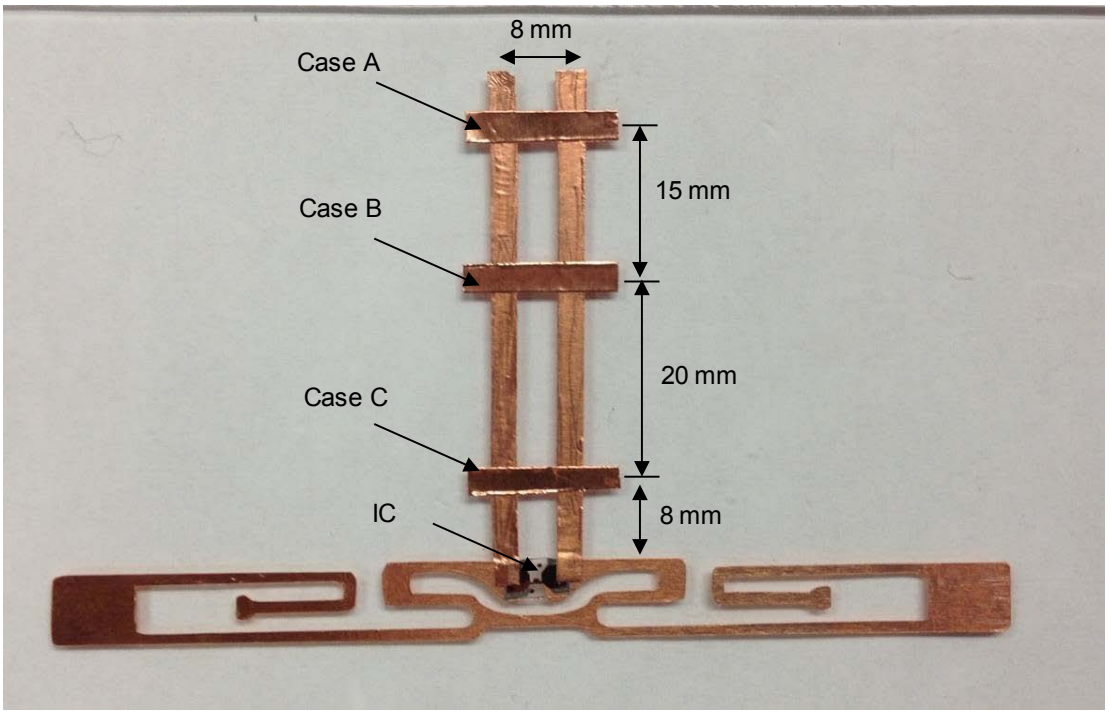

Figure 3- 4. Configuration of RFID tag with different bypass locations

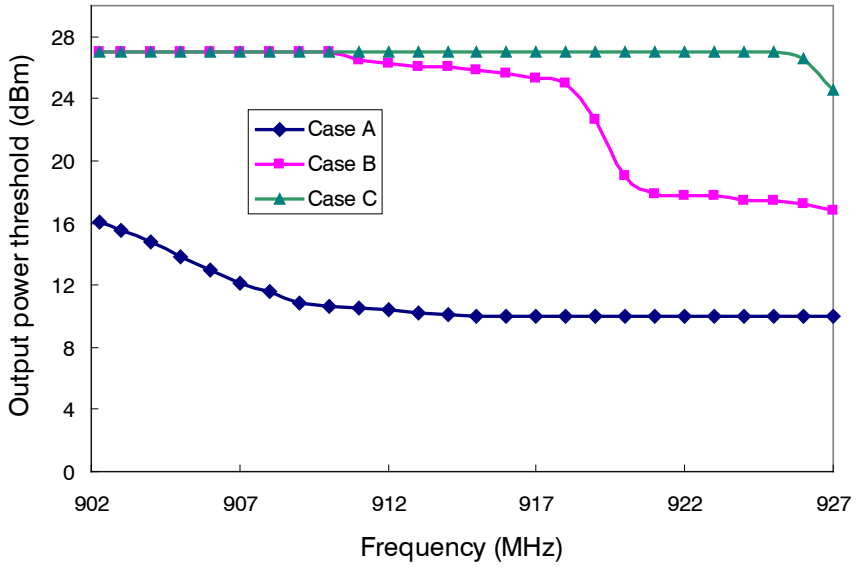

Figure 3- 5. Effect of adding bypass to IC chip on responding output power threshold level of RFID reader (see Figure 3-6 for explanation of different cases)

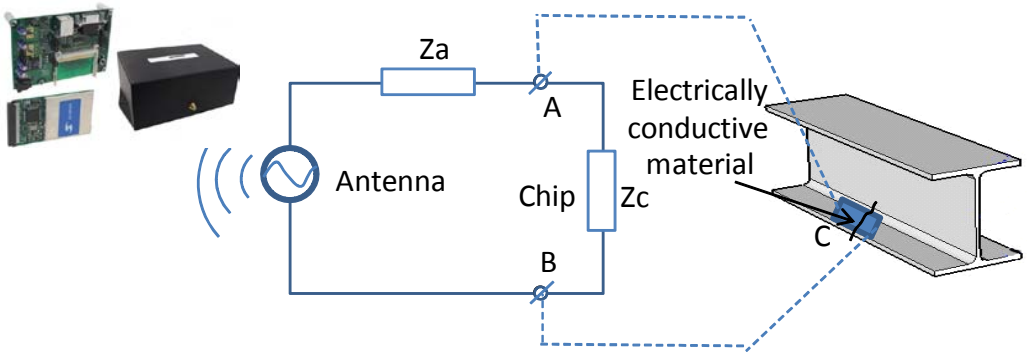

Figure 3- 6. Overall structure of the proposed threshold strain detection system with breakage-triggered (BT) strain sensors

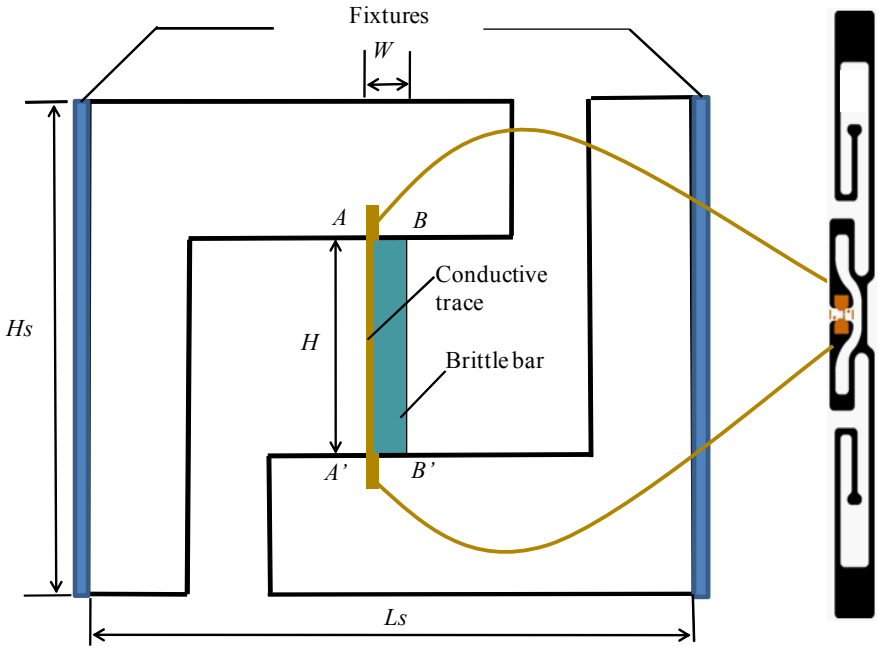

Figure 3- 7. Schematic of BT strain sensor design

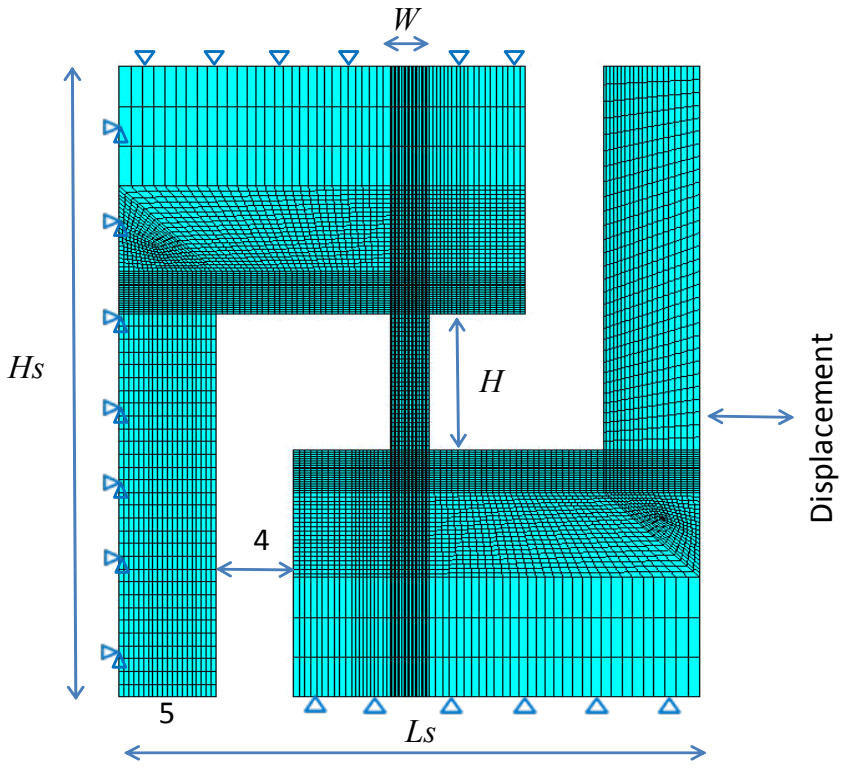

Figure 3- 8. FEM model of BT strain sensor (unit: mm)

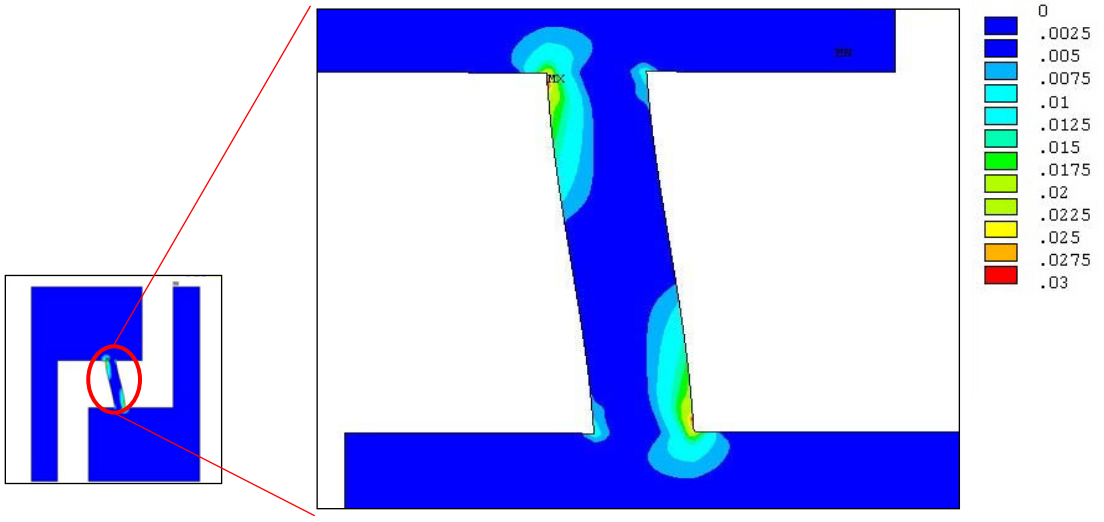

Figure 3- 9. Contour plot of first principal strain in the BT strain sensor (model H9W2, gage length = 30 mm) at breakage

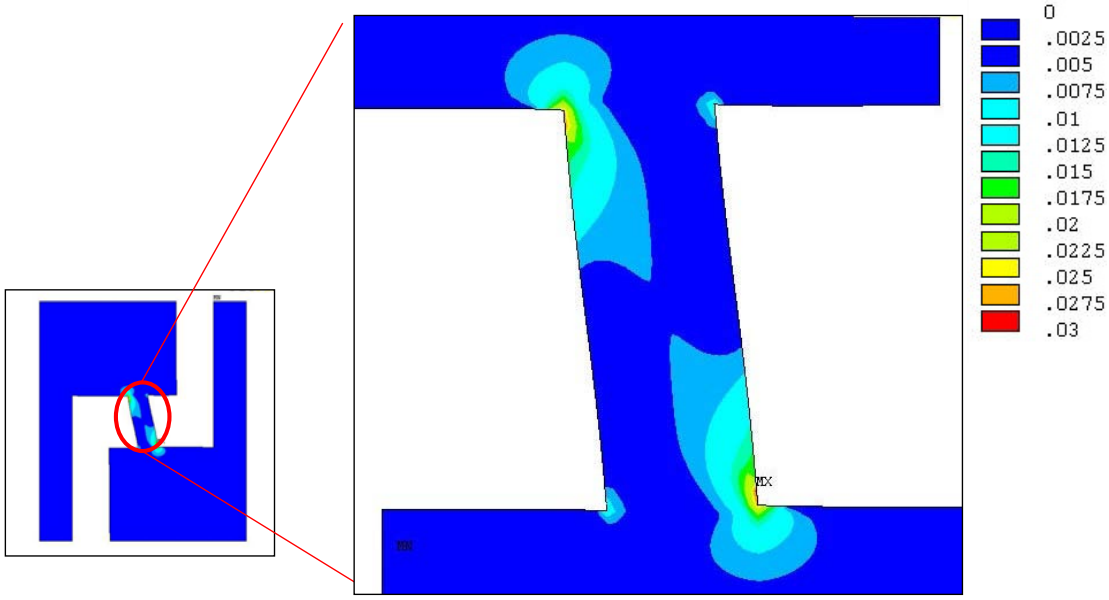

Figure 3- 10. Contour plot of first principal strain in the BT strain sensor (model H8W3, gage length = 30 mm) at breakage

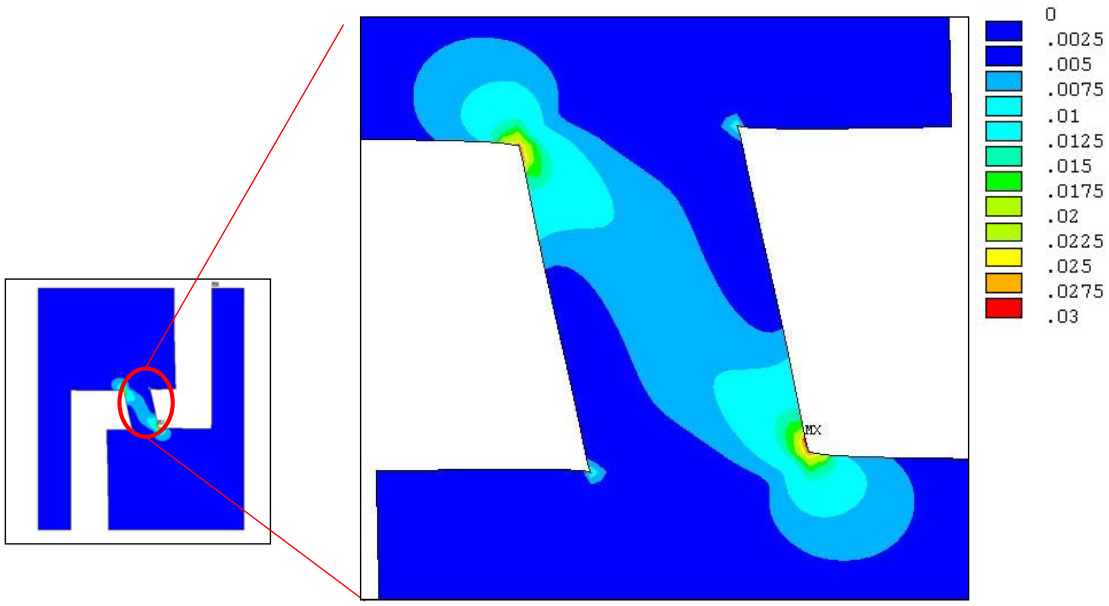

Figure 3- 11. Contour plot of first principal strain in the BT strain sensor (model H6W4, gage length = 30 mm) at breakage

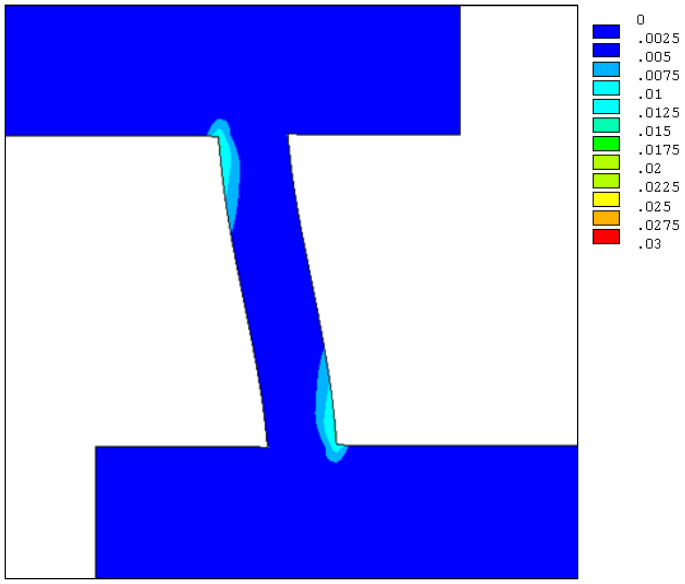

(a) H9W2

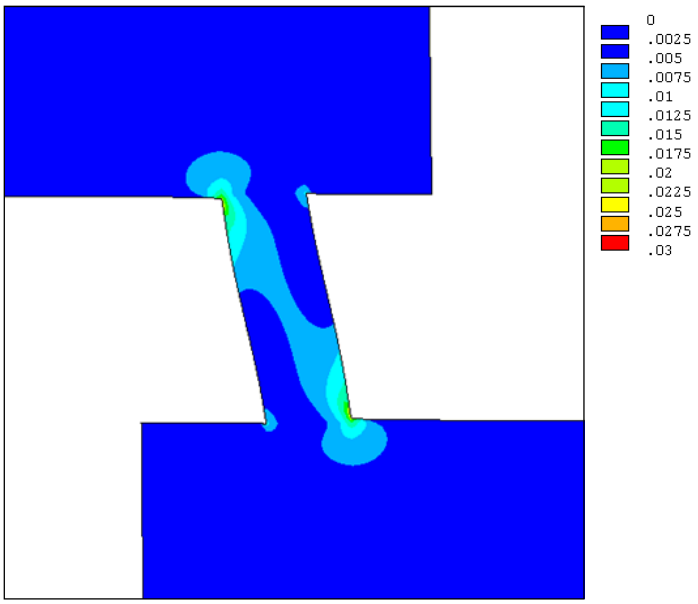

(b) H8W3

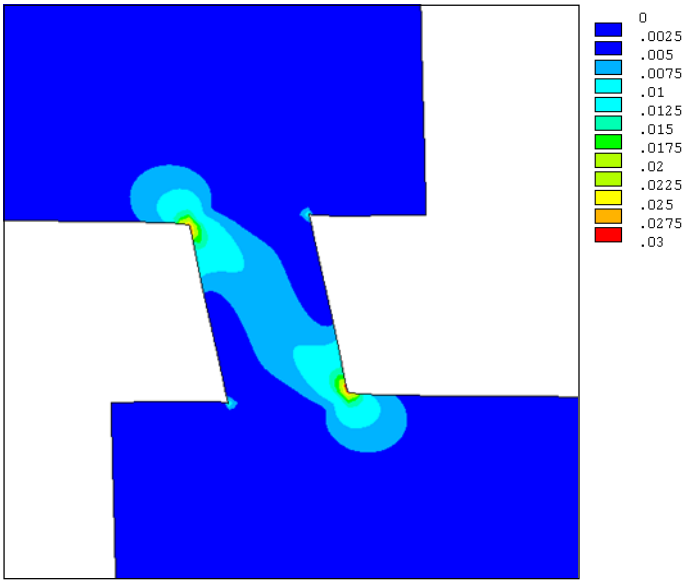

(c) H6W4

Figure 3- 12. Distribution of first principal strain in the model corresponding to 1% sensor strain in the BT strain sensor

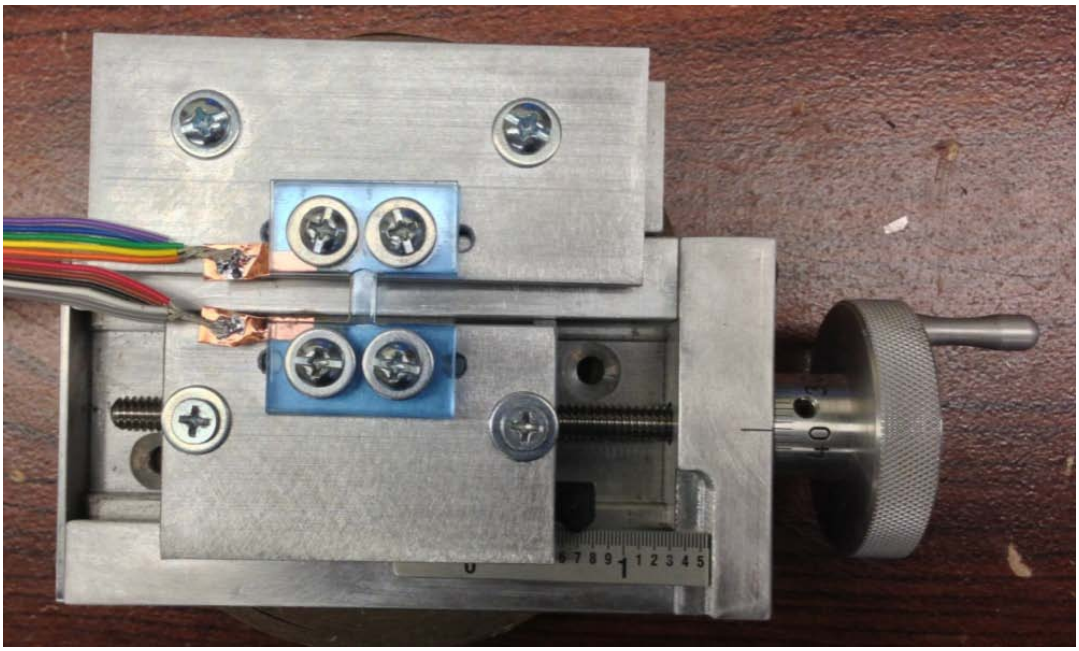

Figure 3- 13. Test setup used for experimental characterization of BT strain sensors using a hand-driven precision slide

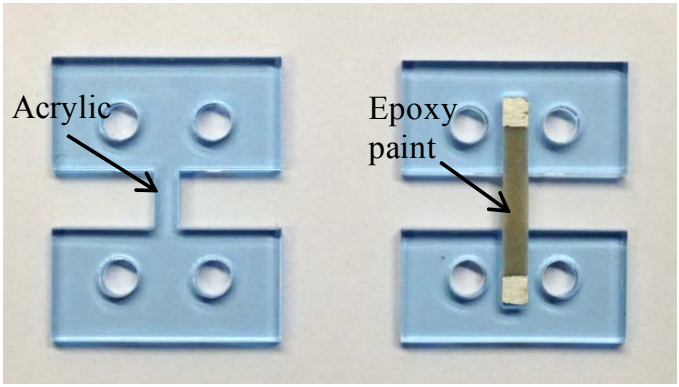

Figure 3- 14. Brittle bar specimens made of acrylic sheet and epoxy paint

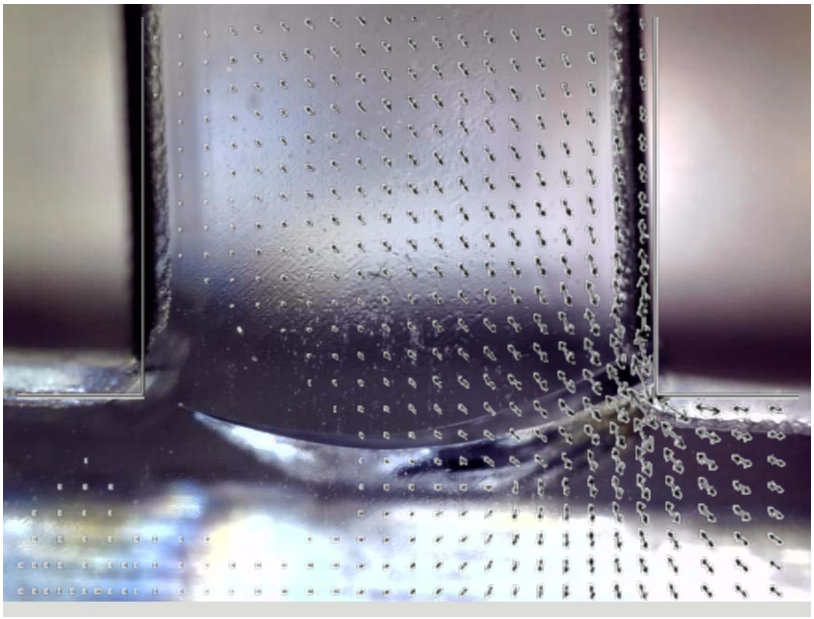

(a) H6W4

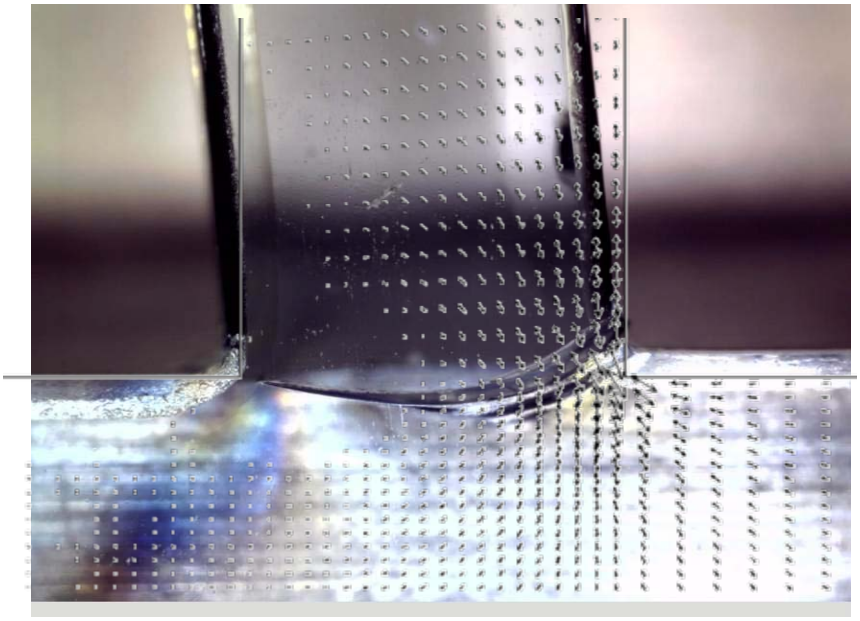

(b) H8W3

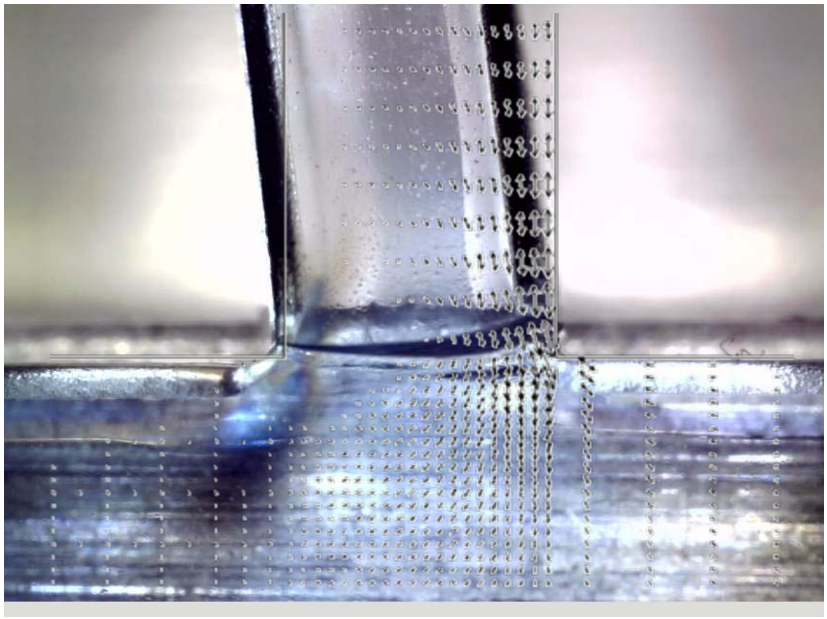

(c) H9W2

Figure 3- 15. Photos of cracked brittle bar (acrylic sheet) after test with vector plot of first principal stress superimposed

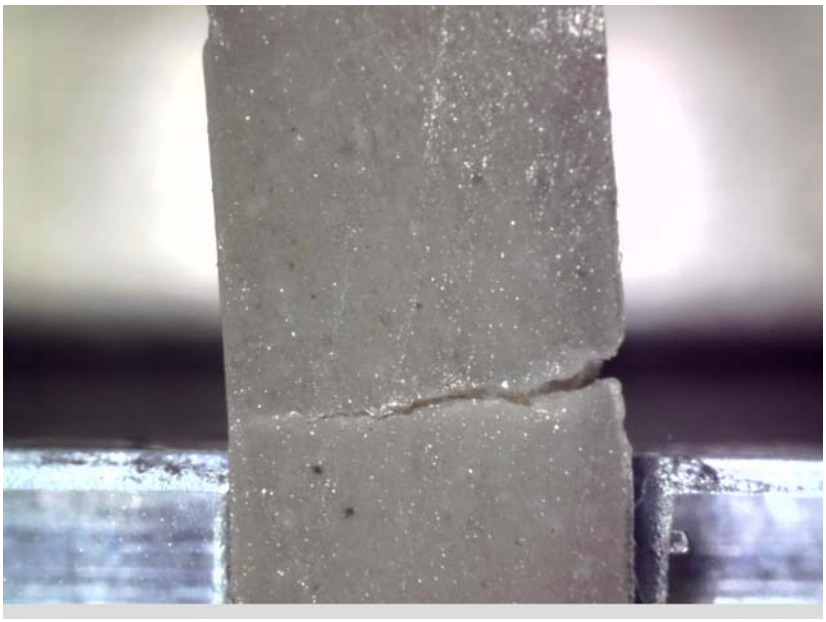

(a) H8W3

(b) H9W2

Figure 3- 16. Photos of cracked brittle bar (epoxy paint) after test

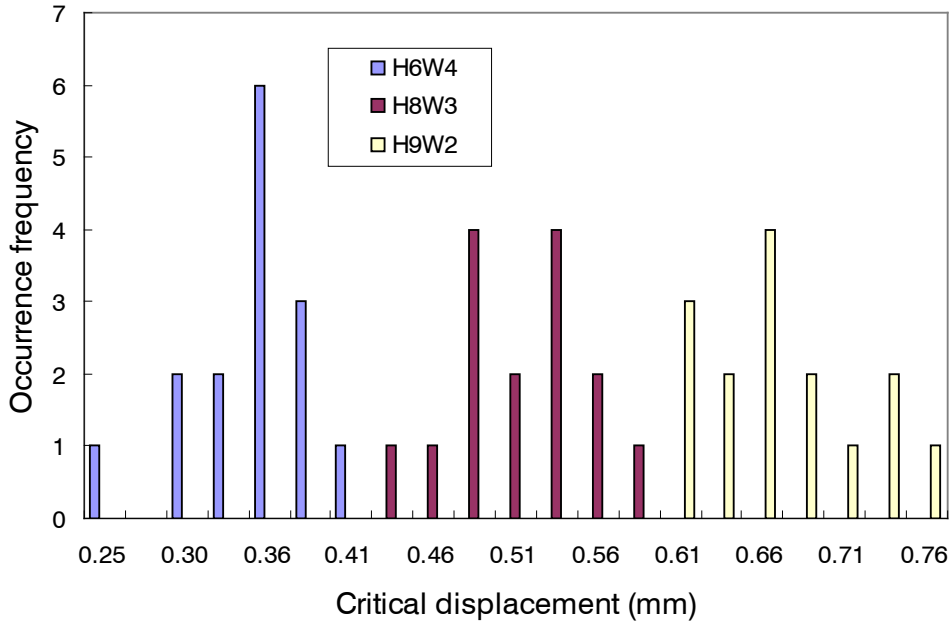

Figure 3- 17. Histogram of critical displacement test results of BT strain sensors (acrylic sheet) with single threshold strain level

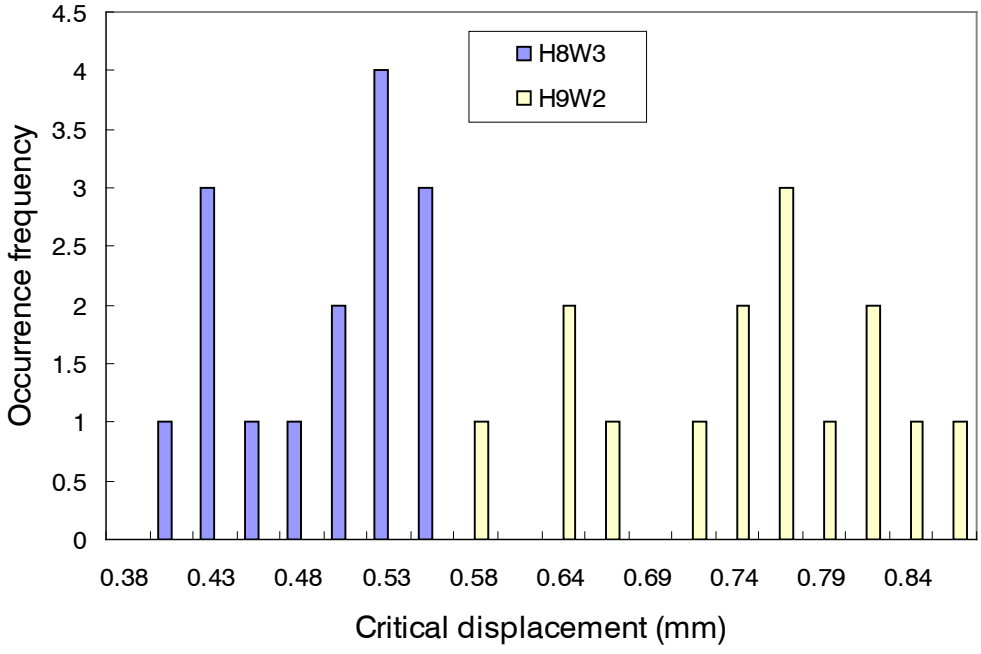

Figure 3- 18. Histogram of critical displacement test results of BT strain sensors (epoxy paint) with single threshold

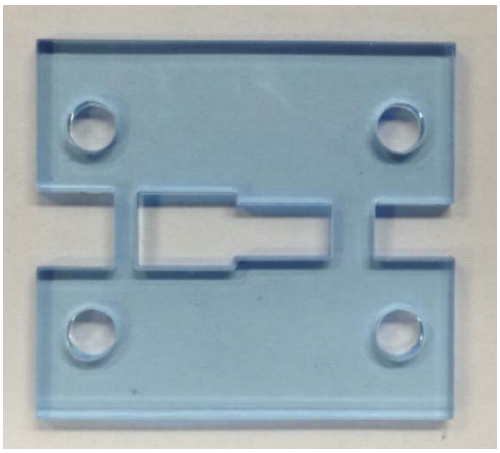

Figure 3- 19. Photo of BT strain sensors with two threshold strain levels (H9W2 and H6W4)

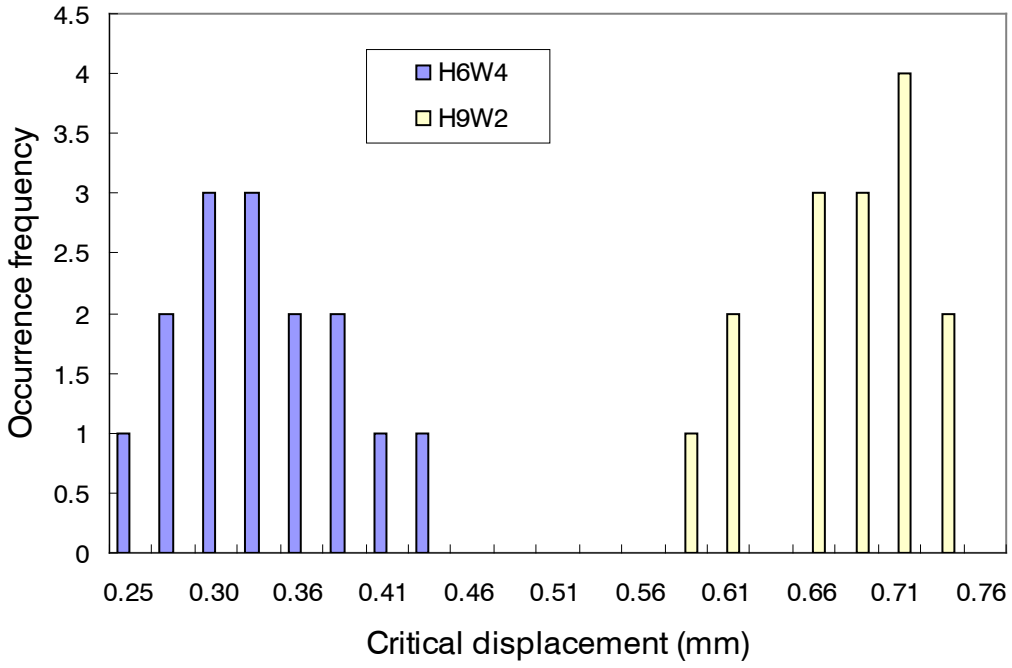

Figure 3- 20. Histogram of critical displacement test results of BT strain sensors (acrylic sheet) with two threshold strain levels

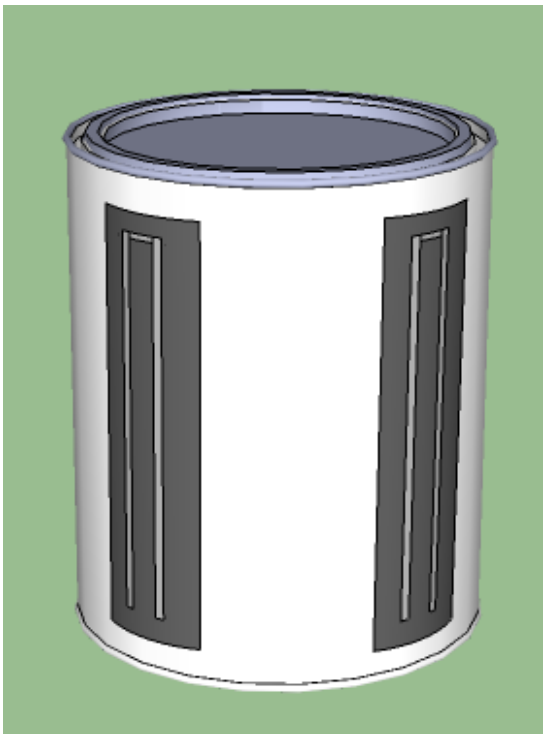

Figure 3- 21. Epoxy paint patch on paint bucket

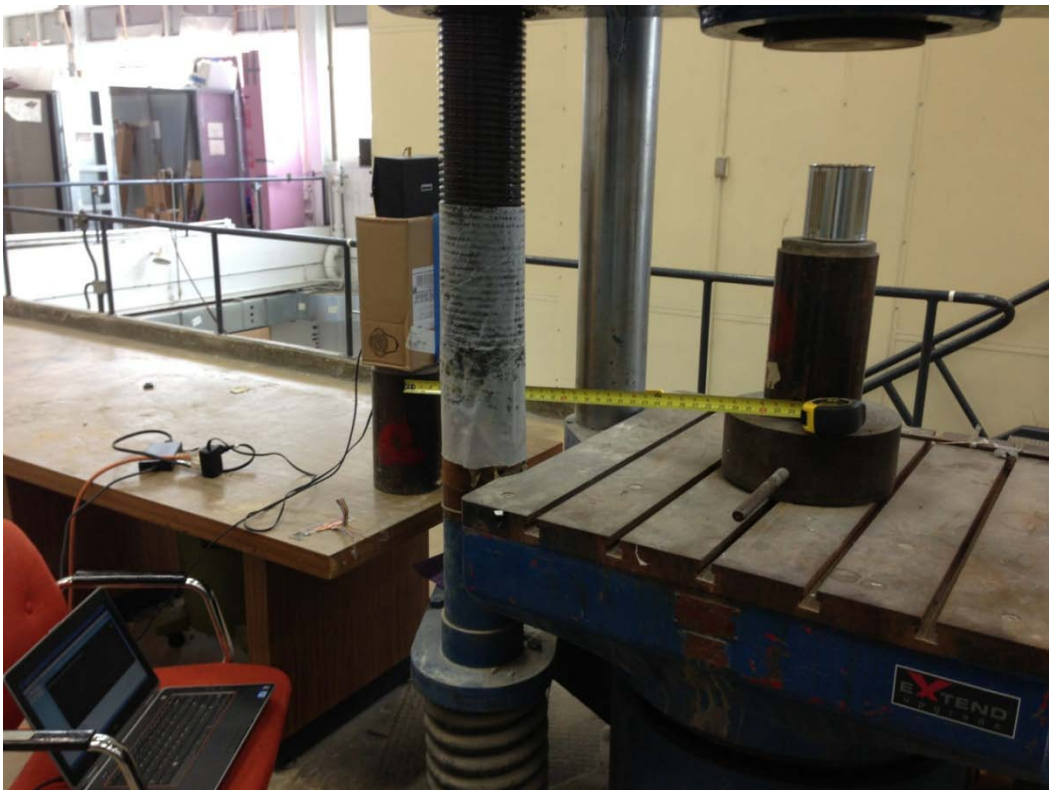

Figure 3- 22. Experiment setup for epoxy paint patch test

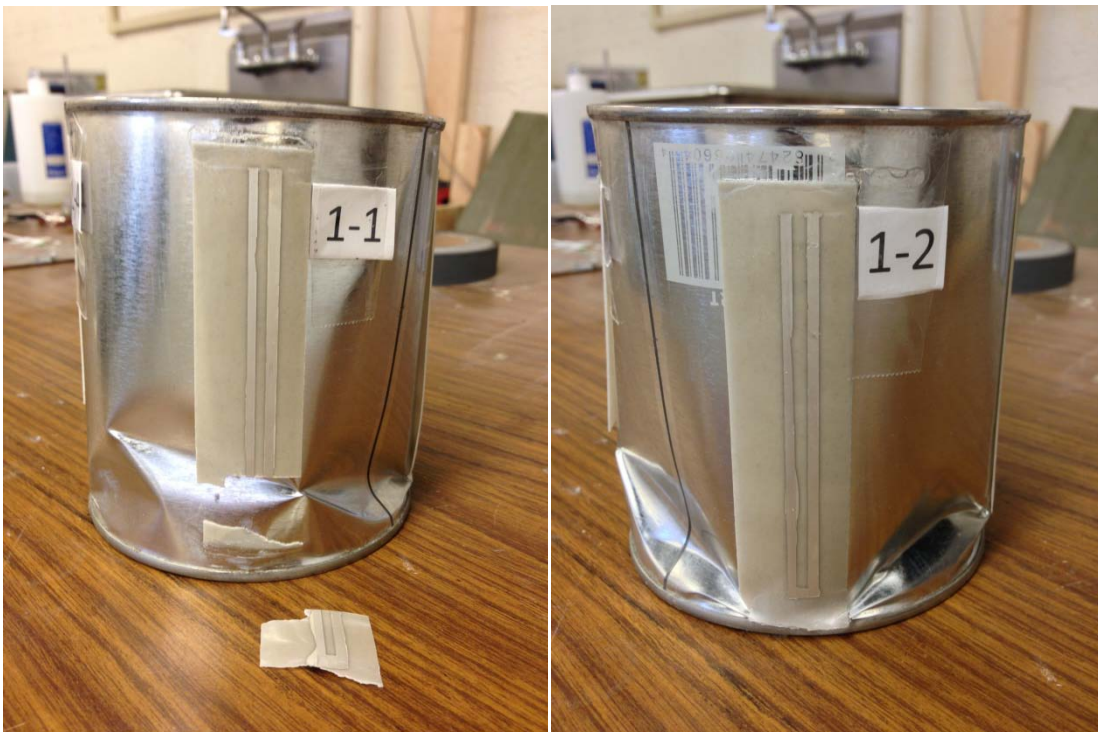

(a) (b)

(c) (d)

Figure 3- 23. Breakage of epoxy paint patch in test #1

Chapter 4: Sensor-Driven Structural Health Monitoring Integrated with Building Information Modeling

4.1. Introduction

Building information modeling (BIM) is a new technology which provides a platform for integrating data of different types and communication of information for asset management and preventive maintenance. BIM can also serve as an ideal 4-dimensional graphical computing environment for SHM and management practice which constantly involves considerable amounts of sensor data of different modalities. BIM software defines objects parametrically; that is, the objects are defined as parameters and relations to other objects, so that if a related object is amended, dependent ones will automatically also change (Eastman *et al*. 2011). Each model element can carry attributes for selecting and ordering them automatically, providing cost estimates and well as material tracking and ordering. BIM data can be stored as a digital file or in a database, and can be shared and exchanged between several applications (Isikdag *et al*. 2007).

A framework of SHM integrated with BIM was developed using Revit Structures software to illustrate sensor data storage and display, finite element (FE) simulation, and structural condition assessment integrated in a BIM-enabled 4D setting, as shown in Figure 4-1. The framework includes the following four major modules: BIM model and a database, BIM for SHM portal, sensor clusters with RFID tag that automates

the activation of the relevant area in the BIM model, and FE simulation software, which are briefly described below:

- The BIM for SHM portal module, which provides an interface and middleware to facilitate the access to other modules in the framework. This was developed using C# programming language. The C# main program provides the interfaces to these components and sends commands to them, such as start RFID reader and select and highlight elements. It also coordinates the work order of the components and acquires and sends necessary date between components. Details of this module will be given in the next section. This modular architecture is also designed to support future expansion and adoption of other SHM utilities.
- The BIM and database server module, which provides data access and storage in two software programs – a BIM software such as Revit and a database server such as SQL server. In this study, MS Access is used for illustration. The BIM model built using Revit is linked to a MS Access database which includes all the information of the elements in the BIM model. The two files (i.e. Revit model file .rvt and MS Access file .mdb) created by the two software applications can update each other when either one is modified.
- The sensor cluster module, which has a RFID tag for automated activation of the particular view area in the BIM model to display the sensor objects in the 3D BIM model. Monitoring data from sensor networks will be sent to database servers either on a pre-arranged scheme or on request.

- The FE simulation module, which consists of a set of basic functional units of a finite element structural analysis program. A FE analysis software program –OpenSees (Mckenna 1997) is used in this study. Other commercial general-purpose FE simulation software applications such as ANSYS, SAP2000 can be used for this purpose equally well as long as an adapter software application is available.

There are several major software developers such as Revit, Tekla, Bentley and ArchiCAD that supply products with functionality in the BIM world (Eastman *et al*. 2011). In this study, Revit - Autodesk's main platform for BIM is selected. Revit has very similar functionality to the other major BIM software. Revit was designed from the ground up as a BIM platform to specifically address problem areas of the architecture, engineering, and construction (AEC) industry. It is a complete discipline specific building design and documentation system supporting all phases of design and construction documentation. Revit structure 2012 was used as BIM software to develop the BIM model. Revit Structure is a technological platform that currently supports architectural, structural, and mechanical disciplines. It allows the user to design with both parametric 3D modeling and 2D drafting elements. Building Information Modeling is a Computer Aided Design (CAD) program that employs intelligent 3D objects to represent real physical building components such as walls and doors. Revit uses .RVT files for storing BIM models. Typically, a building is made using 3D objects to create walls, floors, roofs, structure, windows, doors and other objects as needed. These parametric objects — 3D building objects (such as windows or doors) or 2D drafting objects (such as surface patterns) — are called

"families" and are saved in .RFA files, and imported into the RVT database as needed.

The SHM framework integrated with BIM can significantly reduce the amount of time that would be spent performing searching, accessing and validating the information. As the structure's complexity increases, the BIM model becomes very large and identification and selection of the appropriate SHM locations for relevant sensor data viewing and information processing/display becomes very time-consuming if this is done in a manner of manual operation. This drawback undermines the advantage of BIM technology.

In recent years, Radio frequency identification (RFID) has been given lots of attentions for its fast development in many fields such as asset management, access control, transportation and logistics. RFID uses radio frequency electromagnetic fields to transfer data from a tag attached to an object, for the purposes of automatic identification and tracking. Commonly adopted frequency bands for RFID communication are 120-150 kHz (LF), 13.56 MHz (HF), 902-928 MHz (UHF), and 2.4 GHz (UHF). Passive RFID tags require no battery and are powered by the electromagnetic fields used to read them. The tag contains electronically stored information which can be read from up to several meters away. Also, each RFID tag was assigned a global unique ID, this make it ideal for identification application.

The major advantages of using RFID are that the tag does not need to be within line of sight of the reader and may be embedded in the tracked object, tags can be read through many non-metallic materials, and many tags can be identified at the same

time, each tag can contain more data inside and the radio signal transferring distance is longer. These key features enable the RFID system to fast access the BIM and automatically identify and select appropriate structural elements being monitored in BIM. The data stored on the tags could be read, updated and changed by RFID readers. In the SHM application in question, it is desirable that the RFID tag could be read from far distance. Hence, the system can detect the structure component even if the component is hidden or not visible.

This chapter describes the initial efforts in developing a BIM for SHM portal targeted for urban infrastructure monitoring and management applications. A custom developed middleware enables automated sensor data entry into BIM environment to avoid possible human related errors. A prototype bridge model was developed using Revit Structures software to illustrate sensor data storage and display, FE analysis, photorealistic visualization, dynamic simulation, and structural condition assessment integrated in 3D visual setting.

4.2. BIM for SHM portal

A 3D BIM model for the monitored structure provides a visual clue about the location and condition of the key monitoring area and associated sensor clusters. This facilitates the visualization of the processed SHM information and its variation with time. In this way, a 4D model that integrates a 3D drawing with time is made available and allows the consideration of maintenance actions for deteriorating structural components through their life cycle. Changes that occur in the structural condition and SHM system over time can be highlighted in such a 4D BIM model.

Furthermore, structural safety can be quantified in terms of structural reliability, taking into account the uncertainty involved. It is worth noting that structural safety is also time variant. This is because the loading condition and the properties of a structure may change over time. For example, many developed countries are currently experiencing a problem of aging and deteriorated bridge networks (Pablo 2009). Considering the fact that the ultimate goal of SHM is to evaluate the structural safety of the monitored structure, a 4D BIM model with time varying structural condition and system reliability information is very appealing for SHM applications.

As shown in Figure 4-2, the main computer program developed in the C# environment – the BIM for SHM portal, serves as the coordinator and interfaces with other components in the BIM based SHM system. The BIM for SHM portal coordinates the workflow in the system, such as activating the RFID reader and selecting the desired elements for condition assessment. Then it searches the BIM database for the "RFID Tag" of each element. If a match is found, the proper BIM elements would be highlighted in a user-defined color. In this study, the BIM for SHM portal, was developed using the Revit API and RFID reader API and programmed with Visual C# language. These APIs (Application Program Interfaces) are usually Dynamic-link library (DLLs) that allow the user access and control particular applications' work environments. The Revit .NET API allows users to program with any .NET compliant language including Visual Basic.NET, C#, and C++/CLI. The user can use the Revit Platform API to gain access to model's graphical and parameter data to perform tasks. The Skyetek API is built in C++

language, which allows user to manage basic and advanced RFID tag and reader manipulation tasks.

To be able to fast locate and highlight the area of interest corresponding to the selected sensor cluster in the BIM model, a shared parameter “RFID Tag” is added to the elements. Each BIM element is assigned an ID that uniquely identifies itself. This ID is not the RFID tag number; rather, this is the ID number assigned to each BIM element by Revit. A user can create custom parameters for any element or component category in the BIM software. In Revit, this is realized by creating a “Shared Parameter”, which will be assigned to a specific structural member and are also available to be shared with other members in the family. They offer the power to add custom data or information that is not predefined in the family file or project template. For example, “RFID Tag” and “Damage Flag” are two shared parameters which are custom defined here for SHM application and can be assigned to any structure element. It should be noted that in Revit only “Shared Parameters” can be shared by different projects and families and exported to external database in the ODBC (Open Database Connectivity) format. In Revit, export/import in ODBC format can be made compatible with a variety of database software such as SQL and Microsoft Access. This study uses Microsoft Access as the ODBC database and Figure 4-3 shows an ODBC database sheet created in BIM and tested in Microsoft Access for its compatibility.

Additionally, an Autodesk Revit Add-in program has been developed to display the sensor data such as time series in the BIM environment. Visualization and imaging of SHM results are very helpful in communicating with practitioners and engineers. 3D

models and data display enhance the vividness, clarity, pinpointing, and thereby improve the users' ability to visualize information and increase the users' effectiveness in communicating with others. The visualization capacity is especially appealing to SHM applications because this can expose users to view a space and its health condition that is not easily accessible in a real world environment. For example, it could be used by inspection engineers to walk through a bridge structure that otherwise has to be accessed through snooper truck and often requires road traffic control and even road closing.

4.3. Case study

This section reports a demonstration project which showcases the functionality of the BIM based SHM system for infrastructure monitoring. A prototype system including the Revit Structures, a FE analysis software, sensors and custom-developed middleware code (i.e. BIM for SHM portal), are presented in a case study involving a multiple steel I-girders bridge in Maryland. The bridge is a single-span structure of a span length of 140 ft (42.67 m), as shown in Figure 4-4. The bridge was built in 1980's and fatigue cracks were identified in some of the diaphragm connection welds. Types of sensors used in the field test include piezoelectric film AE sensors, wireless accelerometers, laser distance sensors and strain transducers.

Users can directly use the Revit GUI interface to create the structure model by adding architectural elements, structural elements, and other elements such as sensors or other SHM components. The BIM model of the steel bridge built in Revit is shown in Figure 4-5.

Modeling for expediency alone may not work if a BIM for SHM model is desired. For example, consider the modeling of the steel I-girder of the bridge in BIM. Although it may be tempting to model the I-girder monolithically, the monolithic I-girder will need to be remodeled and segregated to match the FE analysis and hot spot areas required by the SHM application.

Revit DB Link is an add-in program provided by Autodesk that allows user to maintain a relationship between a Revit project and a Microsoft Access, Microsoft Excel, or ODBC database. A user can use Autodesk Revit DB Link to export Revit project data to the database, make changes to the data, and import it back into the project. The database displays Revit project information in a table view that can be edited before import. By using Revit DB link, BIM database was developed in MS Access 2007 format. The BIM database includes database tables for each element types and instances.

The workflow of the BIM based SHM system is shown in Figure 4-2. Eight Revit add-ins have been developed in the Microsoft C# environment. They can be called by clicking the pull-down menu shown in Figure 4-5. Prior to staring the main BIM for SHM portal program, certain parameters are allowed to be edited in the two files - *parameter.txt* and *RFID parameter.txt*. These files allow user to set the path for BIM database and parameters for Skyetek reader. Once these two parameter files are set up, the system is ready to start the main BIM for SHM portal program. The Skyetek RFID reader will be called and starts to scan tags sequentially. During each updating cycle, the Skyetek RFID reader will perform scanning every once in a while at a pre-defined interval, and record the IDs of all the RFID tags within its reading range. The

BIM for SHM portal program compares the current tag ID pool with the one in previous cycle. If any change is found, the BIM for SHM portal program would send a request to the Revit to update its database and highlight the corresponding elements. By performing this check before sending out the request command, the program can avoid sending unnecessary update command to the Revit, and thus save the computing time. In the meanwhile, all the tag IDs would be saved to *RFIDList.txt*, which is located in the same directory. It can be used for verification purpose or other post-processing. If the loop time and interval for each scanning are set to small numbers, each scanning action would take less time at the price of increased likelihood for induced inaccuracy.

The BIM based SHM system is highly automated to minimize human intervention. However, if for some reason manual update is necessary, the Revit GUI also allows the user to run RevitAccessDB process directly. If the user wants to highlight certain elements whose tag IDs are known, he can type in the tag IDs in the file *RFIDList.txt*, and then check the RevitAccessDB GUI button. The damage flags can also be reset by clicking the ResetDamageFlag GUI button. In this example, sensor data from accelerometer has been stored at a pre-specified location on the user's computer. The user can display the acceleration data for the selected element using Revit GUI. Fourier transform was conducted on the sensor data. The sensor data and its frequency spectrum are visualized in the model, as shown in Figure 4-6.

This BIM for SHM portal also facilitates the communication between the BIM model and FE analysis program. The FE model is a 140-ft (42.67 m) long simple beam built in the Opensees navigator (Mazzoni *et al*. 2009). Moving truck load was applied to

the beam. The linear weight per foot length of the beam (including the bridge deck weight) is 487.1 lbf per foot (7.12 kN/m). The moment inertial I is 87,032 in^4 (0.036 m^4) and the cross-sectional area A is 113.75 in^2 (6.45 cm^2). To run the FE analysis, simply check the "RunOpenseesTCL" box in the Revit GUI drop-down menu, as shown in Figure 4-7. After the FE analysis is done, all the results files would have been saved to a pre-determined location. In the subsequent post-processing add-ins such as visualization the data, the program would search the numbers that match the ID of the selected elements in the BIM model, and then plot the desired response data such as internal forces. For illustration purpose, the bending moment of the highlighted beam location is plotted in Figure 4-8.

As mentioned above, if one and only one element is selected, the plot window will show as Figure 4-8 after checking the "PlotBeamMemberMoment" box. Within this window, the time series curve can be zoomed-in or out. Similarly, other response data such as middle span displacement of the bridge under specified loading or from monitoring can be visualized as well, which is shown in Figure 4-9.

A modal analysis was also conducted in the FEM model through the Revit GUI, as shown in Figure 4-10. It's seen that the fundamental frequency of the prototype bridge is 2.9 Hz (natural period displaced in the figure as 0.311 seconds). From the field test data using wireless accelerometers attached to the flange of the bridge girder, the measured fundamental frequency of the bridge is 3.2 Hz, which is close to the FEM result considering the simplicity of the FE model used in this study.

As mentioned earlier, since the ultimate goal of SHM is to evaluate the structural safety of the monitored structure, a 4D BIM model with time varying structural condition and system reliability information is highly desired for decision making in the SHM applications. A time-dependent reliability analysis requires the knowledge of deterioration models which predict the future structural condition and form the basis for life-cycle monitoring and maintenance planning. However, the reliability analysis is only as good as the models which support it. The models must be updated over time to revise the optimum maintenance strategy based on how a structure actually behaves (Estes and Frangopol 2003). Sensor data from the SHM system installed on the monitored structure has been shown to be very useful for updating the deterioration models for future condition forecasting (Catbas *et al*. 2008; Li *et al*. 2011).

Condition rating data based on periodic inspection of bridges components provides an overall characterization of the general condition of a bridge that has been routinely used by inspection engineers. According to the National Bridge Inspection Standards (NBIS), condition ratings are one-digit numbers that characterize the general condition of the entire component being rated. For example, the condition of different parts of a bridge may be rated on a scale of 0 to 9 (with 9 being "excellent" and zero being "failed"). Condition ratings assigned to elements of a component must be combined to establish the overall component condition rating. Unlike the condition-rating inspection approach, the element-level inspection approach is quantity-based and allows the bridge owner to track deterioration of each bridge element over time (AASHTO 2011). This is advantageous, in that, by better understanding the rate of

deterioration, the bridge owner can thus make more intelligent and cost-effective decisions related to preserving their bridge assets. Element-level inspection thus provides the means to help make better performance-based decisions for bridge management and many states in the US are beginning the process of collecting element level data (Rehm 2013).

To accommodate the need for element-level condition data entry and display, the bridge structure can be divided into small, user-defined elements. The condition data for each element is recorded and stored in a database, which could be displayed in the BIM environment at user's request for selected element as shown in Figure 4-11. To illustrate the concept, condition rating along with a Markovian-based modeling approach for estimating the deterioration of condition states of structural elements is adopted in this study. Markovian-based model is one of the most popular methods for bridge deterioration modeling and have been used by major Bridge Management System software including PONTIS. A Markov chain is a stochastic process in which the probability distribution in the next time point depends only on the current state (Cesare *et al*. 1992). The probability transition matrix key to the Markovian-based bridge deterioration model can be derived from the overall condition rating of bridges in a network (e.g., the National Bridge Inventory in the US). The Markovian transition matrix reflects the typical deterioration rates of the bridges in the dataset. Once updated with monitoring data, they can be used to forecast the future condition states of the monitored structural components. To implement this in the BIM environment, "Element CS" add-in has been added to the Revit GUI and by clicking this button from drop-down menu, the selected element's condition as well as an

action button for forecasting the future condition state with the Markovian-based modeling approach is seen in Figure 4-11. With this visual display of the structural condition at element level, the bridge owner can make more intelligent and cost-effective decisions related to preserving their bridge assets with timely maintenance actions.

4.4. Summary

This chapter presents a sensor-driven structural health monitoring (SHM) system that integrates building information modeling (BIM), sensors, FE analysis, and database technology. BIM can serve as an ideal 4-dimensional graphical computing environment for SHM and management practice which constantly involves considerable amounts of sensor data of different modalities. The ability to visualize the inspection and monitoring work done in the life cycle of a structure provides engineers and decision makers with a photorealistic view of the SHM process, simplifying their understanding of current condition of structural elements, structural reliability, maintenance work to schedule, response of structures under natural hazardous events such as earthquakes. In many instances, this improved understanding can facilitate the decision-making process often required when resources are scarce. To accommodate the need for element-level condition state data entry and display, the structure can be divided into small, user-defined elements. The condition data for each element is recorded and stored in a database, which could be displayed in the BIM environment at user's request for selected element.

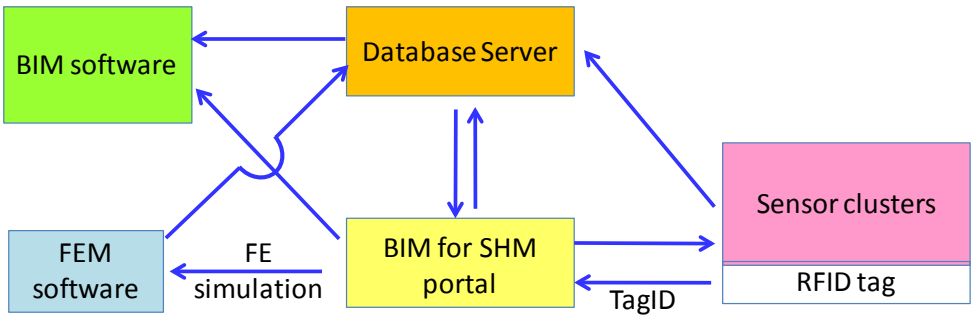

Figure 4- 1. Schematic of SHM framework integrated to BIM

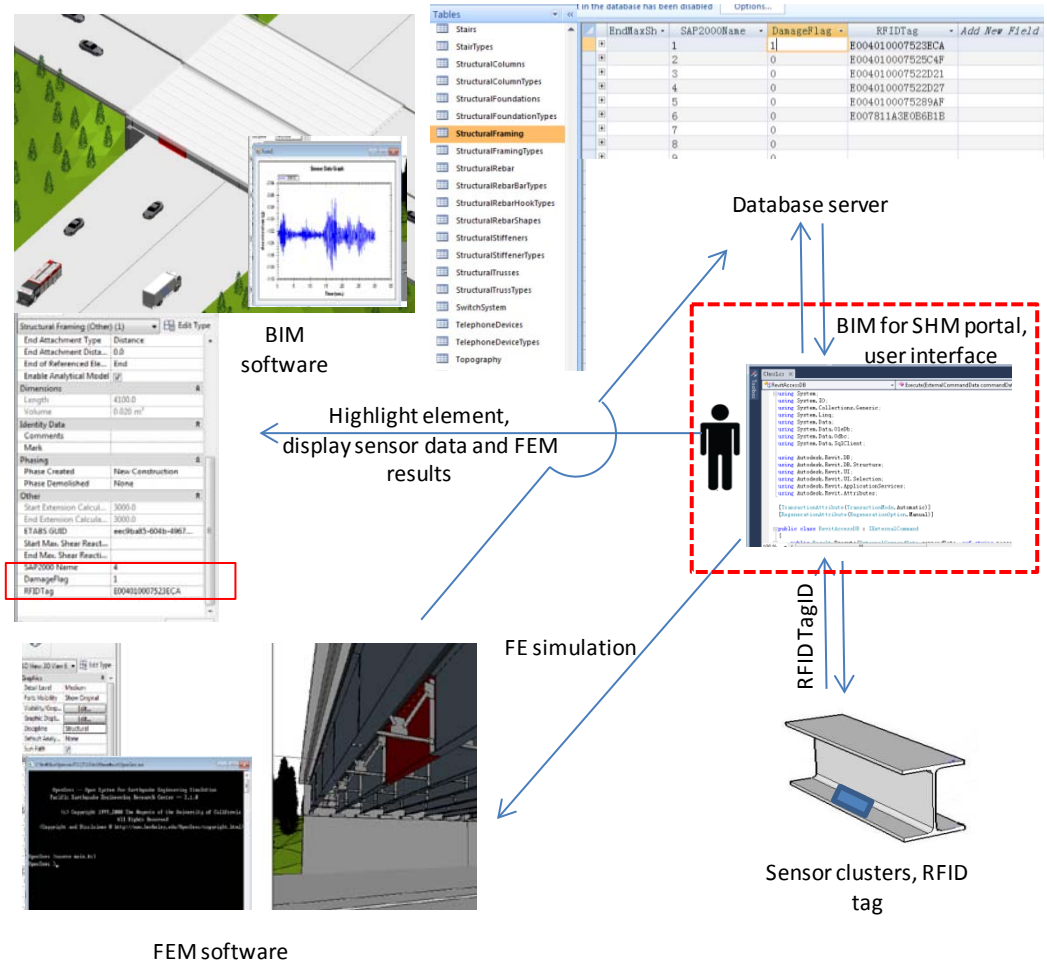

Figure 4- 2. Schematics of the workflow in the BIM based SHM system

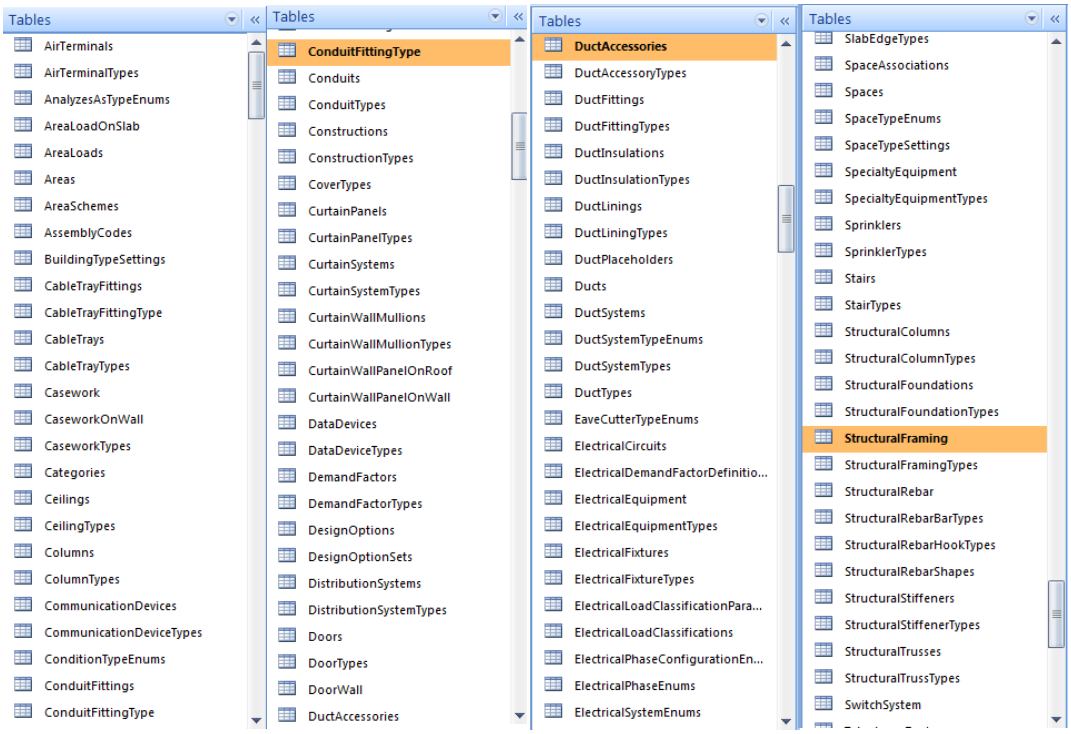

Figure 4- 3. BIM database tables in MS Access

Figure 4- 4. Pictures of the prototype steel highway bridge in case study

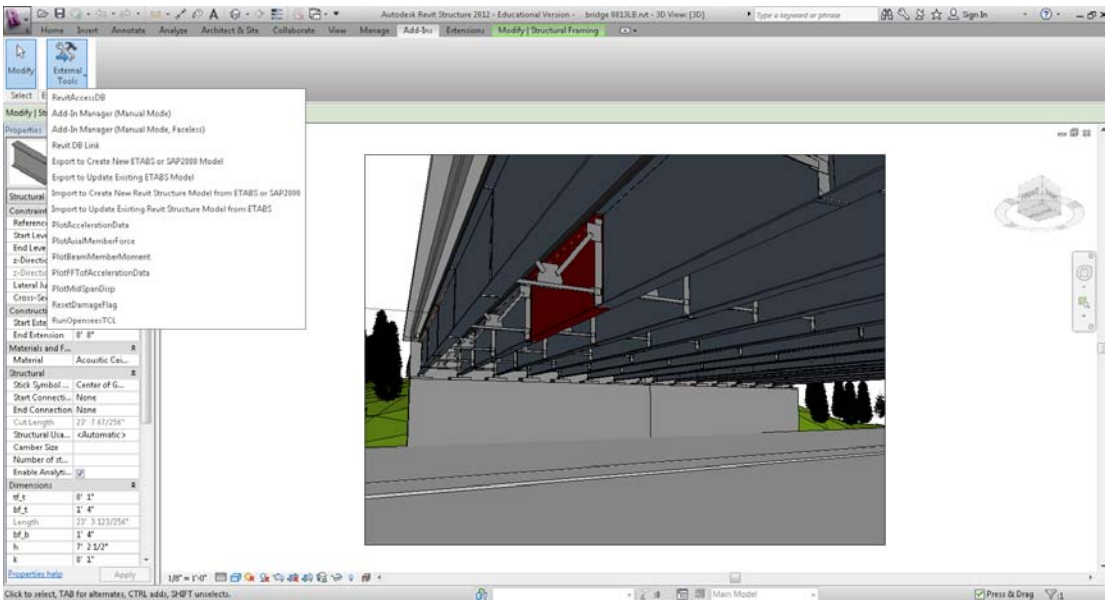

Figure 4- 5. BIM model of the prototype steel highway bridge

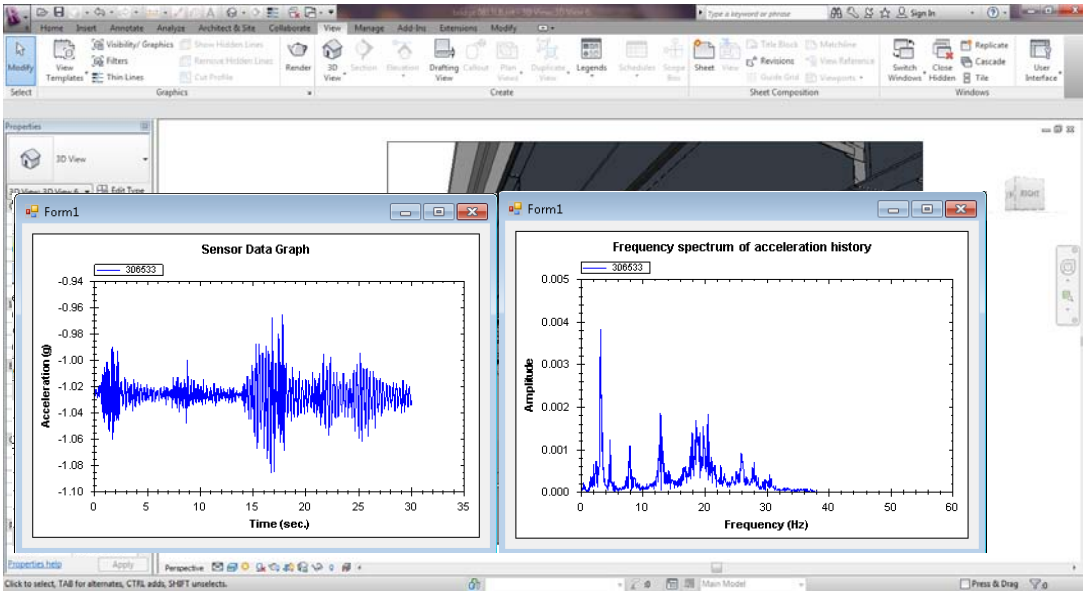

Figure 4- 6. Time history and frequency spectrum of sensor data displayed in BIM environment

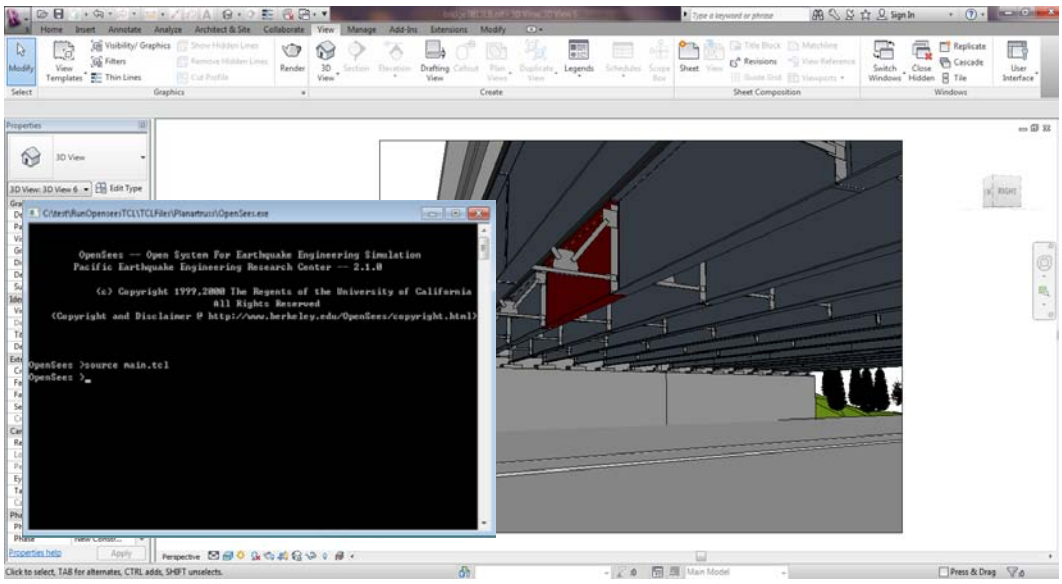

Figure 4- 7. "Run Opensees" add-in for FE analysis called in BIM environment

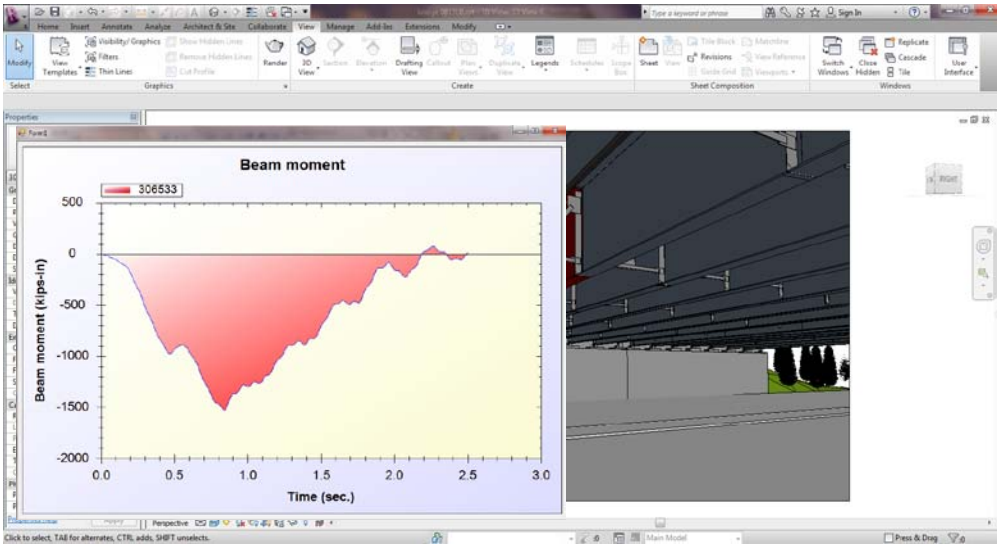

Figure 4- 8. "PlotBeamMemberMoment" add-in called in BIM environment

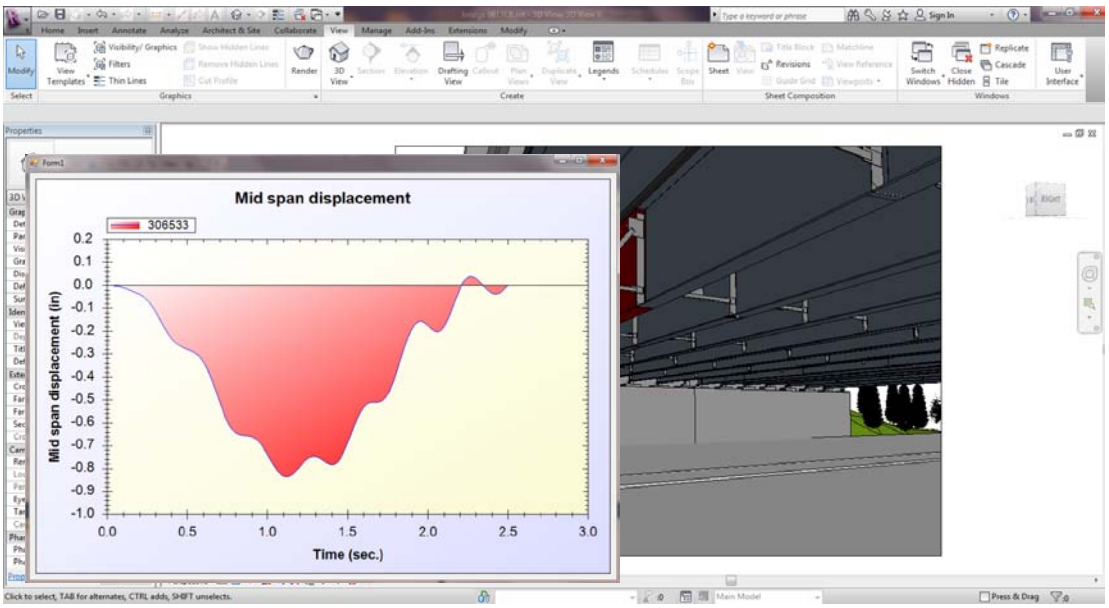

Figure 4- 9. “PlotMidSpanDisp” add-in called in BIM environment

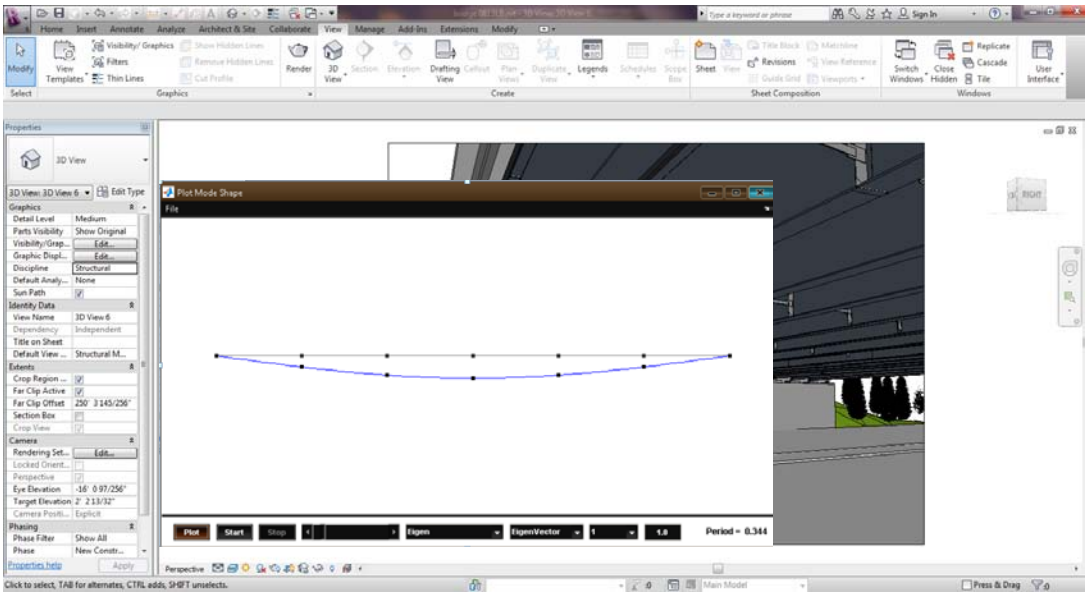

Figure 4- 10. Modal analysis results from FE analysis program displayed in BIM environment

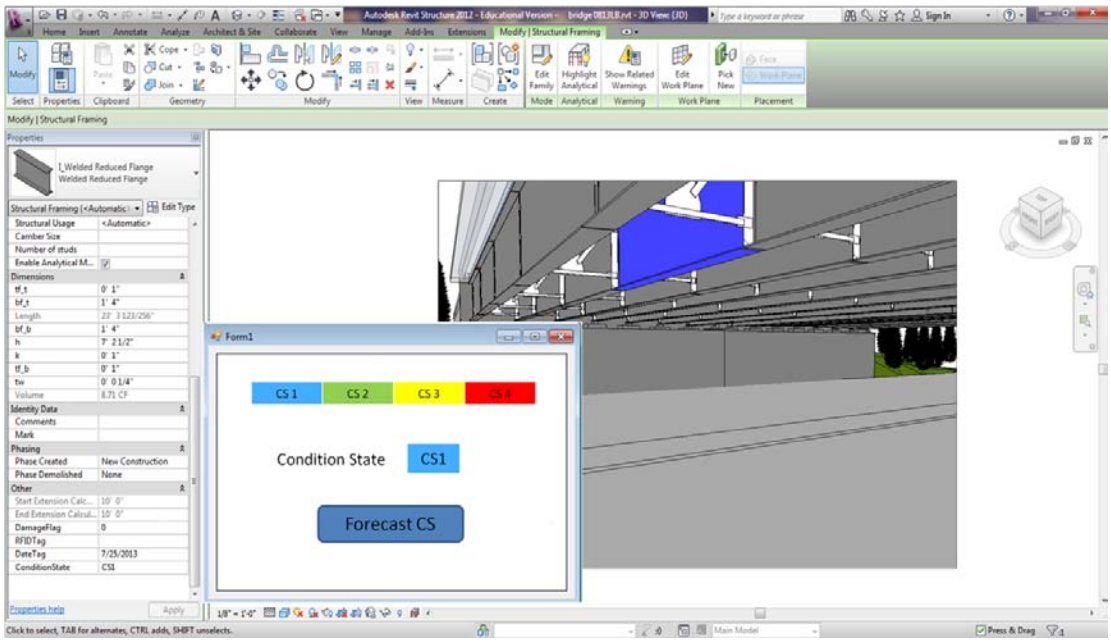

Figure 4- 11. Element-level condition state displayed for selected element in BIM environment

Chapter 5: Resilient Structure Design with Fuse Members

5.1. Introduction

5.1.1. Background of steel structural framing

Steel structural framing has been used for large span industrial buildings and facilities for public gathering. In the emergency of a strong earthquake, public spaces covered by large span arch structures, such as public halls or school gymnasiums, are expected to be converted to refuges for shelter provision for which a higher level of seismic performance (e.g., immediate occupancy) is preferred under strong earthquake events. However, under extreme earthquake, either part of the roof enclosure or the entire roof structure can be damaged. Collapse of roof could cause severe economic loss and poses safety risk to building residents. Furthermore, with recent emergence of building integrated renewable energy production system such as solar panels integrated with building facades and roofs, damage inflicted on the solar panels by excessively large deflection or collapse of roof would cause economic loss and power disruption to building residents.

The collapse of a steel roof frame structure can be initiated by the buckling of a few members, as a result of load redistribution causing a subsequent progressive overstress condition in other members and thus its load carrying capacity is usually limited by the failure of first member or set of members to fail.

5.1.2. Concept of force limiting device (FLD)

In an attempt to alter the brittle collapse behavior of steel roof frame structures under extreme earthquake loading, force limiting devices (FLD) can be used for robustness enhancement. These devices are fitted to critical compression members, and designed to provide a purely plasto-elastic behavior with a long plateau of member ductility (e.g., as exhibited in buckling-restrained braces). Since collapse is initiated by only a few critical members, the use of force limiting devices can be limited to a small selection of the most critical compressive chord or web diagonal members. The feasibility of using force limiting devices for controlling the behavior of space truss was validated in a research conducted by El-Sheikh (1999). The principle behind using these devices is to introduce artificial ductility in truss compression members, which would otherwise possess brittle post-buckling characteristics involving a loss of both stability and strength upon buckling.

Also, to minimize the residual deformation of the roof structure associated with conventional FLD exhibiting bilinear hysteresis, self-centering (SC) members similar to the one developed by Zhu and Zhang (2008) provides a promising FLD alternative for use in steel roof frame structures.

Large residual deformation associated with conventional ductile structural design can often make the structure appear unsafe to occupants, impair its ability to resist subsequent aftershock earthquakes and significantly increase the cost of post-earthquake retrofit (Ruiz-Garcia and Miranda 2006a, 2006b). Residual structural deformation thus starts to be recognized as a complementary parameter in the

evaluation of structural (and non-structural) damage in performance based earthquake engineering (Pampanin *et al*. 2003; Christopoulos and Pampanin 2004). Recognizing the importance of controlling the residual deformation, self-centering seismic resisting system has recently been attracting considerable attention from the community (e.g., Kurama *et al*. 1999; Ricles *et al*. 2001; Christopoulos *et al*. 2002; Mahin *et al*. 2006). Such self-centering system is characterized by a flag-shaped hysteresis loop with certain energy dissipation capability and small or zero residual structural deformation after strong earthquakes.

Special metals like shape memory alloys (SMAs) also exhibit a flag-shaped stress-strain curve (Casciati and Faravelli 2004; Desroches and Smith 2004; Song *et al*. 2006). Due to its unique energy dissipation behavior and high fatigue life, SMA has been studied for use as a self-centering damping device in seismic resistant structures (Dolce *et al*. 2000; Zhu and Zhang 2008; Miller *et al*. 2011). Dolce *et al*. (2000) tested Nitinol-based devices with full re-centering and good energy dissipation capabilities. Zhu and Zhang (2008) studied a special type of bracing member termed self-centering friction damping brace (SFDB) which exhibits a flag-shaped hysteresis loop and has a potential to be used for force limiting devices with self-centering behavior. In the SFDB, the self-centering ability is realized using super elastic SMA wires while its enhanced energy dissipation capacity is achieved through friction. Miller *et al*. (2011) studied the seismic behavior and performance of self-centering buckling restrained braces (SC-BRBs). A SC-BRB specimen consisting of a typical BRB component, which provides energy dissipation, and pre-tensioned superelastic NiTi shape memory alloy (SMA) rods, which provide self-centering, was

experimentally tested and its self-centering hysteresis is verified.

Self-centering fuse members can be used for ductility enhancement and residual deformation reduction. These self-centering members would be fitted to strategically selected locations to create a self-centering hinge zone, and designed to provide a flag-shaped hysteretic behavior. To concentrate the deformation in such a self-centering hinge zone, the use of self-centering fuse members can be limited to a small selection of only a few critical members through properly weakening.

5.1.3. Concept of concentrated damage zones

A structural weakening concept was employed in this study to improve the structural behaviour under dynamic loading. This concept is similar to selective weakening retrofit in earthquake engineering (Reinhorn *et al*. 2005).

For a different application on seismic response mitigation, Reinhorn *et al*. (2005) and Viti *et al*. (2006) introduced the concept of weakening structures (e.g. reducing strength) to reduce simultaneously total accelerations and inter-story drifts. The main features of this procedure were to reduce maximum acceleration and associated forces in buildings subjected to seismic excitation by reducing their strength (weakening).This concept was employed in this study to improve the structural behaviour. Note that the yield force of FLD was designed to be equal to the buckling force (i.e., critical load) of a member with imperfection.

The purpose of member weakening in the roof framing is to make the selected weakened member as a fuse element where favorable ductile damage of the overall

structure is concentrated. This concentrated structural weakening strategy could also bring other benefits such as ease in damage inspection and rapid structural repair with member replacement post extreme events. Strengthening critical members only would not improve the structure collapse behavior because doing so will increase the forces on their neighboring members and cause them buckle instead. To strength all structural members is clearly not economical.

Typically, a compromise has to be struck between the improvement to structural behavior associated with these devices and the cost addition caused by their use. Therefore, the use of FLDs is limited to a small selection of the most critical compression chord members in this study. This includes a strategy for selectively replacing key compressive members in steel roof structures with FLDs to prevent collapse or at least alter the collapse sequence to a favorable collapse mechanism. Simple linear finite element analysis of the original steel roof frame structure without FLDs was conducted to determine the internal forces in all members. The locations of the FLDs are chosen based on the axial force from this analysis. Several other plausible pressure distribution cases and found these selected places are also fine in order to improve the structural collapse resistance behavior compared with the original frame without FLDs. FLDs work as fuse members, where the deformation of the structure would concentrate; and because its strength is weakened compared to regular member, FLD would first be activated under many load cases.

5.2. Analysis procedure for dynamic collapse simulation

To accurately simulate the dynamic collapse of steel roof framing structures subjected

to combined gravity and earthquake load, non-linear time history analysis was performed in this study. The finite element model, that considers dynamic member buckling, yielding of tension members, and geometric nonlinearity due to large deflection of the roof structures undergoing collapse, is established using the OpenSees simulation platform (McKenna and Fenves 2005).

A progressive collapse refers to a structural failure that is initiated by localized structural damage and subsequently develops, as a chain reaction, into a failure involving a major portion of the structural system (Ellingwood and Dusenberry 2005). Several mechanisms might contribute or lead to the progressive collapse of steel roof frame structures including: buckling of compression member, yielding of a tension member, facture of a tension member or connector, and nodal instability. The collapse of a steel frame structure can be initiated by the buckling of a few members (Blanford 1997), and its load carrying capacity is usually limited by the failure of first member or set of members to fail.

In this study, a 2-dimensional force-based element with corotational formulation and fiber discretization of the cross section was adopted for the simulation of buckling, post buckling, and hysteretic responses of members in steel roof frames. In this force-based corotational element, both material and geometric nonlinearities are considered.

The formulation of force-based elements is based on interpolation functions for the internal force variation (Spacone *et al*. 1996). Neuenhofer and Filippou (1998) formulated a force-based element for geometric nonlinear analysis of plane frame structures, with linear constitutive relationship and small rotations. Following that, de

Souza (2000) extended the material nonlinear force-based element proposed by Neuenhofer and Filippou (1997) to include geometric nonlinearity through deriving the transverse displacements from the curvatures using Lagrangian polynomial interpolation. The adopted kinematics is based on the assumption of moderately large deformations along the element, thus rigid body displacements and rotations can be arbitrarily large. However, at the price of further subdividing the structural member into smaller elements, large deformation problems can also be solved.

In the analysis of frame elements, the material nonlinearity is considered by integrating the material stress-strain relations defined for each fiber over the section area, which is commonly referred to as "fiber discretization". Distributed plasticity is obtained by integration of the section force-deformation response over the member length in the corotating frame of reference. As shear effects are neglected, a uniaxial stress-strain relation is employed at the material point. The effect of spreading of plastic deformation along the member axis is thus considered in this study.

The following equation of motion is used for nonlinear time history analysis,

$$M\ddot{U}(t) + C\dot{U}(t) + R\big(U(t)\big) = P_f(t) \tag{5-1}$$

Where the first term is the acceleration-dependent inertial force vector, R is the displacement-dependent restoring-force vector. $P_f(t)$ is the external applied-force vector.

The standard approach for dynamic collapse analysis, as well as other nonlinear structural dynamic problems, is to time discretize the governing equations by

Newmark time integration then solve them via the Newton-Raphson algorithm (Scott and Fenves 2010). In this study, the Newmark constant average acceleration method (β=0.25 and γ=0.50) is employed. This requires that iteration must be performed at each time step in order to satisfy equilibrium. Also, the incremental stiffness matrix must be formed and triangularized at each iteration or at selective points in time.

5.3. Numerical analysis model

A finite element analysis software program – OpenSees (McKenna and Fenves1997) was used in this study. This section describes the modeling technique for dynamic member buckling and self-centering fuse members in the numerical simulation of the nonlinear dynamic behavior of the steel arch structure under earthquake loading.

5.3.1. Analytical model for dynamic member buckling

Modeling of the buckling behaviour of steel bracing members has been examined by a number researchers (e.g., Jin and El-Tawil 2003; Uriz *et al*. 2008; Krishnan 2010). An initial imperfection has to be assigned to the axially loaded member to simulate its buckling behaviour. However, few studies have considered the dynamic buckling effect of a compression member caused by the mid-point-inertia-mass (mid-mass)-induced lateral force at its mid-length (Tada and Suito1998).

The member under examination is a steel tube (O.D= 6.26 in (159 mm), I.D= 5.78 in (147 mm)) with a material yield strength of 34 ksi (235 MPa). The member length is set to be 76.7 inches (1.95 m). To capture the inertia effect on member dynamic

buckling, a lumped mass which represents half the mass of the member is assigned to the middle-length point of the member following a procedure described by Tada and Suito (1998). A parametric study has been conducted and the results revealed that a finer meshed model has very little effect on the member behavior. Therefore, a single mass lumped at mid-length was used in all cases. The end conditions are specified as pin-roller supported, as shown in Figure 5-1. Thus, the member was divided into two inelastic beam-column elements with an initial camber of 0.1% at the mid-node of the member in the finite element model.

In this element, fiber discretization was used and the force components were obtained by integration over the cross-section. The tubular section of the member was discretized into two layers of fibers in the radial direction and 20 fibers in the circumferential direction respectively. As shear effects are neglected, a uniaxial stress-strain relation is employed at the material point. The material properties for the simulation model are based on the Menegotto-Pinto model for steel with extensions for kinematic and isotropic hardening (Filippou *et al*. 1983) with the following values: Young's modulus = 29,000 ksi (200 GPa), yield stress = 34 ksi (235 MPa), and strain-hardening ratio = 0.005.

Figure 5-2(a) shows the load-displacement (P-Δ) relations of the member under cyclic load, P. Due to the initial camber introduced at the mid-length point, the member is subjected to second-order bending effect. At a critical value of Δ, once the second order bending moment at the mid-length point reaches the member's plastic moment capacity, a plastic hinge with spread plasticity would form there. Further

pushing the member in the longitudinal direction would result in the spreading of the plastic deformation near mid-length region and reduction in load.

5.3.2. Analytical model for Force Limiting Device (FLD)

Fuse members with a long plateau of member ductility can be used for ductility enhancement in steel arch structures by fitting them to substitute critical compression members. The fundamental concept behind fuse members is to restrain low-order member buckling modes, creating full and stable hysteretic loops under tension-compression cyclic load. For example, with the use of such fuse members as buckling restrained braces (Uang and Nakashima 2003), member buckling can be held off till a fairly large compressive strain, without significant strength degradation.

In numerical modeling of self-centering fuse members, a simple, one-dimensional, pin-ended truss element is used to have the appropriate uniaxial force-displacement properties. This is based on the Menegotto-Pinto model for steel with extensions for kinematic and isotropic hardening (Filippou *et al*. 1983). Flag-shaped hysteretic model, as shown in Figure 5-2(c), has been widely used to represent the cyclic loading behavior of self-centering system for sake of its simplicity (e.g. Christopoulos *et al* 2002; Seo and Sause 2005; Zhu and Zhang 2008). Two key parameters that define this flag-shaped hysteretic model are post-yield stiffness ratio α and energy dissipation factor β that relates to the energy dissipation capacity of the system. For example, its lower bound (i.e., $\beta = 0$) describes a piecewise nonlinear elastic system while the upper bound (i.e., $\beta = 1.0$) corresponds to a self-centering system with greatest possible energy dissipation capacity. For a given system with known initial

stiffness and yield strength, the flag-shaped hysteretic model can be completely defined with these two parameters - α and β. In this study, β value is set as 0.5 and α value is set as 0.05.

For comparison purpose, conventional fuse members exhibiting bilinear hysteresis are also considered in this study and its typical hysteresis loop is shown in Figure 5-2(b). The hysteresis loop of the conventional fuse member was calibrated with the experimental data reported by Clark *et al*. (1999).

5.4. Seismic analysis

An arch truss is selected as the prototype structure, as shown in Figure 5-3. The member's sizes of this arch structure are listed in Table 5-1. The dead loads applied to the arch truss nodes include its self-weight and the gravity load due to enclosure coverings. The self-weight of the arch truss is calculated to be 20 lbs/ft (0.29 kN/m) and the additional dead load is 11.23 psf (0.47 kPa). The total dead load is thus equal to 11.4 psf (0.55 kPa). The dead loads for the arch spaced 19.7-ft (6 m) apart is then converted into concentrated load applied to the top chord nodes. The lumped mass assigned to the top chord nodes are determined based on the corresponding dead loads. The natural frequencies of this arch structure are calculated from the finite element model and listed in Table 5-2. The viscous damping ratio of the arch structure is assumed to be 2%. Figure 5-4 shows the first three mode shapes for this arch structure. Members were modeled by subdividing into two beam-column elements, as illustrated in Figure 5-1. A 0.1% camber of the original member length was assumed for their initial imperfections.

Four cases were considered in this analysis. First case is the original structure without fuse members (labeled as "Original"). Second case is an arch structure with conventional fuse members (FM) on locations shown in Figure 5-3(b) (labeled as "Conv. FM"). Third case is an arch structure with self-centering fuse members (energy dissipation factor $\beta = 0.5$; cross-section of fuse members reduced to 70% of its original strength to create a weakened zone) which is labeled as "SC 0.5-A". The fourth case is an arch structure with self-centering fuse members (but the size of all members are increased by 1.33 times compared to case "SC 0.5-A") which is labeled as "SC 0.5-B". In practice, the case "SC 0.5-A" could represent a retrofit for an existing structure by substituting critical members with self-centering fuse members while the case "SC 0.5-A" might be a new design with weakened self-centering hinge zone. The location of fuse members are indicated in Figure 5-3(b). The supports at node L1 and L6 are pin supported.

Some explanations are in order for the adopted strategy in selecting the locations of self-centering fuse members which collectively would create self-centering hinge zones at particular region. For example, three neighbouring self-centering fuse members (one upper chord, one lower chord, one web diagonal) could form a self-centering hinge zone in a truss.

Note that the strength of the self-centering fuse members was reduced to 70 % of the critical load (i.e., buckling force) of a compression member with imperfection (around 40% of its original strength). Although the reduced member strength is lower than the critical load, it is worth noting that self-centering member still maintain a stable load carrying capacity and stiffness after 'yielding' while after member

buckles, both strength and stiffness of regular members degrade rapidly. This is the essential distinction between using weakened self-centering members and regular buckled member even though the critical load for the buckled member is slightly greater. This distinction leads to the favorable behavior of steel arch structure with self-centering members.

An analysis has been conducted to demonstrate the benefit of the fuse member selecting and weakening strategy. The nonlinear dynamic analysis on the original structure without fuse members under 20 earthquake records was conducted. For each earthquake record, the member failures were counted and listed in Table 5-3. The failure occurrence varies from 1 to 11. And after check, it's found that 31 locations have ever failed under at least one earthquake records. The failure locations are indicated in Figure 5-5, where are marked in red. Due to the uncertainty of occurrence of earthquakes, it's needed to consider these 31 members as possible failure locations after an earthquake disaster. The numbers of failure occurrences are also indicated on each failure location. It can be seen that failure occurrence on member L1L2 and L3L4 are 10 and 11 respectively. Thus these two locations are selected as fuse member locations. By incorporating weakened FLD member as fuse member, the damages can be concentrated only on the four pre-selected members and thus bring the ease to inspect and replace damaged member after earthquakes.

5.4.1. Nonlinear static analysis

Nonlinear static analysis provides an insight into the expected seismic performance of the structure under specified lateral load profile. A pushover analysis of the arch truss was performed to identify the nonlinear static response of the arch structure with self-centering fuse members. The inverted triangular vertical load pattern was used to distribute the base shear at several nodes on outer chords along the height of the arch in pushover analysis according to its first mode shape. The loads were increased monotonically until the horizontal displacement at the top node of the arch structure reached to the drift ratio of 2%.

The roof drift ratio (top node displacement divided by the overall height of the arch structure) vs. the base shear also known as pushover curve, recorded during the nonlinear static analysis is shown in Figure 5-6. It is seen that the slope of the post yield branch of the pushover curve changes as the chord members enter buckling phases. During the analysis, the base shear increases linearly until the roof drift ratio reaches about 0.5% and the base shear reaches 189 kN. Then the base shear decreases quickly as the drift ratio continues increase, suggesting the arch structure losing load carrying capacity and fail. On the contrary, the base shears for the three arch structures with fuse members did not degrade after the turning point. Case SC 0.5-B shows that by increasing all members 1.33 times than SC 0.5-A, the base shear turning point can be increased to a level comparable to the original structure. After checking member responses, members L4L5 was found to buckle in case Original case. This cause the base shear drops at around 0.5% drift ratio. However, after member L4L5 buckled, no other members yield or buckled. It's seen from the Figure

5-6 that no strength or stiffness degradation in the case SC 0.5-A and SC 0.5-B. This implies that no other members buckled after the base shear turning point in the two SC cases. The post yielding stiffness for Case Conv. FM is lower than two SC cases because the material for the fuse member has lower strain-hardening ratio. The stiffness of Case SC 0.5-B before yielding is slightly lower than the original case due to the reduced section for those fuse members compared to the substituted members in the original case.

5.4.2. Nonlinear time history analysis

The performance of a structural system under strong earthquakes can be evaluated by examining the nonlinear time history analysis results of the key engineering demand parameters (EDPs). For this purpose, nonlinear time history analysis of the arch structure was performed under a suite of 20 strong earthquake records, which were originally developed by Somerville *et al*. (1997) for the Los Angeles, California region with a probability of exceedance of 2% in 50 years. These scaled earthquake records correspond to the maximum credible earthquake of the downtown Los Angeles area. Details of these earthquake records are listed in Table 5-4. These acceleration time histories have been derived from historical recordings or from physical simulations and have been altered so that their mean response spectrum matches the 1997 NEHRP design spectrum, modified from soil type of S_B-S_C to soil type S_D and having a hazard specified by the 1997 USGS maps. The pseudo-acceleration response spectra for these earthquake records are shown in Figure 5-7. The time interval is set as 0.001 seconds for the time history analysis.

5.5. Results and discussions

The results of important EDPs are presented in this section. In the results presented in this sections, the 'peak' result refers to the highest absolute value of the specified parameter (e.g. drift ratio, etc.) recorded during the time history analysis. The "ensemble average" refers to the mathematical average value of the results obtained from the twenty time history analyses which is shown in some figures.

Figure 5-8 shows the peak and residual arch top displacement responses of the arch structures under the twenty seismic records. It's seen that use of conventional fuse members decreases the average peak displacement response from 0.37 m for the original structure to 0.35 m for the Conv. FM case. However, the Conv. FM case is seen to have 0.027 m residual displacement on average, while the original structure case has 0.09 m residual displacement on average. It is observed that self-centering fuse members can significantly decrease the residual displacement response to zero. Case SC 0.5-A has slightly higher average peak displacement response than the original structure case due to reduced fuse member section sizes and thus global stiffness of the arch structure. Average peak displacement for Case SC 0.5-B is 0.38 m, which is lower than that of Case SC 0.5-A.

Figure 5-9 shows the peak base shear and arch top acceleration response of the arch structures under the 20 earthquake records. It's seen that the all three cases with fuse members have lower base shear force than the original structure. Use of fuse members decreases the base shear force from 200 kN for the original structure to around 162 kN for the conventional FM case. The base shear forces for two self-

centering fuse member cases are quite close. Use of fuse members also decrease the peak arch top acceleration response from 10.4 m/s^2 for the original structure case to 8.96m/s^2 for Case Conv. FM and 9.15 m/s^2 for Case SC 0.5-A . The average peak arch top acceleration for Case SC 0.5-B is 9.9 m/s^2, which is still lower than the original structure.

Since it is not possible to present all detailed results of all time history analyses, LA11 is chosen as a representative case for the nonlinear time history analysis and some of its detailed time history results are presented here. Figure 5-10 shows the displacement time histories of node U3, which has the largest displacement response and thus is used as a reference point. For the original structure case, its peak horizontal displacement response reaches 0.52 m. It is seen that there is a sharp downward turn in the displacement response curve, indicating occurrence of member failure around 5 seconds. After checking member responses, members L4L5 was found to buckle at that moment and thus cause the sudden horizontal motion. This also led to the 0.23-m residual displacement observed at the end of seismic record duration in the original arch structure. It is worth noting that strength reduction has been intentionally made in the fuse member members in order to activate these members for energy dissipation and control of member forces. Consequently, this leads to reduced load demand on their neighbouring members and thus prevents the failure of these members. However, due to its bilinear hysteresis, a residual displacement as large as 0.03-m is observed for the conventional fuse member case in Figure 5-10. In order to minimize the residual displacement, the self-centering fuse members are used and the corresponding results are shown in Figure 5-10.

Figure 5-11 show the horizontal acceleration of node U3 for all four cases. The use of both conventional fuse members and self-centering fuse members is able to decrease the acceleration response of the arch structure. Clearly, incorporating fuse members into the steel arch structure can effectively control its seismic responses under strong earthquake loading.

5.6. Conclusions

This research presents the results of nonlinear dynamic analysis of steel arch structures subjected to earthquake load. Both material and geometric nonlinearities are considered in the simulation study. A 2-dimensional force-based element with corotational formulation and fiber discretization of the cross section is used to simulate member buckling and associated strength degradation and large. Four cases were considered for the arch structures, distinguished by the type of fuse members they used or no fuse members: Original Structure without any fuse members, Conventional fuse members, self-centering fuse members (two cases: SC 0.5-A and SC 0.5-B). The fuse members are installed at strategically selected locations to substitute critical members, and designed to provide a high level of member ductility. Through weakening of the steel arch structure by using fuse members of reduced strength (about 30% to 40% of their original member strength), deformation and energy dissipation can be concentrated to a pre-selected self-centering hinge zone formed by the fuse members while the entire arch structure's integrity is retained during strong earthquake event. Findings from this study include:

(1) Installing fuse members at intentionally weakened locations in steel arch

structures can effectively control the displacement response of the arch structure under earthquake loading. Unlike the original critical member susceptible to buckling, the fuse member could maintain its strength and exhibit ductile load behaviour. The strengths of fuse members usually have to be reduced (compared to the critical load of its original substituted member) to prevent the failure (e.g., buckling) of their neighboring members in the arch structure. The structural weakening strategy can concentrate the ductile damage of the overall structure on the selected favorable locations where are easy for damage inspection and structural repair post earthquake events.

(2) The use of conventional fuse members exhibiting bilinear hysteresis results in residual displacement in the steel arch structure. Self-centering fuse members with flag-shaped hysteresis is very effective to eliminate the residual displacement.

(3) As an alternative that could be used for new design, all the member size could be proportionally increased as demonstrated by Case SC 0.5-B. It's seen that the global structure strength is increased to the same level as that of the original structure. By doing so, the displacement response of the arch structure can be further reduced without any residual displacement after strong earthquake events.

Table 5- 1. Section sizes of the arch structure's tubular member

Member	Outer diameter, OD (mm)	Tube Wall Thickness (mm)
F1	75.5	3.75
F2	88.5	4
F3	114	4
F4	140	4.5
X1	88.5	4
X2	114	4
X3	140	4.5
X4	159	6
X5	159	8
S1	159	6

Table 5- 2. Natural frequency of the steel arch structure with and without fuse members (unit = Hz)

	1^{st} mode	2^{nd} mode	3^{rd} mode	4^{th} mode	5^{th} mode	6^{th} mode
Original	0.706	1.724	3.424	4.975	6.667	7.092
Conv. FM	0.626	1.618	3.425	4.831	6.329	6.711
SC 0.5-A	0.625	1.617	3.424	4.829	6.325	6.701
SC 0.5-B	0.688	1.726	3.817	5.405	7.246	7.634

Table 5- 3. Numbers of member failures under each earthquake records

Code	No. of members failed	Code	No. of members failed
LA01	5	LA11	7
LA02	2	LA12	2
LA03	7	LA13	8
LA04	3	LA14	5
LA05	7	LA15	2
LA06	2	LA16	2
LA07	1	LA17	6
LA08	2	LA18	11
LA09	10	LA19	1
LA10	9	LA20	5

Table 5- 4. Earthquake ground motion records used in this study (scaled to the maximum credible earthquake for Los Angeles, California)

Code	Original EQ. Record	EQ. Magnitude	Epicentre Distance (km)	Scale Factor	PGA (cm/s^2)	Vertical PGA (cm/s^2)
LA01	Imperial Valley, 1940, El Centro	6.9	10	3.02	678.05	494.25
LA02	Imperial Valley, 1940, El Centro	6.9	10	3.02	994.32	724.79
LA03	Imperial Valley, 1979, Array #05	6.5	4.1	1.52	579.06	422.09
LA04	Imperial Valley, 1979, Array #05	6.5	4.1	1.52	717.98	523.36
LA05	Imperial Valley, 1979, Array #06	6.5	1.2	1.26	443.54	323.31
LA06	Imperial Valley, 1979, Array #06	6.5	1.2	1.26	345.12	251.57
LA07	Landers, 1992, Barstow	7.3	36	4.80	619.47	665.59
LA08	Landers, 1992, Barstow	7.3	36	4.80	626.24	672.86
LA09	Landers, 1992, Yermo	7.3	25	3.26	764.55	821.47
LA10	Landers, 1992, Yermo	7.3	25	3.26	530.03	569.49
LA11	Loma Prieta, 1989, Gilroy	7	12	2.69	978.74	713.43
LA12	Loma Prieta, 1989, Gilroy	7	12	2.69	1426.40	1039.75
LA13	Northridge, 1994, Newhall	6.7	6.7	1.55	997.40	730.59
LA14	Northridge, 1994, Newhall	6.7	6.7	1.55	966.74	708.13
LA15	Northridge, 1994, Rinaldi RS	6.7	7.5	1.19	784.95	574.97
LA16	Northridge, 1994, Rinaldi RS	6.7	7.5	1.19	852.87	624.72
LA17	Northridge, 1994, Sylmar	6.7	6.4	1.49	837.65	613.57
LA18	Northridge, 1994, Sylmar	6.7	6.4	1.49	1202.16	880.57
LA19	North Palm Springs, 1986	6	6.7	4.46	1499.15	1092.78
LA20	North Palm Springs, 1986	6	6.7	4.46	1451.42	1057.99

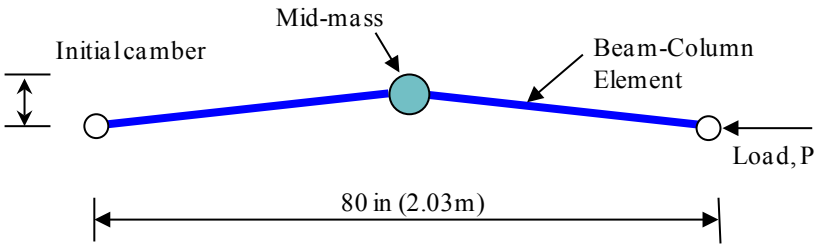

Figure 5- 1. Configuration of brace model considering mid-length mass

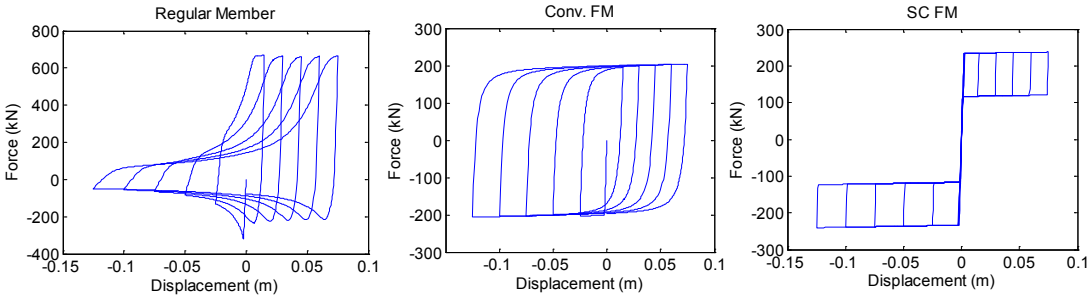

(a) Regular member (b) Conventional FM (c) Self-centering FM

Figure 5- 2. Hysteresis model of buckled member, conventional fuse member (FM) and self-centering FM

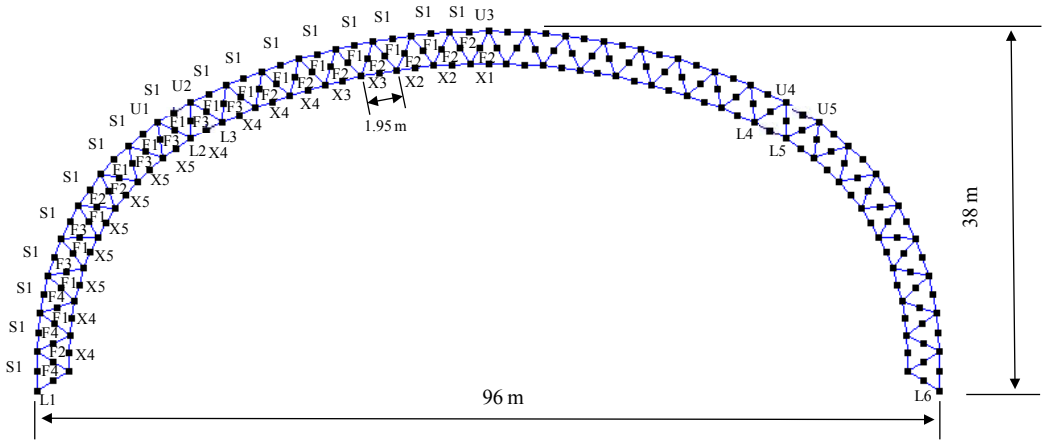

(a) Elevation view (without fuse members)

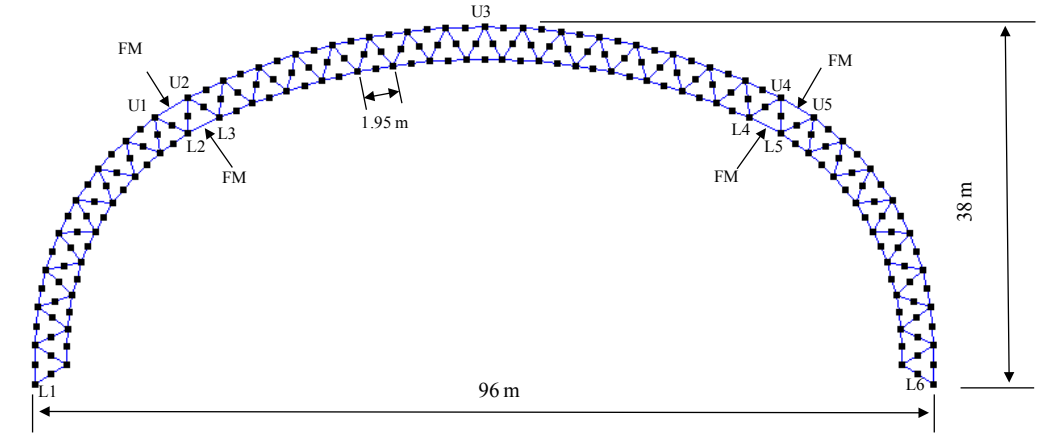

(b) Elevation view (with fuse members)

Figure 5- 3. Schematics of steel arch structure and location of fuse members

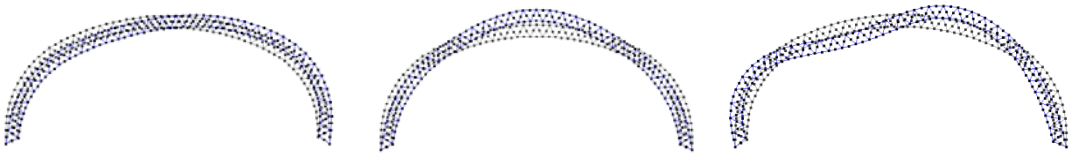

(a) 1st mode (0.706 Hz) (b) 2nd mode (1.724 Hz) (c) 3rd mode (3.424 Hz)

Figure 5- 4. First three mode shapes of the arch structure

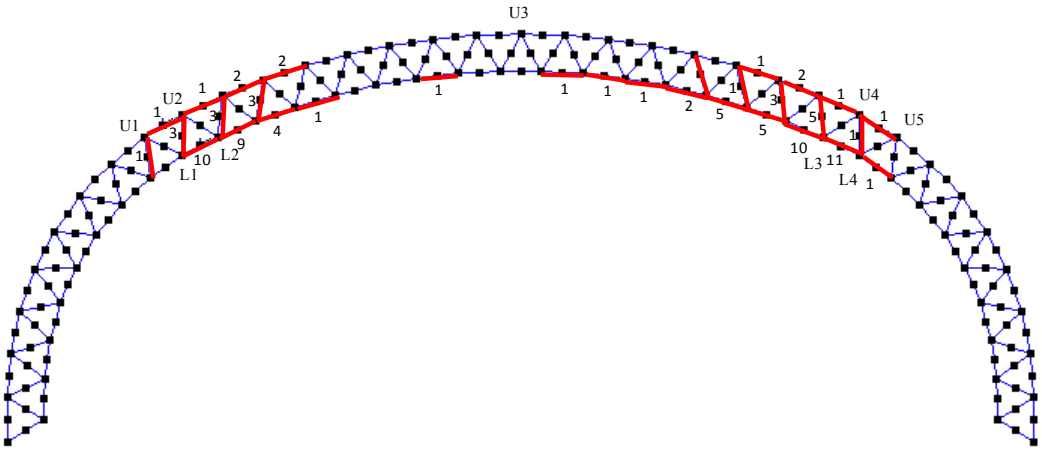

Figure 5- 5. Locations of member failure under 20 earthquake records. (Numbers indicate the member of failure occurrences in total 20 earthquakes.)

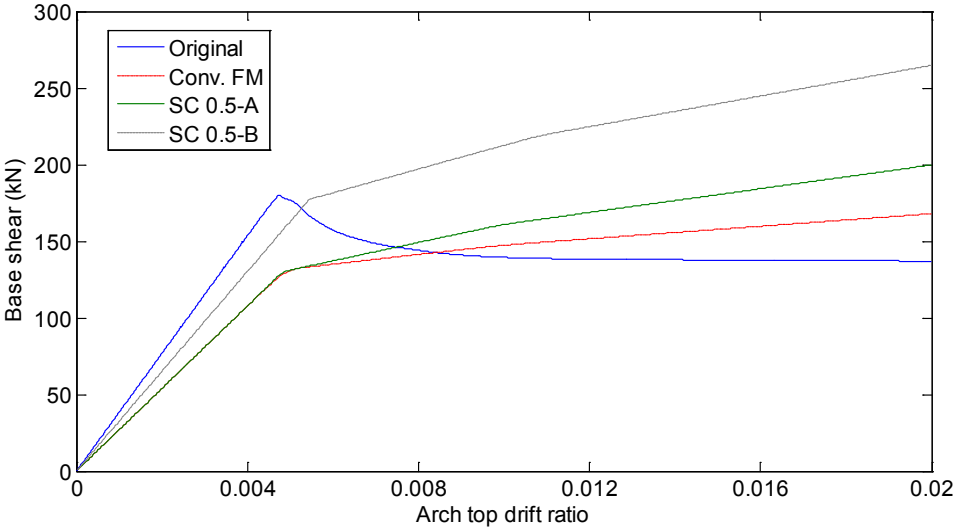

Figure 5- 6. Static pushover curve of the arch structure

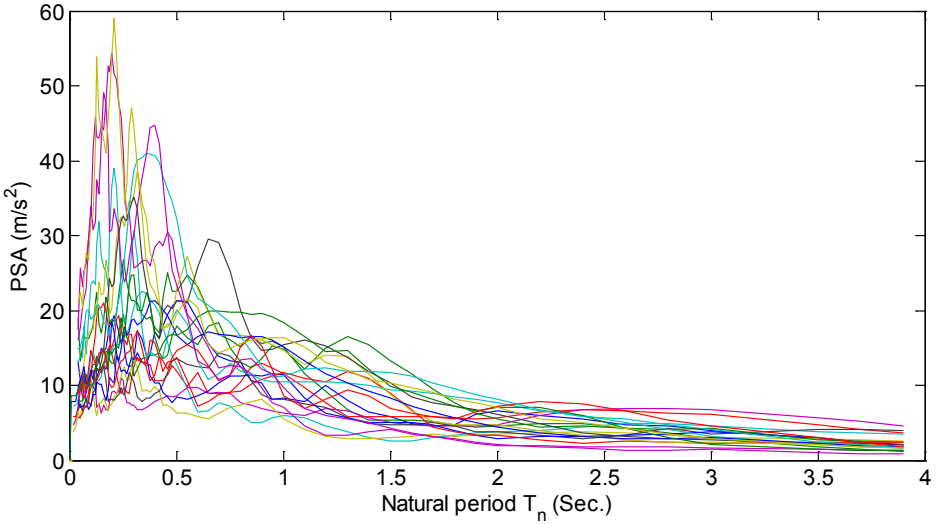

Figure 5- 7. Pseudo-Acceleration response spectra of the seismic records in Table 5-4 (viscous damping ratio=0.05)

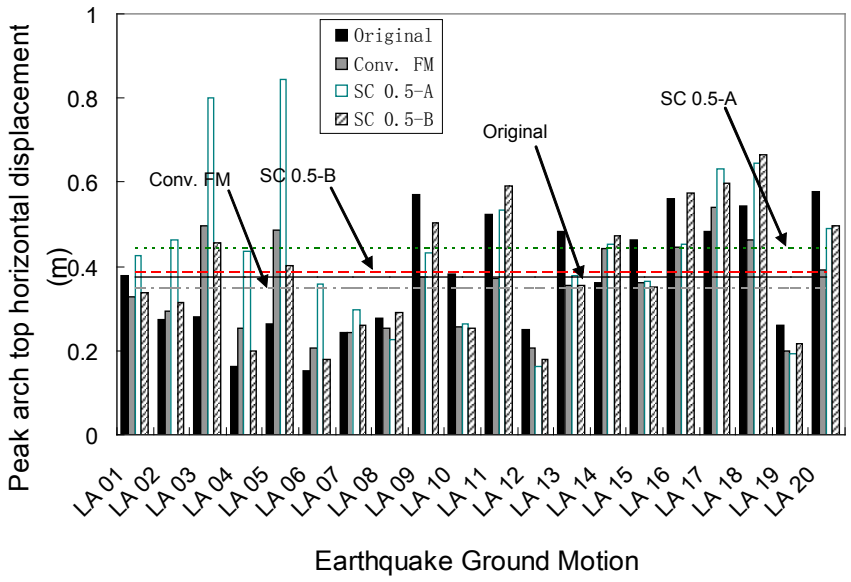

(a) Peak arch top displacement

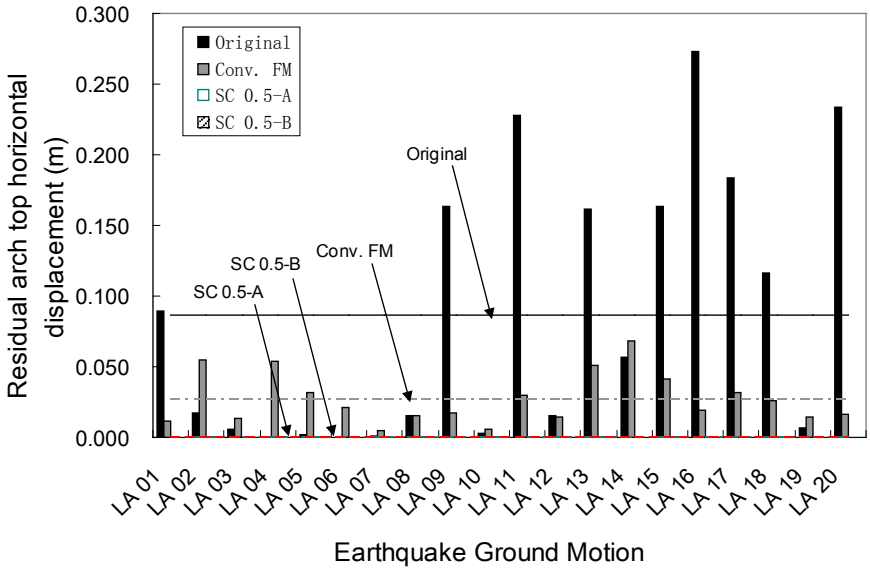

(b) Residual arch top displacement

Figure 5- 8. Peak and residual arch top displacement of the arch structure

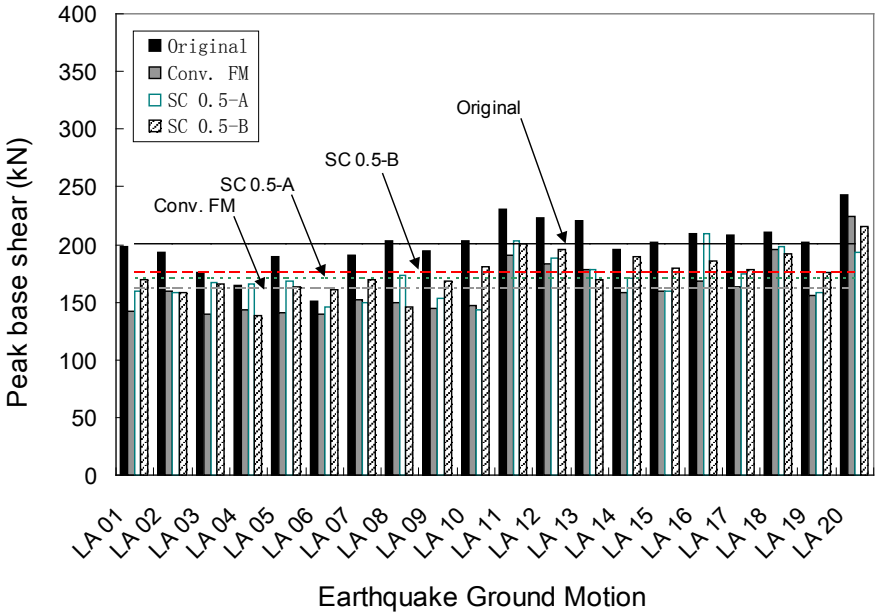

(a) Peak base shear

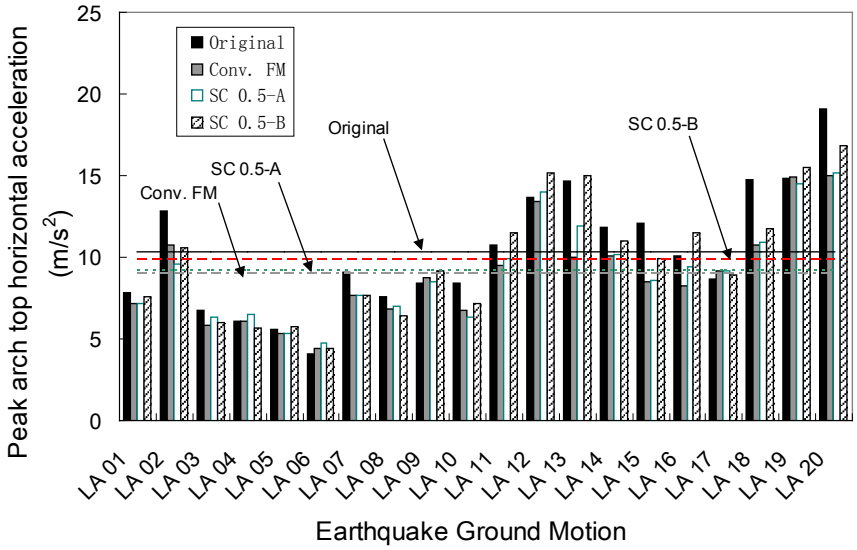

(b) Peak arch top point acceleration

Figure 5- 9. Peak base shear and acceleration response of the arch structure

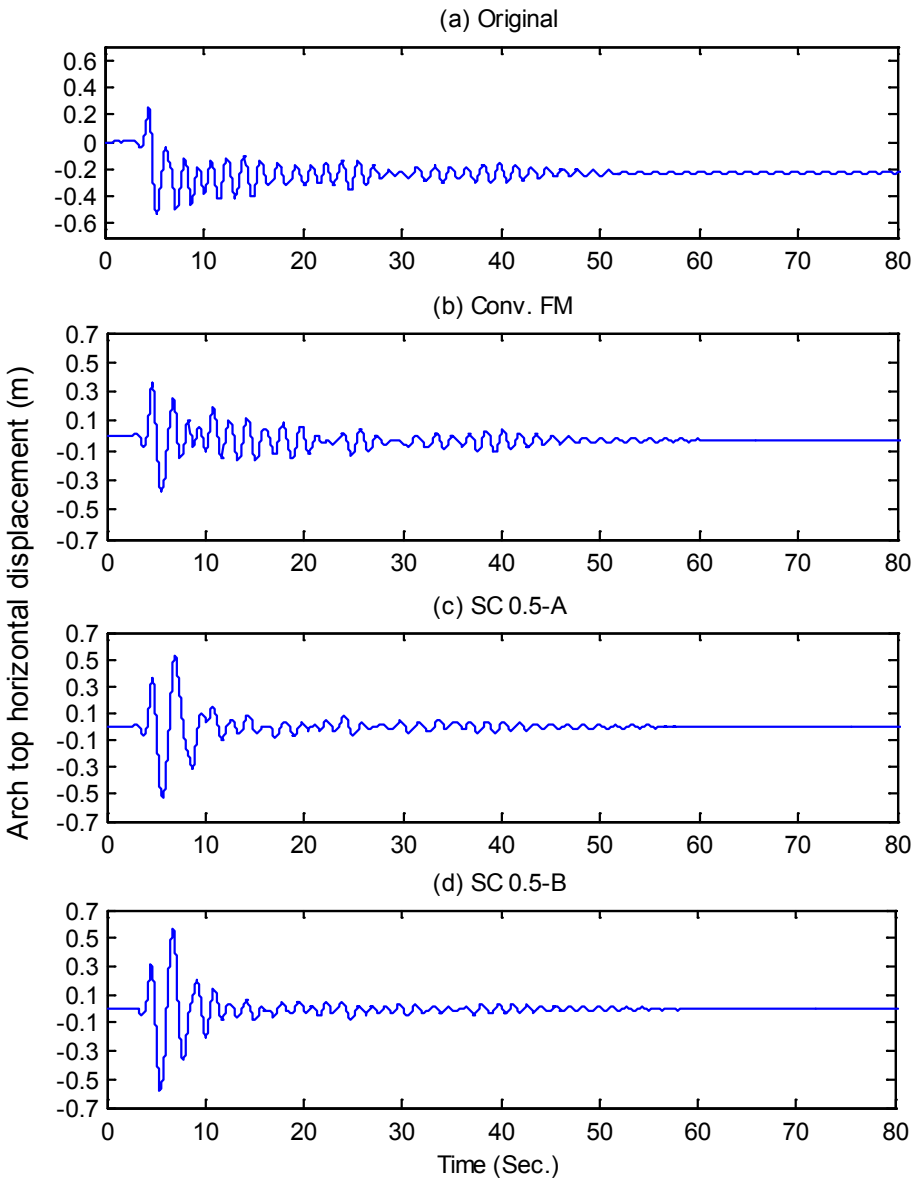

Figure 5- 10. Displacement response of the arch structure under LA11 record: horizontal displacement at arch top node U3

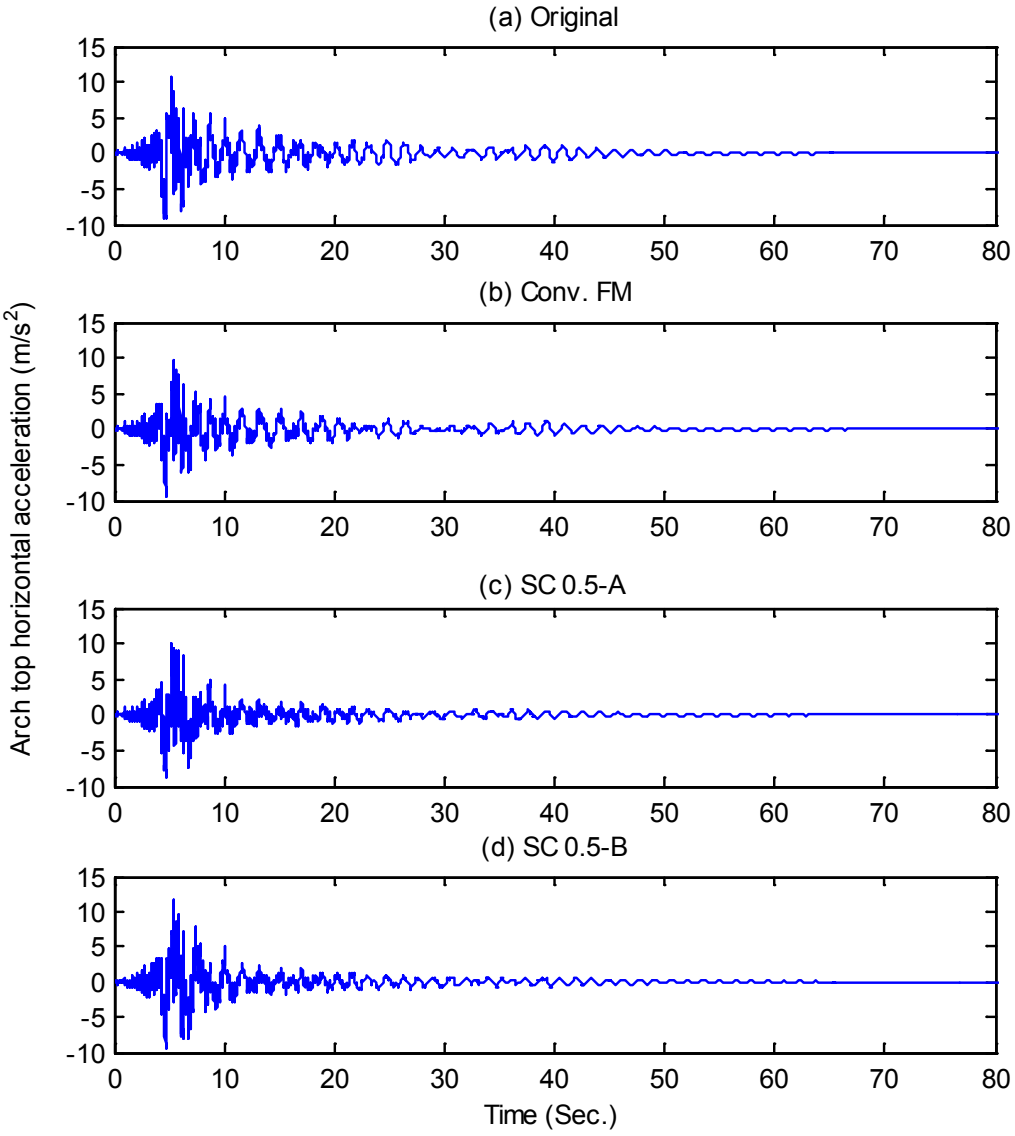

Figure 5- 11. Acceleration response of the arch structure under LA11 record: Horizontal acceleration at arch top node U3

Chapter 6: Case Study I: Demonstration of WSCA System on Truss Structure

6.1. Introduction

In this chapter the implementation of the wireless structural condition assessment (WSCA) system will be demonstrated on a truss structure through experimental test. After the BT strain sensors were validated using the countertop test setup described in Chapter 3, it's natural to further test the performance of the WSCA system on a more realistic structure in order to accomplish the following three goals: (i) validate the BT strain sensors installed on a large-scale structural member in a structure subjected to load; hybrid simulation test will be conducted for this purpose; (ii) investigate the various aspects of the WSCA system including the integration of the wireless sensors (e.g., BT strain sensors) and the BIM-based computing environment; (iii) validate and evaluate the performance characteristics of the BIM based WSCA system in a real structure setting such as demonstrating its capability of quickly locating and visualizing the strain in the selected members.

To faithfully capture the essential structural behavior of monitored structure on which the sensor will be installed and its performance will be evaluated, it is desired that the test structure shall be fabricated at or near full scale. Conventional testing technique for experimentally evaluating structures usually involves fabrication of large-scale structural assembly and simplification of loading patterns on the test structure. While this is a proven method of testing, it is very costly and requires the use of testing

equipments that are available at limited number of large-scale testing facilities across the country. A hybrid simulation method provides a more efficient and cost effective alternative to conventional testing methods.

The use of this hybrid simulation method for structural condition assessment will be demonstrated through assessing the truss structure with tubular members in this chapter. Specifically, Section 6.2 describes the hybrid testing methodology. The details of the test setup for the hybrid simulation test conducted on the truss structure are given in Section 6.3. The WSCA implemented on the truss structure under hybrid simulation test and its performance observed during the test is discussed in Section 6.4.

6.2. Experimental test: hybrid simulation

The concept behind hybrid testing of a large scale structure like a roof or bridge truss is that a large portion of the structure can be easily simulated using the fundamental behaviors of the materials and geometries of the structural elements. However, certain parts of the truss may be difficult to numerically model and simulate (such as a truss member susceptible to buckling). Hybrid testing solves this problem by combining experimental testing of the large scale truss member susceptible to structural damage with a computer model that simulates the remainder of the structure and external loading. By experimentally testing the selected member of the truss structure, a more realistic and controlled testing environment can be applied in testing structural members at large scale and validating structural sensors.

The prototype truss shown in Figure 6-1 has a span length of 14.7 ft (4.47m). A 3D model of the prototype truss was built in Revit. An overall view of the Revit model of the truss is shown in Figure 6-1. It's noted that only the experiment member indicated in the figure will be tested while other members will be simulated in the FE software. Concentrated load was applied at the mid-span joint of the lower chords and the load was monotonically increased until the upper chord failed or the BT strain sensor mounted on the physically tested truss member was triggered. Strain gages were also installed on the test truss member. During the test, synchronized recording of the strain gage and BT strain sensor data was carried out until a threshold strain exceedence signal is received from the BT strain sensor.

6.2.1. Software architecture for hybrid simulation

To perform hybrid simulation test, a software framework needs to be first established to integrate the physical testing elements with the computer model. Figure 6-2 shows the architecture of such a software framework that depicts its basic components and their interrelationships. The requirements for this middleware software framework are: ease in operation, and compatibility with different types of experimental system. It shall allow researchers to carry out hybrid simulation without specialized knowledge about the underlying software. Also, it shall enable any interested user to custom develop and extend it to other field by adding new control system, application model, and integration modules.

During a hybrid test, the first task for the software framework is to transform the degree-of-freedoms from the coordinate system of the finite element (FE) software to

those of the test specimens being physically tested, by considering the geometry and kinematics of the system. Subsequently, another class is responsible for communication between the laboratory control and data acquisition systems. For geographically distributed hybrid testing, another class is needed to facilitate the communication between distributed experimental sites and the master site which runs the computational software and works as the coordinator in the test (Schellenberg *et al*. 2009).

OpenFresco is one of the hybrid test software frameworks which have a modular architecture. Each module can be modified and new ones can be added without affecting other modules. In OpenFresco, a module is called a class, including ExperimentalElement, ExperimentalSite, ExperimentalSetup and Experimental-Control classes. The relationship between these classes is shown schematically in Figure 6-2 (Schellenberg *et al*. 2006a, 2008).

OpenFresco is independent of the FE software used, meaning that any FE software that allows the addition of new elements can be used, such as Abaqus, LS-Dyna, OpenSees, Matlab, etc. For example, OpenSees can be readily used with OpenFresco because of its object oriented design methodology. Unlike a pure numerical analysis conducted in OpenSees, the difference in hybrid testing is to replace the numerical element with the ExperimentElement from OpenFresco and add the numerical integration operators (Schellenberg *et al*. 2006b).

6.2.2. Hybrid simulation test setup

Hybrid simulation seamlessly combines the analytical and physical parts of a

structure and simulates their response with a number of advantages over traditional large scale structural testing method. In contrast to a conventional numerical simulation, in which the entire structure is modeled numerically, the hybrid testing method obtains some of the forces corresponding to either restoring force or damping from a concurrent physical test performed on the real structure or selected components. The hybrid testing method therefore gives the researches the flexibility to model the well understood parts of a structure using a FE program on a computer, leaving the construction and testing of a component that is the highly nonlinear and/or numerically difficult to model to physical parts of the structure in the laboratory.

A hybrid simulation test setup to simulate the nonlinear response of large scale frame structures under severe transient loadings (e.g., extreme wind load from downburst) established at the University of Maryland (UMd) is shown in Figure 6-3. The goal of this hybrid simulation test setup is to investigate and validate the application of hybrid simulation method to faithfully reproduce the truss member damage behavior such as buckling and effect on the collapse of full-scale metal frame structures under transient loading. The UMd hybrid testing system is based on the sub-structuring pseudo-dynamic testing concept, in which the dynamic behaviour of the test structure is simulated on a computer by solving the equations of motion during the test using the structural restoring forces measured from the nonlinear substructure being physically tested. The hybrid testing system combines physical testing and model-based simulation in a flexible manner for an efficient and realistic evaluation of the nonlinear behaviour of a structural system subjected to extreme loading or dynamic excitation.

This hybrid simulation test setup had been demonstrated the capability of hybrid testing technique in faithfully capturing the post-buckling behaviour of a long span arch truss structure subjected to transient wind loading. The details about these validations tests can be found in the work by Bai and Zhang (2010). This hybrid simulation test setup was also used in the present experimental study on the WSCA system installed for the prototype truss. However, monotonic loading was applied on the truss for simplicity.

In this hybrid simulation system, the OpenFresco software framework for hybrid simulation is used along with an MTS FlexTest 60 controller and hybrid testing driver. The OpenSees software program is used to solve for the displacement vector satisfying the governing equation of motion of the structural model at each time step. The hardware part of the hybrid testing system include: three MTS actuators with servo-control (two 55-kips (244 kN) double-rod actuators with 30-GPM (114L/Min) servovalve, a 60-GPM (227 L/Min) hydraulic power supply, three 50-GPM (189 L/Min) hydraulic service manifolds, a 4-channel servo-control system with FlexTest 60 controller and MTS test software.

The advantages of using hybrid simulation to assess the ultimate structural behavior (e.g., collapse) of structural systems are numerous: physical masses are removed from the experimental setup as they are modeled numerically, improving the safety of the tests, especially at imminent collapse stage; the specimens can be tested at large scale; only the vulnerable substructure (e.g., buckled member) is tested experimentally while the remaining structure is modeled numerically, thus improving the economy of the tests; etc. Those benefits make hybrid simulation test a safe, efficient and less

expensive alternative for experimental evaluation of ultimate structural behavior (Wang *et al*. 2009).

6.3. Component validation test on truss member

Before conducting a full scale hybrid simulation test, a validation test with a simple test setup is needed to validate and debug the BT strain sensor which is now installed on a large scale structural member. This simple test setup includes a truss member made of Poly (vinyl chloride) (PVC) tube under monotonic loading. This PVC tube has an outer diameter of 4.5 inches (11.43 cm) and an inner diameter of 4 inches (10.16 cm). The length of the PVC tube is 2 ft (0.61m). The modulus of elasticity of the PVC material was measured to be 160 ksi (1.1 GPa).

The test setup of this component validation test is shown in Figure 6-4. The test setup includes the following components: 2 strain gages (Vishay model #: EA-06-250AE-350), BT strain sensor with RFID tag antenna, UHF RFID reader (Skyetek model #: SkyeModule M9). The universal test machine used for this test is a SATEC 400-kips (181.4 kN) servo-hydraulic test machine (serial #: I-series 400BTE/483280). As shown in Figure 6-4, the Skyetek RFID reader was placed at a distance of 75 inch (190.5 cm) away from the PVC tube. Two strain gages were bonded to the mid-length point of the PVC tube to measure the axial strain of the PVC tube during the test. The two strain gages are positioned at 180º from each other along the circumference of the tube to cancel out any eccentricity induced strain if there is any. The strain gages also provide a calibration tool for the BT strain sensor by comparing synchronized recordings of each other. A video camera was used to record the strain reading during

the test in order to identify when the RFID tags were triggered. The RFID tags were connected to the BT strain sensors using AWG 26 ribbon wires, as shown in the inset of Figure 6-4.

The BT strain sensors were directly cut from a 6 by 12 inches (15.24 by 30.5 cm), 0.08 inches (2 mm) thick acrylic sheet using a carbon dioxide laser cutter (CO2 cutter). The distance between the two end fixtures of the BT strain sensor is 2 inches (5.08 cm), which is considered as the gage length *Ls* of the BT strain sensors. The dimensions of the BT strain sensors are shown in Figure 6-5. As reported in Chapter 3, FE simulation is conducted to find out the maximum axial deformation in the sensor that will break the brittle bar. As aforementioned, BT strain sensor failure is defined as the maximum first principal strain in the BT strain sensor first exceeds 3%. The design values for H9W2 and H6W4 from the FE analysis are listed in Table 6-1. These design values are calculated by dividing the relative displacement between the two end fixtures from the FE simulation with the BT strain sensor gage length *Ls* (which is 2 in or 5.08 cm in this study).

The two BT strain sensors (labeled as H6W4 and H9W2 respectively) were attached to the PVC tube using screws and glue bonding at their ends, as shown in Figure 6-6. The two BT strain sensors were stacked on each other, this "stacking" configuration is intended to minimize the effect of cracking of H6W4 on H9W2 in the BT strain sensor, which was observed in the test of a monolithic design and caused complication in the BT strain sensor response. It was observed that after H6W4 fractured, rotation about its pivot point pushed the acrylic sheet outward and made the H9W2 break before its design value.

Three identical component validation tests were conducted on PVC tubes. The loading rate for the axial load applied to the PVC tube was 1 kips/min (4.45 kN/min). The axial strains recorded in the tests are plotted in Figure 6-7. The trigger strain values of the BT strain sensors measured from the thre*e* component validation tests, FEM simulation based design analysis, and countertop tests are listed in Table 6-1 for comparison purpose. It is seen that the measured data of the two strain gages are very close to each other, suggesting that there is very little eccentricity effect and bending moment in the PVC tube. It is also found that the trigger strain levels from all three tests are smaller than the countertop test results. Considering the different end fixture configurations for the BT strain sensors in the PVC tube test and countertop test (see Chapter 3), this discrepancy may be attributed to the fact that after H6W4 fractured, rotation about its pivot point pushed the acrylic part outward. Photos of the fractured BT strain sensors after triggering are shown in Figure 6-8. It is seen that their failure mode is identical to that observed in the countertop tests reported in Chapter 3.

6.4. System validation test on prototype truss

This section presents an experimental study focused on the implementation and validation of the WSCA system through hybrid testing of the aforementioned truss structure under monotonic loading. The experimental findings provide valuable test data of the WSCA system performance, which can be used for identifying challenging issues associated with the full scale implementation of WSCA system. For the convenience of specimen fabrication and safety in trial test, a planar truss made of PVC tubes was used in the experimental study described below. The configuration and dimension of the planar truss and external loads are shown in

Figure 6-9. The left-side top chord (highlighted in red dash line in the figure) of the truss was designated as the experiment element which was to be physically tested during the hybrid simulation test. The ExpBeamColumn2d experimental element in the OpenFresco was used to represent this physical member (i.e., the PVC tube to be physically tested). The PVC tube member has an outer diameter of 4.5 inches (11.43 cm) and an inner diameter of 4 inches (10.16 cm). The length of the PVC tube is 44 inches (1.12 m). The modulus of elasticity of the PVC material was measured to be 160 ksi (1.1 GPa). The support, joints, and external force were all modeled numerically in the OpenSees software program.

The experiment setup is shown in Figure 6-10. The test setup includes the following components: 2 strain gages (Vishay model #: EA-06-250AE-350), BT strain sensor with RFID tag antenna, UHF RFID reader (Skyetek model #: SkyeModule M9), Autodesk Revit Structure, and a custom developed middleware. The MTS hybrid simulation test setup described in Section 6.2 was used for this experimental study. The Skyetek RFID reader is placed at 30 inch (76.2 cm) away from the PVC tube. The inset of Figure 6-10 shows close-up view of the RFID tags and BT strain sensors installed on the test specimen. A single-actuator setup was adopted in this hybrid simulation test to control the degree of freedom in the axial direction of the truss member because the original member in the OpenSees model is a truss bar. Displacement control was used in the hybrid test and the control point, which is the middle-span joint at the lower chord level of the truss, was pushed downward gradually from its original position. The total duration of the hybrid testing lasted about 10 minutes, which depends on the value of the ramping time set for the

hydraulic system and controller. A shorter ramping time leads to faster loading rate. During the test, a displacement increment of 0.01-inch (0.254 mm) was imposed at each step to the test member. For all other elements in the numerical model, their cross-sectional area is assumed to be 3.34 in^2 (21.5 cm^2). A video camera was placed in order to record the failure process of the physically tested member during the experiment.

Two identical hybrid simulation tests were conducted for this experimental study on full-scale implementation and validation test of the WSCA system. Figures 6-11 to 6-16 show the test results from these two hybrid simulation tests. Figure 6-11-(a) shows the measured strain data as well as the trigger strains of the two BT strain sensors (labeled H6W4 and H9W2 respectively) during the first hybrid simulation test (HS Test #1). For independent verification purpose, the strain of the PVC tube member derived from the displacement data measured with the built-in LVDT transducer in the MTS actuator (calculated by dividing the measured displacement with the PVC tube length (44 in or 111.76 cm)) is also included in the figure. It's seen that all of these strain data agree very well with one another. This suggests that the bending moment in the PVC tube due to eccentricity is very small, and thus the section where the BT strain sensor is bonded on the PVC tube is subject to uniform axial deformation. The square marks in Figure 6-11 identify the trigger point for the two BT strain sensors. As shown in Figure 6-10, two BT strain sensors were stacked on each other after installation on the PVC tube. The BT strain sensor H6W4 which has a lower trigger strain level was triggered at 6,486 με, (corresponding to the average of the two strain gage readings at trigger).

Figures 6-12 to 6-13 show the hybrid simulation test setup and screen shots of BIM user interface at the trigger of the BT strain sensors respectively, during the first hybrid simulation test HS Test #1. In the BIM user interface where the Revit structure model is shown, two colors were used to highlight the trigger strain level - blue or red. When the member concerned is marked with a blue color bar, the lower level BT strain sensors H6W4 is known to be triggered. If it's marked with a red color bar, the higher level BT strain sensor H9W2 has also been triggered. Figure 6-12 (b) shows the properties of the selected member in the hybrid simulation test. For example, a unique RFID tag info is shown there which can be used to rapidly identify the member and BT strain sensor. It also includes a "DataTag" which stores the strain level and time when the BT strain sensor is triggered. These properties will be updated automatically during the test. It is worth noting that other customized properties can be included easily depending on the interest of the user.

Similarly, the results from hybrid simulation test #2 are shown in Figures 6-14 to 6-16. In this test, the strain data from the two strain gages appear to be slightly different especially when the strain increased to 5,000 με. This may be caused by the initial misalignment of the test specimen and introduced bending moment to the specimen during the test. However, the average value can be used to cancel out the bending moment effect on the axial strain. The trigger strain for the two BT strain sensors in the two hybrid simulation tests are listed in Table 6-2.

6.5. Summary and conclusions

This chapter presents an experimental test that demonstrates the implementation of the wireless structural condition assessment (WSCA) system. Through the component validation test on truss member made of PVC tube, the configuration and installation approach for the two BT strain sensors were determined: the sensors were attached to the PVC tube by stacking on top of each other and using screws and glue bonding at their ends. This "stacking" configuration is intended to minimize the effect of cracking of H6W4 on H9W2 in the BT strain sensor. It is found that the BT strain sensor's failure mode is identical to that observed in the countertop tests reported in Chapter 3.

A hybrid simulation test of a truss structure was conducted to validate the BT strain sensors installed on a nearly-full-scaled tubular structural member and the BIM-based WSCA system. The various aspects of the BIM-based WSCA system including the integration of the RFID based BT strain sensors and BIM-based computing environment have been evaluated in a real structure setting. For example, its capability of quickly locating and visualizing the threshold strain exceedence in the selected members is demonstrated. In the BIM user interface where the Revit structure model is shown, the two triggering strain levels were highlighted in two colors (blue or red). The automatic updating of the condition states of selected members has also been demonstrated in the hybrid simulation test.

Table 6- 1. Measured and design values of the trigger strain level for the two BT strain sensors on the PVC tube subjected to axial load

	BT strain sensor	
	H6W4	H9W2
Test #1	0.62%	1.02%
Test #2	0.66%	1.05%
Test #3	0.64%	1.03%
Average of test values	0.64%	1.03%
Design value	0.55%	1.18%
Countertop Test	0.68%	1.32%

Table 6- 2. Measured and design values of the trigger strain level for the two BT strain sensors on the PVC tube in hybrid simulation test (HS = Hybrid Simulation)

	BT strain sensor	
	H6W4	H9W2
HS Test #1	0.65%	1.10%
HS Test #2	0.61%	1.02%
Average of HS test values	0.63%	1.06%
Design value	0.55%	1.18%
Countertop Test	0.68%	1.32%

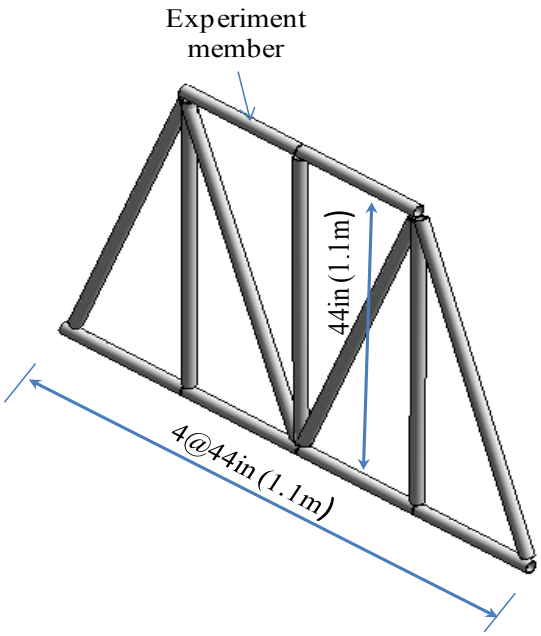

Figure 6- 1. 3D model of the prototype truss structure for hybrid simulation test

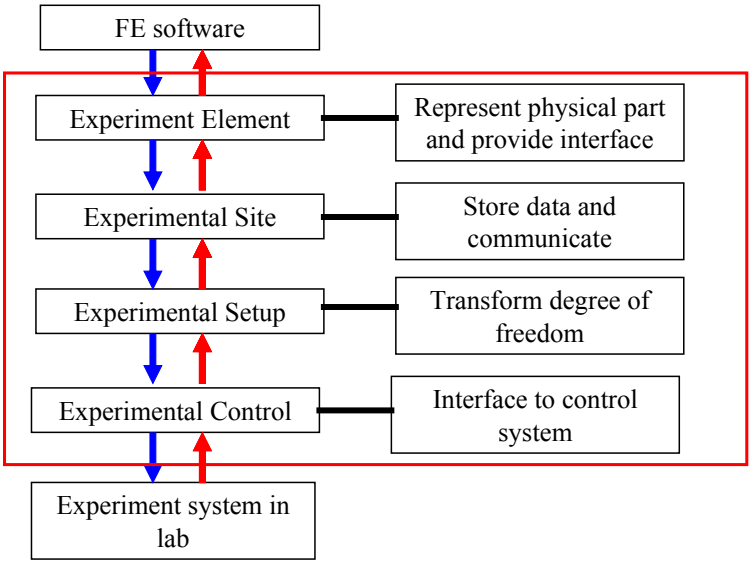

Figure 6- 2. Schematics of hybrid testing software framework (Schellenberg *et al* 2006a)

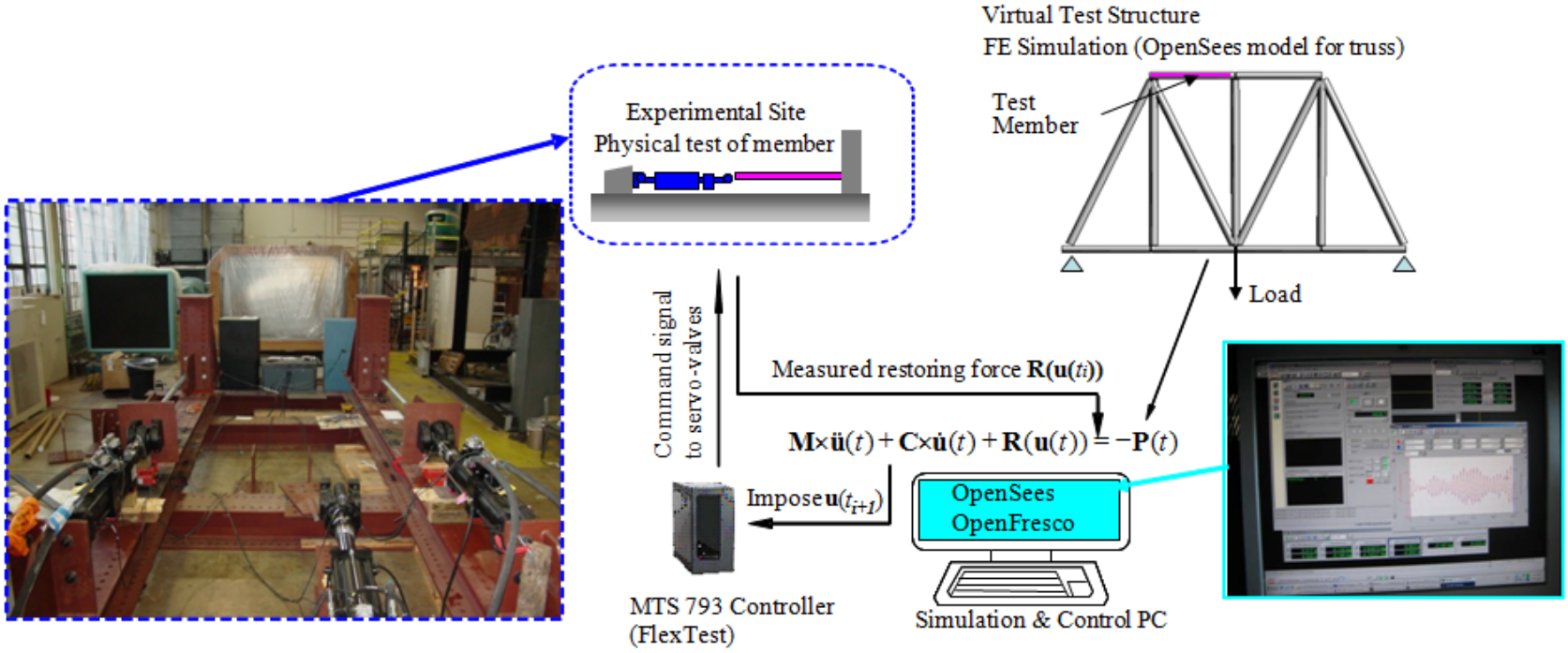

Figure 6- 3. Schematics of a hybrid testing facility for collapse simulation under wind loading

Figure 6- 4. Schematic of test setup for component validation test on PVC tube
(legend: (1) data acquisition system user interface for strain gage measurement; (2) BIM user interface (Revit Structure); (3) RFID reader; (4) PVC tube with BT strain sensors)

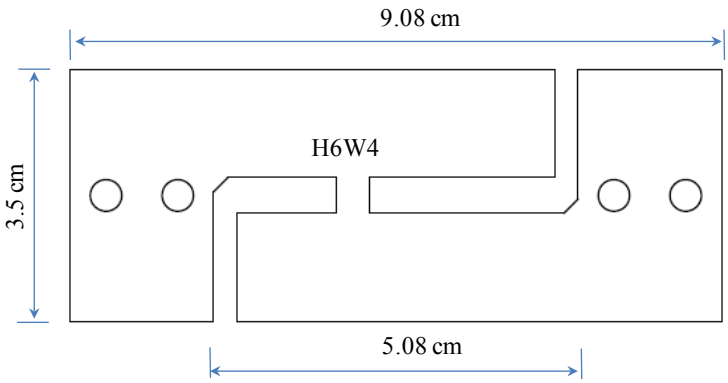

Figure 6- 5. Dimensions of BT strain sensor (H6W4 as an example)

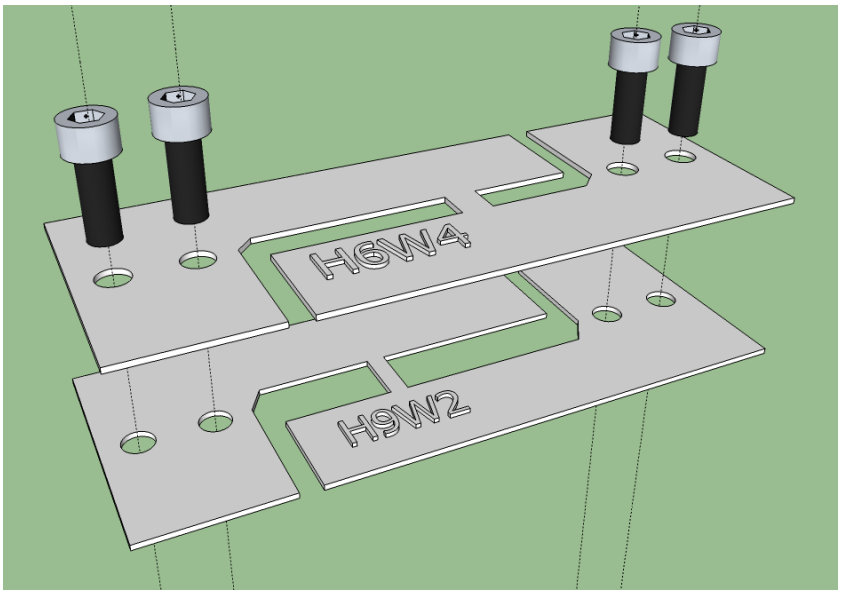

(a) Exploded view of BT strain sensor

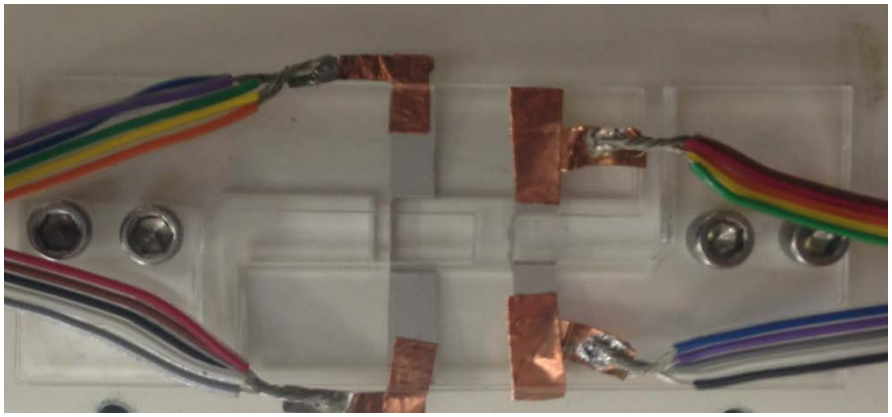

(b) Close-up view of the BT strain sensor on the tube

Figure 6- 6. Schematic of BT strain sensor

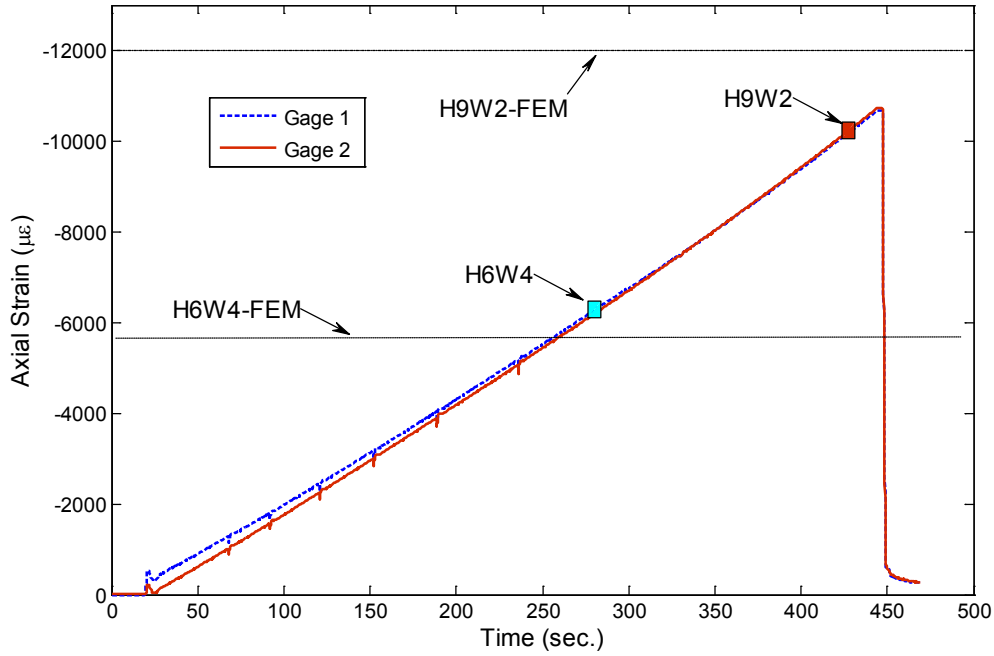

(a) Strain test data from Test #1

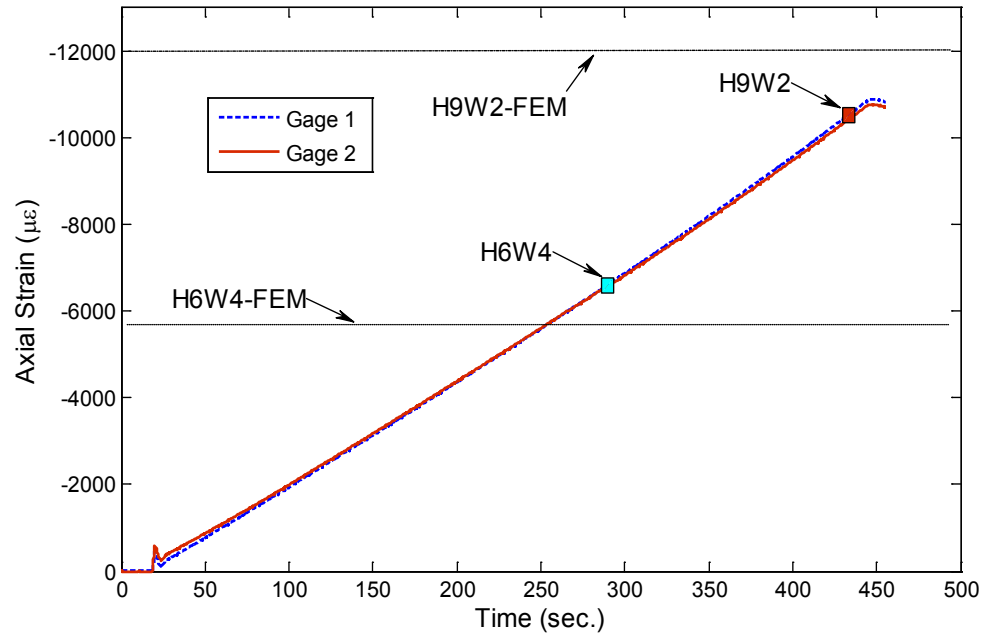

(b) Strain test data from Test #2

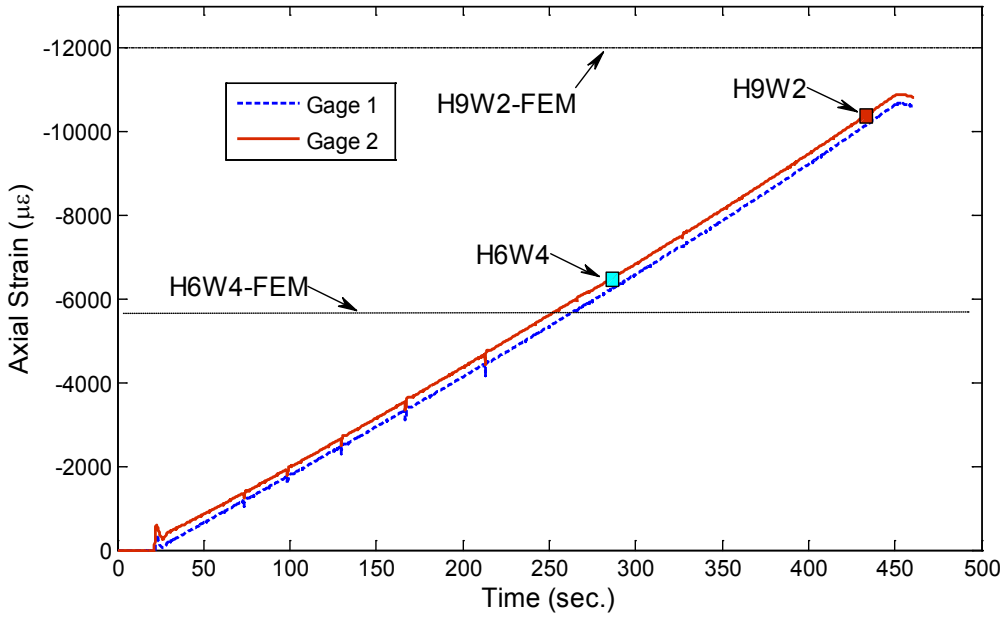

(c) Strain test data from Test #3

Figure 6- 7. Comparison of measured strain of the PVC tube and triggering time point of the BT strain sensors

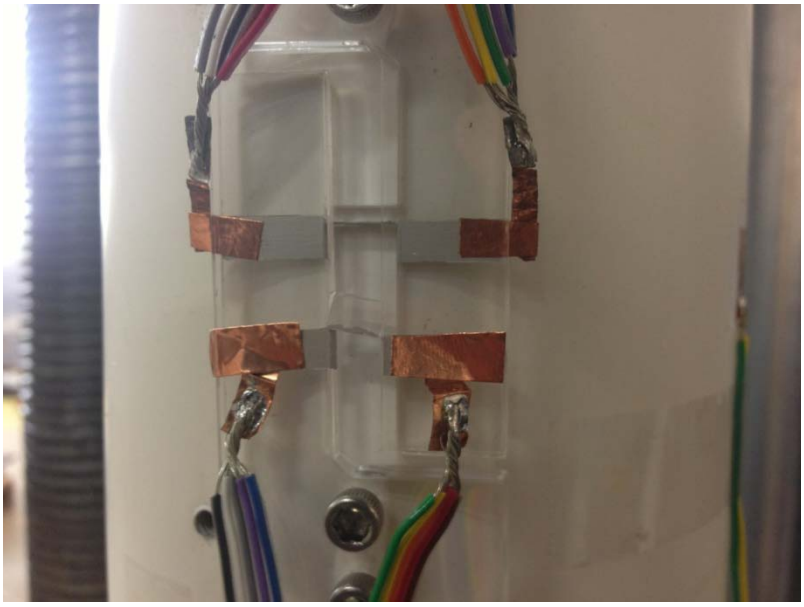

Figure 6- 8. Close-up view of the cracks in the BT strain sensors after triggering

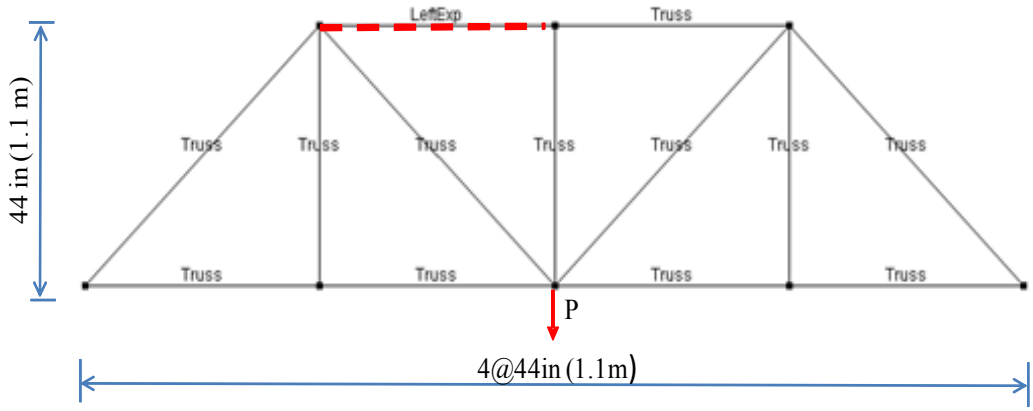

Figure 6- 9. Prototype truss model for hybrid simulation test

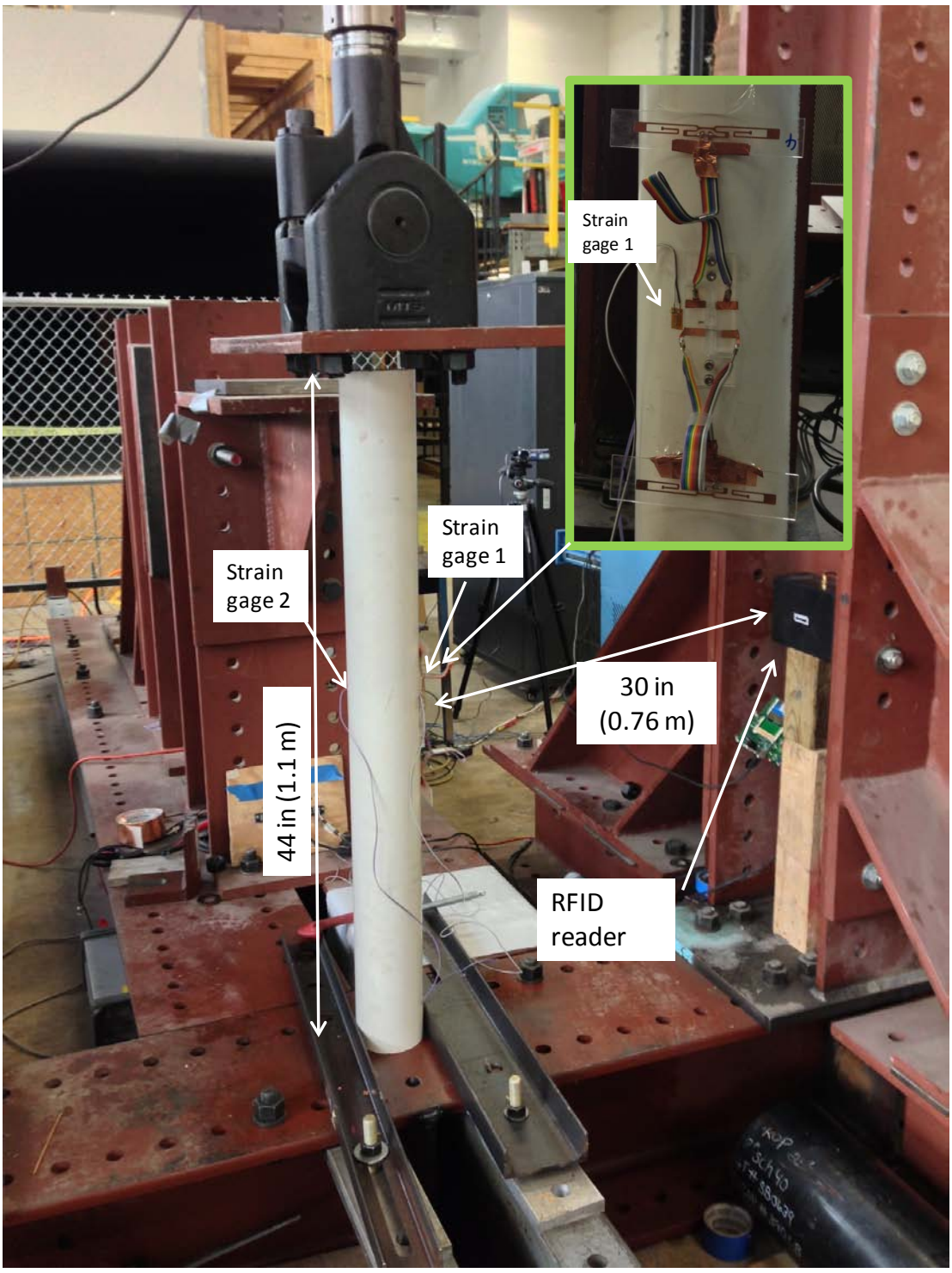

Figure 6- 10. Hybrid simulation test setup for system validation of WSCA on truss structure

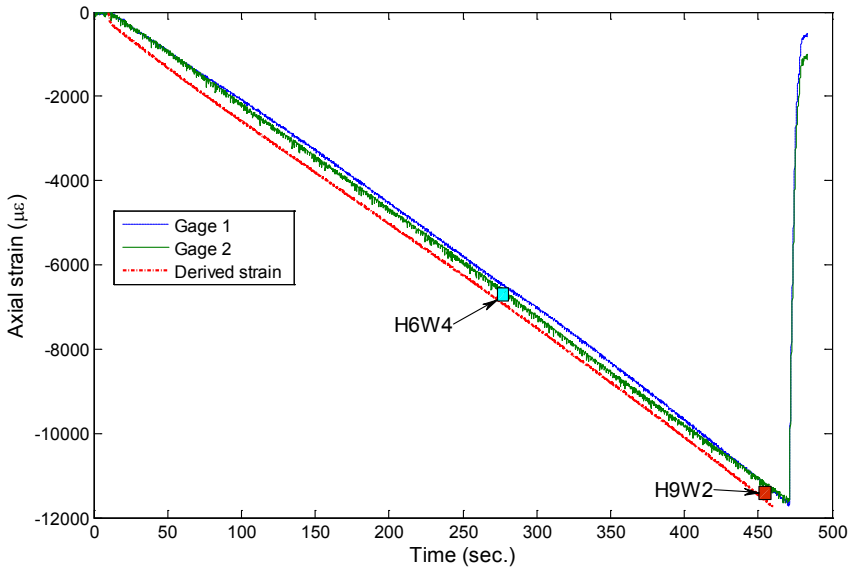

(a)

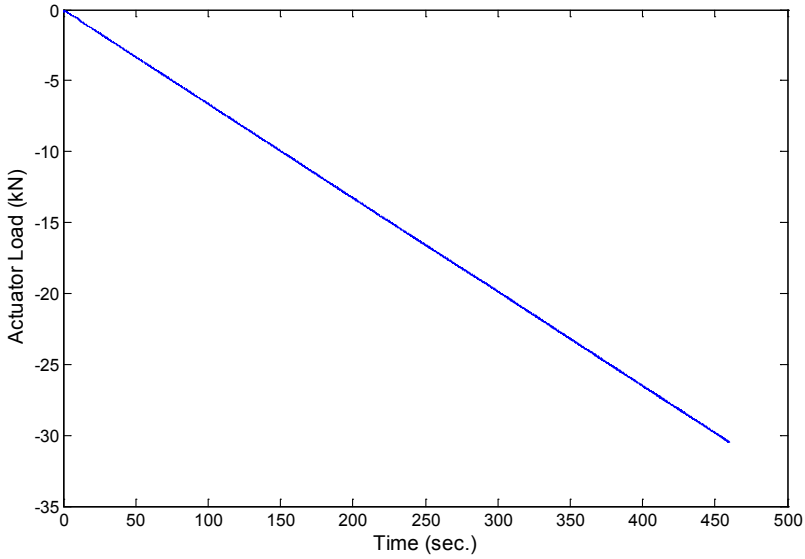

(b)

Figure 6- 11. Test results of the first hybrid simulation test on truss structure (HS Test # 1, Strain): (a) strain test data (from PVC tube); (b) load data (on PVC tube)

(a)

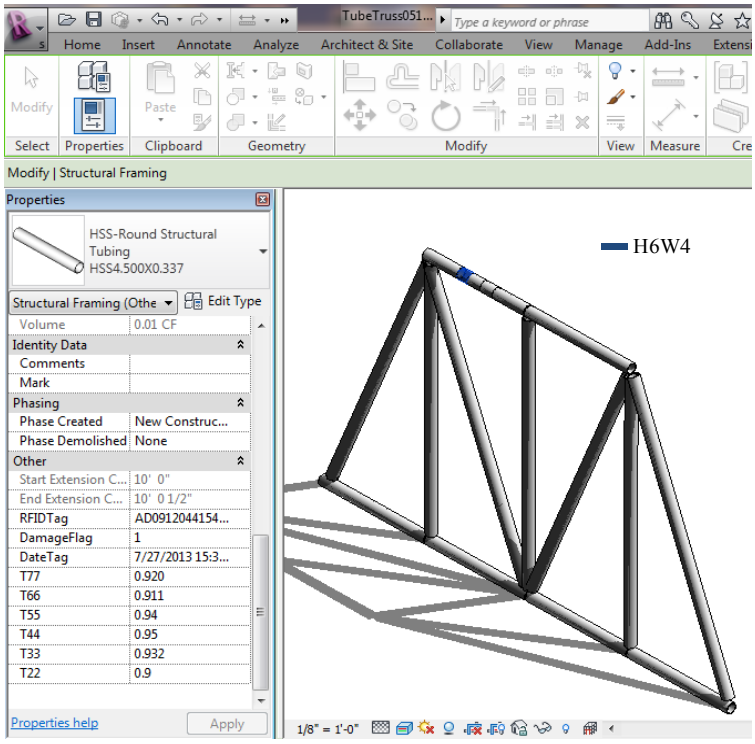

(b)

Figure 6- 12. Test results of the first hybrid simulation test on truss structure (HS Test # 1, H6W4): (a) picture of test setup at triggering of H6W4; (b) screen shot of BIM user interface

(a)

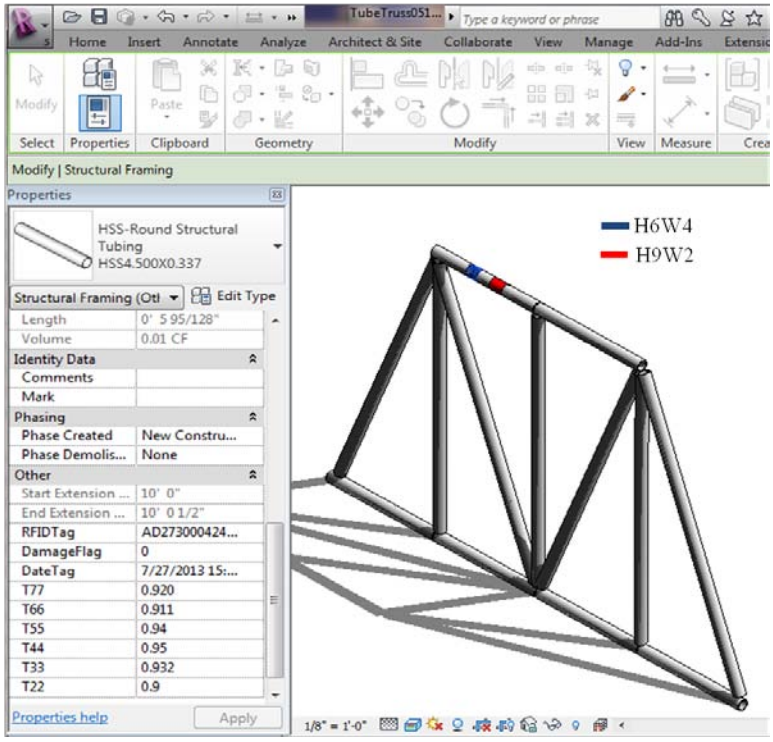

(b)

Figure 6- 13. Test results of the first hybrid simulation test on truss structure (HS Test # 1, H9W2): (a) picture of test setup at triggering of H9W2; (b) screen shot of BIM user interface

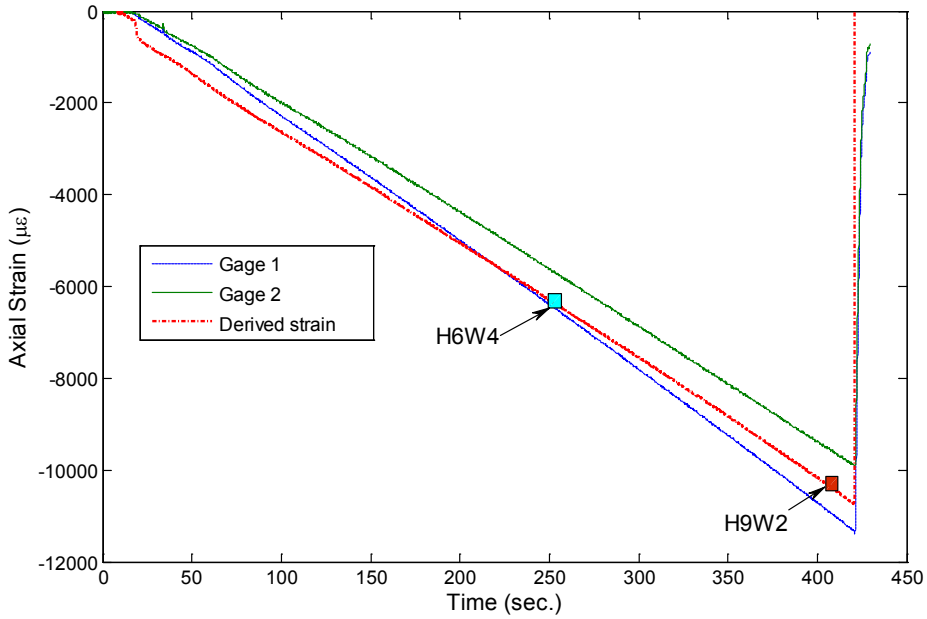

(a)

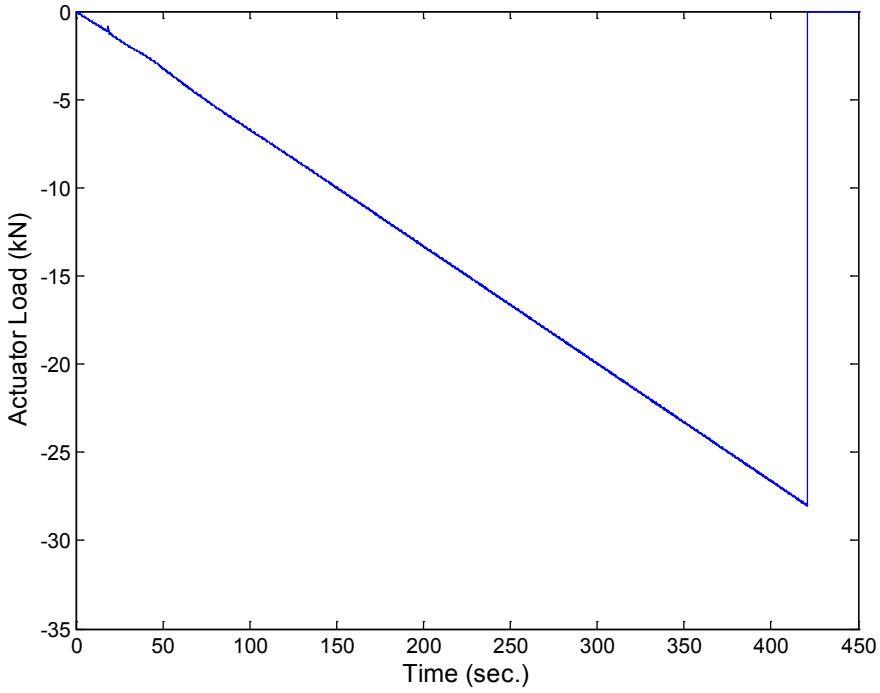

(b)

Figure 6- 14. Test results of the first hybrid simulation test on truss structure (HS Test # 2, Strain): (a) strain test data (from PVC tube); (b) load data (on PVC tube)

(a)

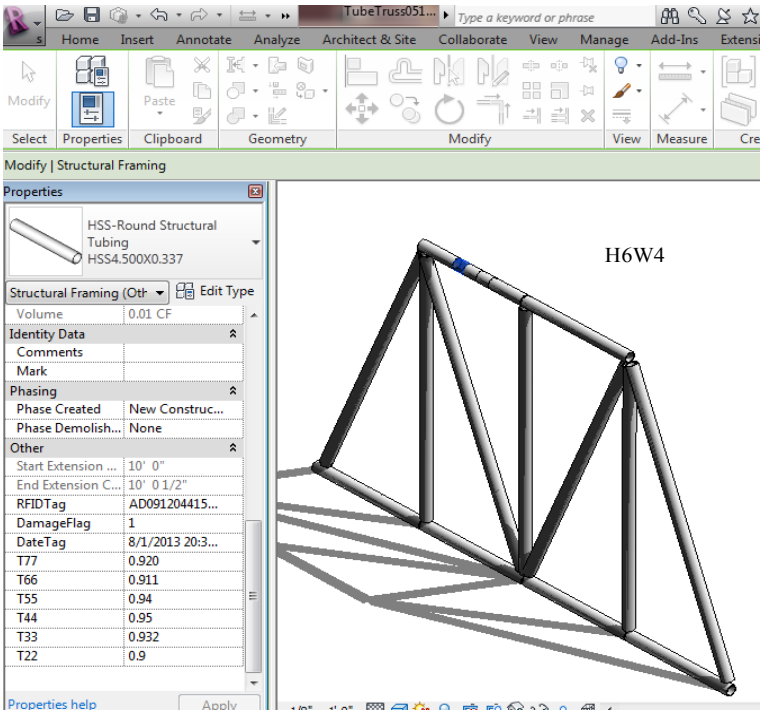

(b)

Figure 6- 15. Test results of the first hybrid simulation test on truss structure (HS Test # 2, H6W4): (a) picture of test setup at triggering of H6W4; (b) screen shot of BIM user interface

(a)

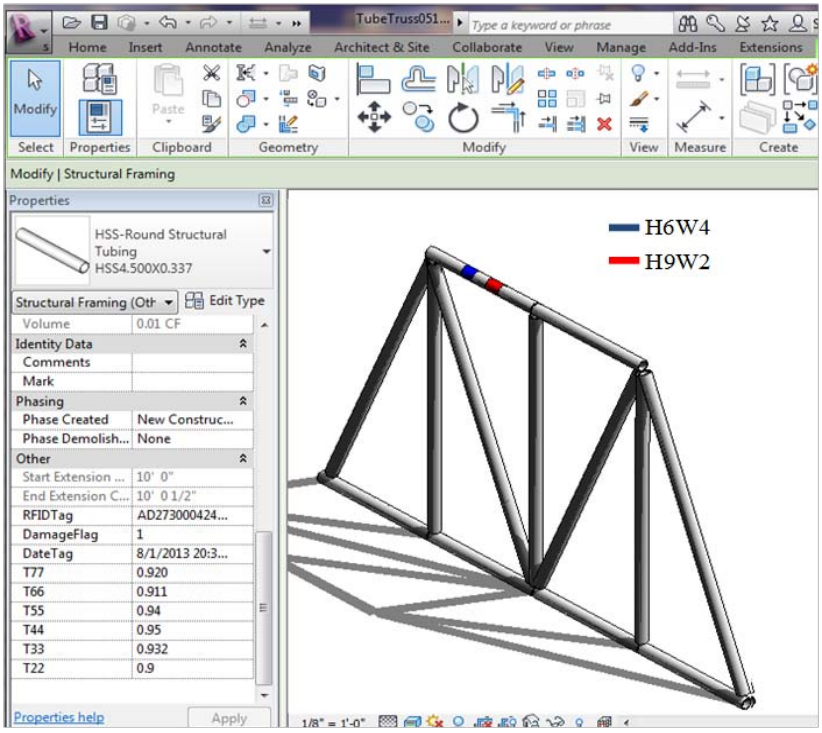

(b)

Figure 6- 16. Test results of the first hybrid simulation test on truss structure (HS Test # 2, H9W2): (a) picture of test setup at triggering of H9W2; (b) screen shot of BIM user interface

Chapter 7: WSCA Case Study II: Eccentrically Braced Frame (EBF) with Shear Link

7.1. Introduction

Eccentrically braced frames (EBFs) are a lateral load-resisting system for steel buildings that can be considered a hybrid between conventional moment-resisting frames (MRFs) and concentrically braced frames (CBFs). EBFs were proposed in an attempt to combine the individual advantages of MRFs and CBFs, while minimizing their respective disadvantages (Popov and Engelhardt 1988). The most attractive feature of EBFs for seismic-resistant design is their high stiffness combined with excellent ductility and energy-dissipation capacity. The excellent ductility of EBFs can be attributed to inelastic shear deformation in the links, which are designed and detailed to sustain large inelastic deformations without loss of strength. The shear links are easy to replace and they won't fail before experiencing large deformations (Mansour *et al*. 2008). The yielding of the links (yield mostly in shear, therefore called shear link) in EBFs serves to limit the maximum force transferred to the brace. Under severe earthquake loading, shear links in EBFs function as structural fuses, experiencing plastic deformation while other components of the EBF remain essentially elastic (Popov *et al*. 1988). Rotation capacity is greatest for short links that yield primarily in shear which are typically used in the EBF design (Richards and Uang 2006). The damage to an eccentrically braced frame due to a major earthquake is designed to be confined to a highly ductile link. The link acts as a safety valve for

the structure (Ghobarah and Ramadan 1990). Therefore, monitoring the peak strain levels in shear links during earthquakes and thus its remaining ductility capacity for aftershocks is essential to the safety and resilience of EBF structures.

In this chapter, a three-story EBF building was chosen as the prototype structure to demonstrate the resilient structure concept with the use of the proposed BIM-based WSCA system. First, a numerical simulation analysis was conducted on the prototype EBF subjected to an ensemble of 20 earthquake records in order to collect the information for the design of BT strain sensors. An experimental test of the WSCA mounted on a 1/3-scaled shear link was performed to demonstrate the use of and evaluate the performance of the BIM-based WSCA system.

7.2. BT strain sensor design

7.2.1. Prototype EBF modeling

The three-story prototype EBF buildings was designed by Richards and Uang (2006) for location in Los Angles based on the moment frame protocol work by Gupta and Krawinkler (1999), following the local code requirements for Los Angles. All prevailing code requirements for gravity, wind, and seismic design were considered. The building was designed as a standard office building situated on stiff soil (Soil type S2 as per UBC 1994). It was redesigned according to the IBC (ICC 2000) and AISC Seismic Provision (AISC 2002) using eccentrically braced frames (Richards and Uang 2006).

A two-dimensional model of the case study building was developed in this study using the computer program OpenSees (McKenna 1997). The three-story EBF with

the shear link model was modeled as a two-dimensional planar structure in the OpenSees software as shown in Figure 7-1. The member sections are listed in Table 7-1. Accurate modeling of the EBF and specifically the shear links are critical to the seismic performance evaluation since the inelastic deformation of the EBF is confined to these shear yielding links while other members are supposedly to remain linear elastic during design level earthquakes. A special element developed by Moghaddasi-B. (2011) in the OpenSees that simulates the cyclic loading behavior of the shear links was used for this study. A detailed description of this shear link element is given in the next section.

7.2.2. Shear link model in OpenSees

Shear links were modeled using a technique proposed by Ramadan and Ghobarah (1995). Ramadan and Ghobarah's approach is based on the theory developed by Ricles and Popov (1987) and can be incorporated into general finite element (FE) analysis programs. In this study, shear link is modeled using the approach adopted by (Moghaddasi-B. 2011), namely, the following three elements are used collectively in the model: a beam element in the middle which accounts for elastic axial, bending and shear deformations and yielding in bending, and two zero length elements at two ends of shear link which account for yielding in shear.

The middle beam used in the link model is an OpenSees element called "beam with hinges". This element is comprised of three parts: two hinges at the ends, and a linear-elastic region in the middle (see schematics in Figure 7-2). The hinges at the ends in the middle beam is modeled using the rigid-plastic hinges which are built in

to the beam element (Mazzoni *et al*. 2009). The hinges were defined to yield at the plastic moment capacity calculated using the expected yield stress of 345 MPa (50 ksi). The post-yield flexural stiffness of the link was equal to 5% of the elastic flexural stiffness. The plastic moment capacity of a link, M_p, is determined from the following equations (ANSI/AISC 341-10):

$$M_p = Z\sigma_y \tag{7-1}$$

where σ_y is the yield strength of the shear link material and Z is the plastic modulus of the link cross section. The moment developed in the shear links are supposed to be lower than their plastic moment capacity since the links are shear critical.

The shear stiffness and yielding in the link are modeled by two zero length elements (termed shear hinge springs in Figure 7-2) at two ends of the shear link. In Figure 7-3 link shear V is plotted against the elongation δ of the zero-length element in the direction perpendicular to the shear link longitudinal axis in the undeformed configuration. This V- δ curve is calibrated based on the experimental test results from A992 steel short links (Arce 2002). The shear link behavior observed in experimental test, can be divided into three distinct phases: the elastic behavior up to the shear force of $1.1Vp$ and plastic and degradation phase before ultimate failure of the link by fracture in web section (Okazaki *et al*. 2006). The plastic shear capacity of a link, V_p, is determined using the equation below (from ANSI/AISC 341-10 (AISC 2010)):

$$V_p = 0.6\sigma_y \cdot A_{web} \tag{7-2}$$

where σ_y is the yield strength of the shear link material and A_{web} is the cross sectional area of the web in the link.

Four parallel springs with isotropic bilinear behavior were used to model the shear hinges at both ends of the link element as shown in Figure 7-2. Elastic-perfectly-plastic (ElasticPP) material in OpenSees was used to model the hysteresis behavior of four springs connected in parallel, with zero-length elements positioned at the ends of the link element to simulate the piecewise-linear shear behavior of the shear link shown in Figure 7-3.

In this study, two types of link rotation angle, γ_a and γ_p, are defined and recorded, as shown in Figure 7-4. The first type of link rotation angle, denoted as γ_a, is defined using Eqn. 7-3a. γ_a is computed as the relative vertical displacement between the two ends of the link divided by the link length. The other definition for link rotation angle is adopted from ANSI/AISC 341-10 seismic code (AISC 2010), as illustrated in Figure 7-4. In the figure, the link rotation angle can be related to the plastic story drift angle θ_p. L is the bay width of the EBF. The link rotation angle, noted as γ_p, is calculated with the equation below:

$$\gamma_a = \frac{\Delta}{e} \tag{7-3a}$$

$$\gamma_p = \frac{L}{e}\theta_p \tag{7-3b}$$

7.2.3. Elements, materials and loads

Nonlinear beam-column elements with inelastic fiber sections were used to model the beams in the braced bays and all columns. The beams in the middle two bays are modeled using truss elements in the OpenSees because connections in these unbraced bays were considered simple in the original design (Richards and Uang 2006). The bracing members which are intended to carry the load only through axial action, are also modeled with truss elements. The braces in the first story of the EBF were assumed to be fixed at their lower ends.

Material behavior for all elements, including braces, beams and columns was modeled using the Giuffre-Menegotto-Pinto model (Menegotto and Pinto 1973) with isotropic strain hardening of 2%, Young's modulus of 200 GPa, and yield strength of 345 MPa (50 ksi) (i.e., Steel02 material in OpenSees).

A gravity load combination of 1.2DL+0.5LL based on design code was applied to the structure during seismic loading. The dead load DL is calculated to be 80 psf (3.83 kPa) for the roof and 85 psf (4.07 kPa) for other floors. The live load LL for each floor is assumed to be 20 psf (0.96 kPa) for the roof, but 50 psf (2.4 kPa) for other floors. Floor masses (only dead load is considered for seismic mass) were lumped into the beam end nodes at each floor level and lean-on column joints based on tributary area. A lean-on column along the height of the structure and pinned at its base, consisting of 3 elastic rigid link bar elements was used in the model to simulate the gravity columns which can account for the P-Delta effect. The lean-on column was connected to the center interior nodes of each floor of the EBF frame by

assigning multi-point constraint to the corresponding nodes to transfer the seismically induced inertia force.

Damping effect in the time history analysis was considered through Rayleigh damping. As a typical value for steel buildings, a 2% damping ratio for the first and third modal frequencies of the EBF was used for the OpenSees model. The stiffness proportional damping was applied only to the frame elements, since for accurate analysis no stiffness damping should be considered for the lean-on column and highly rigid truss elements that link the frame and lean-on column (Zareian and Medina 2010).

7.2.4. Eigen value analysis

The Eigen value analysis was performed using the model developed in OpenSees. The first three vibration periods of the 3-story EBF were 0.61, 0.29 and 0.20 seconds respectively. The first three mode shapes are shown in Figure 7-5.

If it is assumed that the first mode dominates the seismic response of the structure, the inverted triangular vertical load pattern seems to be appropriate to distribute the base shear along the height of the building in pushover analysis according to the first mode shape of the building.

7.2.5. Nonlinear static analysis

Nonlinear static analysis provides a insight into the performance of the structure. A pushover analysis of the 3-story EBF was performed to identify the nonlinear static

response of the EBF. The inverted triangular lateral load pattern was used to distribute the base shear along the height of the building in pushover analysis.

The lateral loads were applied as lumped forces at the left most exterior nodes at each floor level. The loads were increased monotonically until the horizontal displacement at the middle node of the roof reached the drift ratio of 3%.

The roof drift ratio (roof displacement divided by the height of the building) vs. the normalized base shear response (also known as pushover curve) from the nonlinear static analysis, is shown in Figure 7-6. The pushover curve also shows the sequence of the plastic deformation development in the shear links. In Figure 7-6, *L1, L2, L3* refers to shear links at the 1^{st}, 2^{nd}, and 3^{rd} floor levels begin plastic deformation respectively. Definition for $\delta 1, \delta 2, \delta 3$ can be found in Figure 7-3.

It is seen that the slope of the post yield branch of the pushover curve changes as the shear links enter different phases of their inelastic deformation. During the pushover analysis, the base shear increases linear proportionally until the roof drift ratio reached about 0.5% when the corresponding base shear ratio was about 0.11.

7.2.6. Nonlinear time history analysis

The performance of a structural system under strong earthquakes can be evaluated by comparing the nonlinear time history analysis results of the key engineering demand parameters (EDPs) with code specified values and what is generally accepted in practice. For the purpose of obtaining the anticipated strain levels of the shear links in the prototype EBF building at design basis earthquakes (DBE) and maximum credible

earthquakes (MCE), nonlinear time history analysis of the 3-story EBF was performed under a suite of 20 strong earthquake records, which were originally developed by Somerville *et al.* (1997) for the Los Angeles, California region with a probability of exceedance of 10% in 50 years. The MCE records were obtained by scaling up the DBE records by 1.5 times. These scaled earthquake records correspond to the design basis earthquake in the downtown Los Angeles area. The Newark average-acceleration (γ=1/2, β=1/4) time-step integration method with Newton initial stiffness interaction was used to solve the dynamic differential equations. The time interval for all time history analyses was set to be 0.001 seconds.

The results of important EDPs are presented in Figures 7-7 to 7-12. Since it is not possible to present all detailed results of all time history analyses, LA01 is chosen as a representative case for the nonlinear time history analysis and some of its detailed time history results are presented here. For simplicity, shear link will be denoted as L*x*L and L*x*R, where *x* indicated the floor where the shear link is located; *L* indicated the left-hand side link while *R* indicates right-hand side link on each floor, as shown in Figure 7-1.

Tables 7-2 to 7-5 list the maximum link rotation angle of shear links in the EBFs subjected to either DBE or MCE earthquake records. The mean value refers to the ensemble average of the results over the 20 earthquake records. The mean value of the link rotation angles derived for DBE and MCE records will be used to guide the design of the BT strain sensors in the next section.

7.3. FE analysis of shear link

7.3.1. FE model description

A FE analysis of the shear link was first conducted to determine the principal strain distribution on the web plate in order to guide the design of the BT strain sensors. To lower the demand on the testing equipment, a reduced-scale shear link specimen that is 1/3 of its original size W16x77 is adopted. W16x77 is the section size of the two shear links located at the EBF's first floor. Although the model length (8 inches) is slightly longer than that (6 inches) of 1/3-scale, it should have negligible effect on the findings since the loading of the shear link is displacement-control loaded to a link rotation angle of 0.08 rad. The extra 2-inch in length is also favorable to the experimental test because it gives more space to sensor installation. Therefore, a reduced-scale FE model is adopted to provide information for test planning. The FE model of the 1/3-scaled shear link created in ANSYS v.13 is shown in Figure 7-13. This FE model was developed in three dimensions to provide the details of stiffeners and flange. 3-d solid elements (ANSYS 8-node element SOLID45 with 3 degrees of freedom (DOFs) per node) was used to model all components in the shear link. The right-hand side end of the shear link was restrained from movement by applying translational constraints to all DOFs of the nodes over the entire end section. Therefore, the link model has a fixed end on its right side. Material behavior for steel was modeled using the Bilinear Isotropic Hardening (BISO) with strain hardening of 2%, Young's Modulus of 200 GPa, and yield strength of 345 MPa (50 ksi).

The BT strain sensors are installed on the web using four attachment screws, as shown in Figure 7-18. For the acrylic BT strain sensor, its Young's modulus is 2.76 GPa and tensile strength is 69 MPa. In the FE model, the attachment screws were simulated by coupling the nodes on the strain sensor with corresponding nodes on the web for all DOFs. The dimensions of the acrylic BT strain sensors are the same as those shown in Figure 6-5. The gage length of the BT strain sensor is 60.8 mm.

The shear link is loaded by applying a concentrated load at the point on the top flange, as shown in Figure 7-13. To rotate the shear link by a link rotation angle of 0.08 radians, the downward displacement at the load application point is 0.64 inch (1.63 cm).

7.3.2. Orientation of BT strain sensor

As mentioned earlier, a brittle material will fail when the maximum principal stress exceeds some value, independent of other stress components present. Therefore, the failure criteria for the brittle bar adopted in this study is that first principal strain reaches the fracture strain in a simple tension test. For example, the acrylic brittle bar will fail by fracturing whenever the maximum first principal strain around the corner surpasses 3%. The first principal strain is defined as the first principal stress divided by the modulus of elasticity of the material, that is, $\varepsilon_1 = \sigma_1/E$. When the relative displacement between the two parts of the BT strain sensor reaches the critical value, brittle bar in the strain sensor breaks and corresponding RFID tag is restored to normal operation to signify the breakage and threshold strain exceedance. The BT strain sensors would be considered triggered whenever the first

principal strain first exceeds 3%. Triggering of the BT strain sensor can thus be related to the link rotation angle.

The BT strain sensors were installed onto the web using four attachment screws (two on each end), as shown in Figure 7-18. An initial concern was whether the rotation restraint by the group of two screws on each end would cause additional strain in the brittle bar because of the link's curved deflected shape. It is desirable to check the effect of sensor's orientation angle would have on the deformation of the brittle bar in the BT strain sensor. For example, if the sensor axis is oriented vertically, the two groups of end screws should rotate by the same amount because they are on the same cross-section of the shear link and there would be no additional deformation induced. Figure 7-14 and 7-15 show the vector plot of first principal strain on the web. It can be seen that the first principal strain on the web are about 45° to the longitudinal axis of the shear link. Therefore, the relative displacement between the two parts of the BT strain sensor reaches larger value if the sensor orientated at 45° to the longitudinal axis of the shear link.

To investigate an optimal orientation angle for the installation of the BT strain sensor on the web plate, four cases were considered in this FEM study. The FE models in these four cases are shown in Figure 7-16. Two BT strain sensors each with different brittle bars (H6W4 or H9W2) are installed on each side of the link's web plate. The angles between the axis of the BT strain sensor and the longitudinal axis of the shear link in these four cases are: 45°, 0°, 90° and 35° respectively. The

BT strain sensors are placed near the neutral axis in the vertical direction (Y-direction) and its right most edge is 1 inch (2.54 cm) away from the fixed end.

To visualize the effect of different orientation angles of the BT strain sensors on their deformation, the initial and deformed locations of the four attachment screws in the sensors were presented in Figure 7-17. The initial locations of the four attachment screws were marked as open circles and deformed locations (corresponding to link rotation angle of 0.08 rad.) were marked as circles with dashed line. It is seen that for all three cases, the four attachment screws were still in a straight line after deformation. This suggests that there is negligible uneven rotation at the two end screw groups. The changes in the distance between the two inner attachment screws, ΔL, and the ratio of $\Delta L/L$ for each case are calculated and given in Table 7-6. The distance between two inner attachment screws after deformation is denoted as *L'* in the table.

The relationship between the link rotation angle and maximum value of the first principal strain in the BT strain sensor are plotted in Figure 7-19. Using the 3% principal strain failure criteria, the link rotation angle could be related to the breakage and triggering of the BT strain sensor. Figure 7-19(a) shows that for Case 1 (45° orientation angle), the first principal strain of strain sensor H6W4 and H9W2 reaches 3% when the link rotation angles are 0.037 and 0.078 radians respectively. The maximum value of first principal strain in the BT strain sensor in Cases 2 and 3 are below 0.2%, meaning that the BT strain sensor will not break even if the link rotation angle goes beyond 0.08 radians. The contour plots of the first principal strain for four cases are shown in Figure 7-20.

The ensemble average of the maximum link rotation angles in the corresponding shear link (L1L) from the previous nonlinear time history analysis of the EBF building subjected to 20 earthquake ground motion records are also shown in Figure 7-19(a). The ensemble average values of link rotation angles of the shear link are 0.07 and 0.15 for the DBE and MCE levels respectively. Based on the FE analysis results, the BT strain sensors H6W4 and H9W2 could provide two threshold level indication of the link rotation angle, close to Frequent Earthquake (FE) level and DBE levels. This enables the WSCA system to provide multi-level structural condition indications after earthquake events.

It's worth noting that although this study uses a two threshold level BT strain sensor, adjustments could be made to include three threshold levels or more so that indication of exceeding link rotation angles corresponding to earthquakes in between the DBE and MCE levels could be provided. Other adjustments include rotating the BT strain sensors to an orientation angle that reduces the sensitivity of the BT strain sensors to link rotation. For example, the BT strain sensor could be rotated counter-clockwise by 10 degrees so that the angle between the sensor axis and link longitudinal axis is 35 degrees, which is Case 4 presented in Figure 7-19(d). It can be seen that the triggering link rotation angles for the BT strain sensors H6W4 and H9W2 are increased to 0.041 and 0.091 radians respectively.

Contour plots of the first principal strain of the BT strain sensors for all four cases are shown in Figure 7-20. In these figures, the shear link was deformed to a link rotation angle of 0.03 radians. It's seen that in Case 1, the first principal strain in sensor H6W4 reached 0.025. However, the first principal strains in the BT strain sensors for

Cases 2 and Case 3 are both smaller than 0.01. The first principal strain in the sensor for Case 4 is smaller than that in Case 1. This confirms that the BT strain sensor in Case 4 was triggered at a larger value of the link rotation angle compared with that in Case 1.

7.4. Experimental validation test

This section presents an experimental test to validate the WSCA system in a shear link specimen designed based on the prototype EBF building. As mentioned in the previous section, the shear link on the first floor of the EBF building was selected as the prototype link for this study. The prototype link has a section size of W16x77 and a length of 0.91 m (3 ft.). Due to limitation of loading equipment and availability of steel shapes, a 1/3-scaled steel WF section, W6x12, was used for the link test specimen in this experimental study. It is worth noting that the web thickness of W6x12 is 0.23 inches, which is greater than 0.15 inches (=1/3-scale web thickness of W16x77). The steel grade of the shear link specimen was ASTM A-992 steel. The W6x12 link beam was welded to a 1-inch (2.54 cm) thick end plate to anchor it on the reaction frame.

The test setup configuration and test specimen dimensions are schematically shown in Figure 7-21. The test setup for validating the WSCA system on shear link includes the following components: 2 strain gages (Vishay model #: EA-06-250AE-350), two BT strain sensors with UHF RFID tag, UHF RFID reader (Skyetek model #: SkyeModule M9), BIM software (Autodesk Revit Structure), and a custom developed middleware. The RFID reader was placed at a distance of 32 inches (81.28 cm) away

from the shear link. MTS servo-hydraulic testing system (see description in Section 6.2) was used to apply load on the shear link in the experimental test. Displacement control was implemented in the test and the control point, which is 8 inches (20.32 cm) away from the end plate on the upper flange surface, was pushed downward gradually from its initial position.

Figure 7-22 shows a close-up view of the RFID tags and acrylic BT strain sensors installed on the link test specimen. The BT strain sensors on the web plate were inclined by a 45-degree angle to the longitudinal axis of shear link and 1 inch (2.54 cm) away from the end plate. In this test, combined BT strains sensors H9W2 and H6W4 were stacked on top of each other to provide a two threshold strain level indication. When the first threshold strain level is reached, H6W4 would break, and its trigger would highlight the shear link model in the Revit Structure in blue color. Similarly, whenever the second threshold level is exceeded, H9W2 would break, and the shear link model in the Revit Structure would be highlighted in red color.

Unfortunately, the test was halted due to an accident. As shown in Figure 7-24, top flange of the link specimen was fractured due to local bearing failure at a load level of nearly 30 kips (133.4 kN). The test was called off and an alternative test plan was proposed and implemented.

To evaluate the BT strain sensor's performance on steel structure component, compression test was conducted on a stub column (by turning the link specimen 90 deg.). The test setup for this compression test is shown in Figure 7-25. The test setup includes the following components: 2 strain gages (Vishay model #: EA-06-250AE-

350), two BT strain sensors with UHF RFID tag, UHF RFID reader (Skyetek model #: SkyeModule M9), and BIM software (Autodesk Revit Structure). The universal test machine used for this test is a SATEC 400-kips servo-hydraulic test machine (serial #: 400BTE/483280). The stub column specimen was loaded axially till it failed at about 711 kN. Two strain gages were installed on the web plate at the BT strain sensor location, one on each side of the web plate. The strain gage was aligned with the longitudinal axis of the stub column in order to record its axial strain during the test. The Skyetek RFID reader was placed at a distance of 32 inch (81 cm) away from the shear link, as shown in Figure 7-25.

The axial load was applied to the stub column by using displacement control. The loading rate is 0.2 inches (0.508 cm) per minute. The applied load on the stub column during the test is shown in Figure 7-27. Figure 7-28 shows the stress vs. the strain of the stub column (denoted as derived s train) derived from the measured crosshead displacement data (calculated by dividing the measured displacement with the stub column length of 11 inches (28 cm)). In this figures, the trigger time or strains of the two BT strain sensors (labeled H6W4 and H9W2 respectively) is also shown. It is seen that the axial force reached its peak value of 160 kips (711.7 kN) and begun to drop right after the peak. The readings of the two metal foil strain gages placed on the web plate were shown in Figure 7-29. The strain data measured (denoted as measured strain) from the two metal foil strain gages appear to be different. This may be caused by the initial misalignment of the fractured test specimen after the previous shear link test accident and introduced eccentricity and thus bending moment to the stub column specimen during the test. The two strain gages stopped working at 15 and 20 seconds

respectively due to the web local buckling that was observed during the test. The two BT strain sensors were triggered at around 6,000 and 6,600 με (derived strain) respectively. Both BT strain sensors were triggered below design value due to the local buckling on the web plate during the test. This is because local buckling caused out-of-plane bending and thus introduced additional strain to the BT strain sensors.

Figures 7-30 shows a screen shot of the BIM user interface (Revit Structure) after both BT strain sensors were triggered. In the Revit model, two colors (blue or red) were used to identify whether the two pre-set threshold strain levels were surpassed in the stub column. When the member concerned is highlighted with a blue color bar, the lower threshold strain level (for H6W4) is known to be exceeded. If it's also marked with a red color bar, the higher threshold strain level (for H9W2) has also been surpassed. The buckled stub column specimen after the test was shown in Figure 7-31. Both flange and web plates were buckled during the test.

7.5. Summary and conclusions

To validate and demonstrate the use of WSCA system in real steel structures, an experimental study of the BT strain sensors installed on shear links from a three-story prototype EBF building was conducted in this chapter. To guide the design of BT strain sensors for shear link strain condition monitoring, nonlinear time history analysis of EBF building subjected to an ensemble of 20 earthquake records was performed. The earthquake records were scaled according to the design basis earthquake (DBE) and maximum credible earthquakes (MCE) for a location in the Los Angles, California region. It's found from nonlinear time history analysis that the

mean value of maximum shear link rotation angles of the shear links in the EBF building is 0.07 radians under DBE and 0.15 radians under MCE. Based on this information, the design of BT strain sensors were studied using FE analysis of a shear link integrated with BT strain sensor. It's found that by installing the BT strain sensors on the web plate of the shear link in different inclination angles, the WSCA system can be adjusted to monitor different levels of link rotation angle of the shear link and thus offers alert signal for exceeding multiple preset threshold strain levels that can be displayed in the BIM user interface. By installing the BT strain sensor at an inclination angle of 45 degrees, the WSCA system can give the first level exceedence alert at 0.037 radians and second level exceedence alert at 0.078 radians for the shear link specimen considered in this study.

An experimental validation test of the WSCA system using a 1/3-scaled shear link specimen was performed to demonstrate the use of and evaluate the performance of the BIM-based WSCA system. The BT strain sensors were installed on the web plate based on the findings from the FE analysis. Unfortunately, an accident happened during the test of the shear link and the test had to be halted due to premature fracture of the link specimen. An alternate test was conducted in which the link specimen (thus called stub column) was loaded axially with the two-level BT strain sensors installed on the specimen. This test demonstrates that in the WSCA system, breakage of the two BT strain sensors was successfully detected and corresponding member in the Revit model was highlighted in colors.

Based on the analysis and experimental results presented in this chapter, it is concluded that the WSCA system provides a promising rapid structural condition

assessment technology, especially for post-earthquake structural condition assessment. The WSCA system can also be used for real-time structural health monitoring of fuse members in the structure, which facilitate the implementation of the concept of resilient structure by shortening the condition assessment and thus recovery time.

Table 7- 1. EBF member sections and link properties (Richards and Uang 2006)

Story	Member sections				Link length e and (eV_p/M_p)
	Braces	Columns with link connection	Columns without link connection	Beams/Links	
1	HSS 16x16x5/8	W14x90	W14x61	W16x77	3.0 ft. (1.07)
2	HSS 14x14x5/8	W14x90	W14x61	W14x74	3.2 ft. (1.15)
3	HSS 12x12x5/8	W14x90	W14x61	W10x45	2.6 ft. (1.21)

Table 7- 2. Maximum link rotation angle (γ_a) in shear links of the prototype EBF building subjected to design basis earthquakes (DBE)

EQ Record	Shear link and corresponding maximum link rotation angle (γ_a) (unit: radians)					
	L1L	L1R	L2L	L2R	L3L	L3R
LA01	0.08	0.09	0.03	0.03	0.03	0.03
LA02	0.07	0.06	0.03	0.03	0.03	0.03
LA03	0.04	0.05	0.01	0.01	0.01	0.01
LA04	0.01	0.01	0.00	0.01	0.02	0.02
LA05	0.03	0.03	0.01	0.01	0.01	0.01
LA06	0.00	0.00	0.00	0.00	0.02	0.02
LA07	0.03	0.03	0.01	0.01	0.02	0.02
LA08	0.02	0.02	0.01	0.00	0.01	0.02
LA09	0.07	0.07	0.02	0.02	0.03	0.03
LA10	0.02	0.02	0.01	0.01	0.03	0.03
LA11	0.03	0.03	0.01	0.01	0.03	0.04
LA12	0.02	0.02	0.03	0.03	0.07	0.06
LA13	0.12	0.12	0.06	0.06	0.06	0.07
LA14	0.12	0.12	0.05	0.05	0.06	0.05
LA15	0.11	0.10	0.03	0.04	0.04	0.04
LA16	0.20	0.19	0.04	0.04	0.03	0.03
LA17	0.09	0.09	0.04	0.04	0.04	0.04
LA18	0.09	0.08	0.05	0.05	0.08	0.08
LA19	0.05	0.04	0.04	0.04	0.03	0.03
LA20	0.13	0.12	0.04	0.04	0.06	0.06
Mean	0.07	0.07	0.03	0.03	0.04	0.04
Max.	0.20	0.19	0.06	0.06	0.08	0.08

Table 7- 3. Maximum link rotation angle in shear links (γ_a) of the prototype EBF building (unit: radians) subjected to maximum credible earthquakes (MCE)

EQ record	Shear link and corresponding maximum link rotation angle (γ_a) (unit: radians)					
	L1L	L1R	L2L	L2R	L3L	L3R
LA01	0.14	0.14	0.06	0.06	0.05	0.06
LA02	0.12	0.12	0.05	0.05	0.06	0.06
LA03	0.08	0.07	0.03	0.03	0.03	0.03
LA04	0.02	0.02	0.01	0.02	0.04	0.05
LA05	0.06	0.06	0.02	0.02	0.02	0.02
LA06	0.02	0.02	0.01	0.00	0.02	0.02
LA07	0.06	0.06	0.02	0.02	0.05	0.04
LA08	0.05	0.05	0.02	0.02	0.05	0.04
LA09	0.27	0.27	0.05	0.05	0.05	0.05
LA10	0.03	0.03	0.02	0.02	0.06	0.06
LA11	0.10	0.11	0.03	0.03	0.04	0.04
LA12	0.06	0.06	0.04	0.04	0.10	0.10
LA13	0.24	0.23	0.11	0.11	0.12	0.12
LA14	0.27	0.28	0.13	0.13	0.09	0.08
LA15	0.29	0.29	0.09	0.09	0.08	0.08
LA16	0.39	0.39	0.07	0.07	0.04	0.04
LA17	0.26	0.26	0.07	0.07	0.05	0.05
LA18	0.17	0.17	0.06	0.06	0.14	0.15
LA19	0.12	0.11	0.08	0.08	0.06	0.05
LA20	0.29	0.28	0.07	0.07	0.07	0.08
Mean	0.15	0.15	0.05	0.05	0.06	0.06
Max.	0.39	0.39	0.13	0.13	0.14	0.15

Table 7- 4. Maximum link rotation angle in shear links (γ_p) of the prototype EBF building (unit: radians) subjected to DBE earthquakes

EQ record	Shear link and corresponding maximum link rotation angle (γ_p) (unit: radians)					
	L1L	L1R	L2L	L2R	L3L	L3R
LA01	0.11	0.11	0.08	0.08	0.07	0.07
LA02	0.09	0.09	0.07	0.07	0.07	0.07
LA03	0.07	0.07	0.05	0.05	0.04	0.04
LA04	0.03	0.03	0.04	0.03	0.05	0.05
LA05	0.06	0.06	0.05	0.05	0.04	0.04
LA06	0.02	0.02	0.03	0.03	0.05	0.04
LA07	0.06	0.06	0.05	0.05	0.05	0.06
LA08	0.04	0.04	0.04	0.04	0.04	0.04
LA09	0.11	0.11	0.06	0.06	0.06	0.06
LA10	0.05	0.05	0.04	0.04	0.06	0.06
LA11	0.05	0.05	0.04	0.04	0.07	0.07
LA12	0.05	0.05	0.06	0.06	0.10	0.10
LA13	0.16	0.16	0.11	0.11	0.11	0.11
LA14	0.16	0.16	0.10	0.10	0.10	0.10
LA15	0.14	0.14	0.08	0.08	0.08	0.08
LA16	0.24	0.24	0.09	0.09	0.07	0.07
LA17	0.13	0.13	0.09	0.09	0.08	0.08
LA18	0.11	0.11	0.09	0.09	0.12	0.12
LA19	0.07	0.07	0.08	0.08	0.07	0.07
LA20	0.16	0.16	0.08	0.08	0.08	0.08
Mean	0.10	0.10	0.07	0.07	0.07	0.07
Max.	0.24	0.24	0.11	0.11	0.12	0.12

Table 7- 5. Maximum chord rotation in shear links (γ_p) of the prototype EBF building subjected to MCE earthquakes

EQ record No.	Shear link and corresponding maximum link rotation angle (γ_p) (unit: radians)					
	L1L	L1R	L2L	L2R	L3L	L3R
LA01	0.16	0.16	0.11	0.11	0.10	0.10
LA02	0.15	0.15	0.10	0.09	0.10	0.10
LA03	0.11	0.11	0.06	0.06	0.07	0.07
LA04	0.04	0.04	0.05	0.05	0.07	0.07
LA05	0.09	0.09	0.07	0.07	0.05	0.05
LA06	0.04	0.04	0.04	0.04	0.05	0.05
LA07	0.08	0.09	0.06	0.06	0.08	0.08
LA08	0.09	0.09	0.06	0.06	0.08	0.08
LA09	0.33	0.33	0.11	0.11	0.09	0.09
LA10	0.06	0.06	0.05	0.05	0.09	0.09
LA11	0.15	0.15	0.06	0.07	0.08	0.08
LA12	0.09	0.09	0.08	0.08	0.14	0.14
LA13	0.28	0.28	0.16	0.16	0.16	0.16
LA14	0.32	0.32	0.19	0.19	0.13	0.13
LA15	0.35	0.35	0.14	0.14	0.12	0.12
LA16	0.44	0.44	0.13	0.13	0.08	0.08
LA17	0.30	0.30	0.12	0.12	0.10	0.10
LA18	0.22	0.22	0.10	0.10	0.19	0.19
LA19	0.14	0.14	0.13	0.13	0.10	0.10
LA20	0.35	0.35	0.13	0.13	0.11	0.11
Mean	0.19	0.19	0.10	0.10	0.10	0.10
Max.	0.44	0.44	0.19	0.19	0.19	0.19

Table 7- 6. Distance and axial deformation between the BT strain sensor (inner) attachment points when shear link rotates by 0.08 rad (unit: cm)

	$L + \Delta L$	L	ΔL	$\Delta L/L$
Case 1: 45 deg.	5.761	6.08	0.319	5.24%
Case 2: 0 deg.	6.108	6.08	0.028	0.46%
Case 3: 90 deg.	6.083	6.08	0.003	0.05%

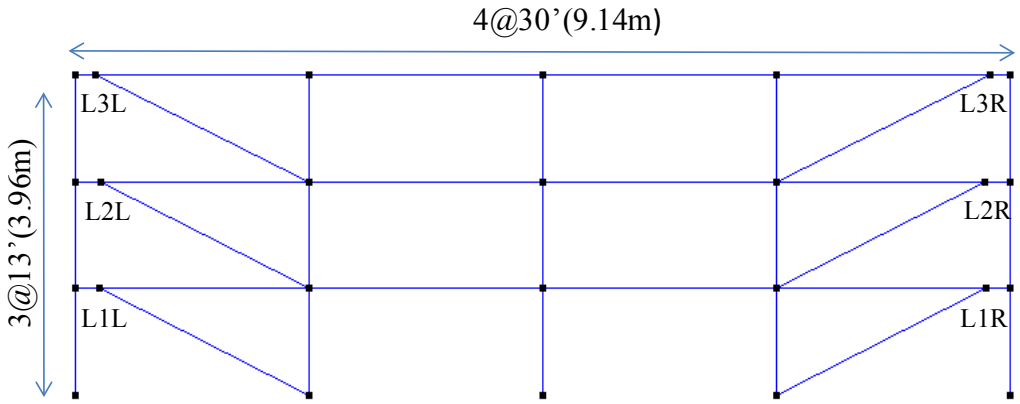

Figure 7- 1. OpenSees model of the prototype EBF structure

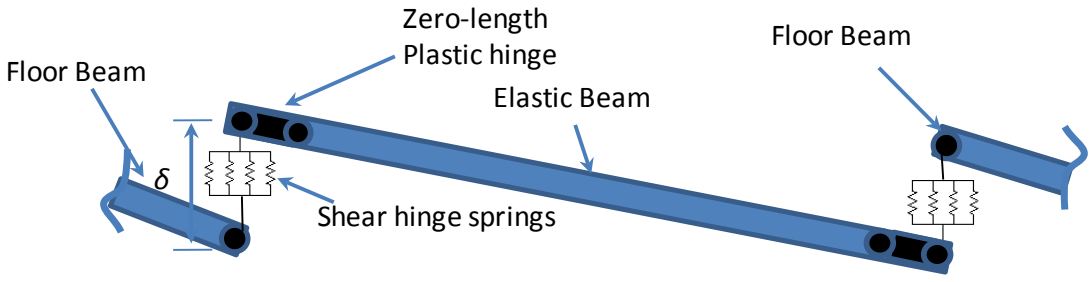

Figure 7- 2. Schematics of shear link model

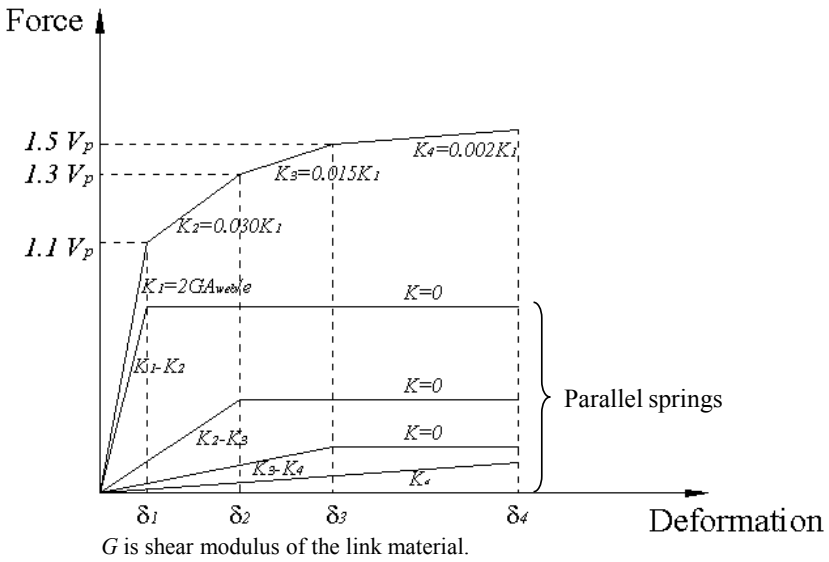

Figure 7- 3. Combined behavior of parallel springs used to model shear hinge (Richards and Uang 2006)

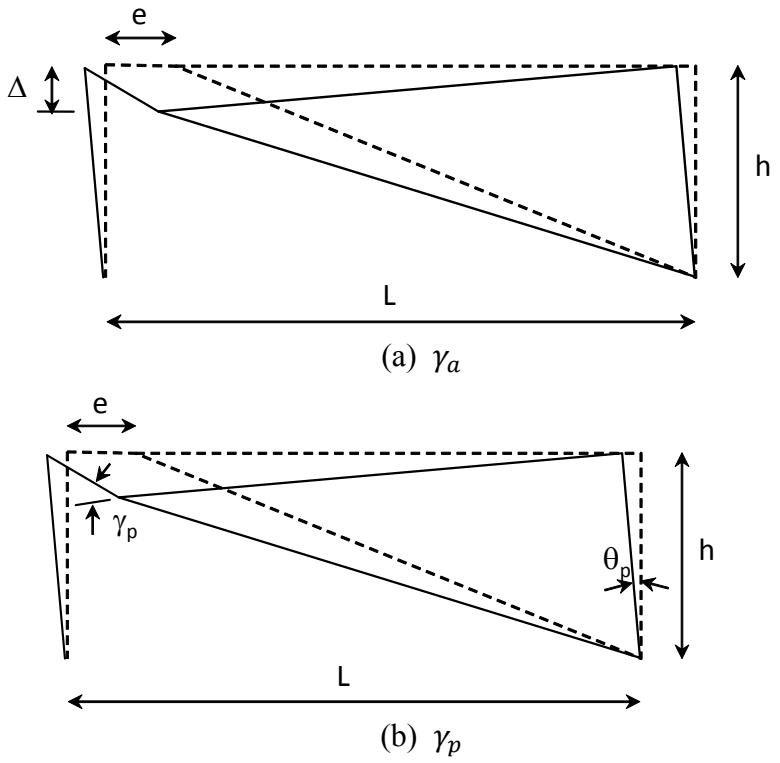

Figure 7- 4. Illustration of link rotation angle γ_a and γ_p

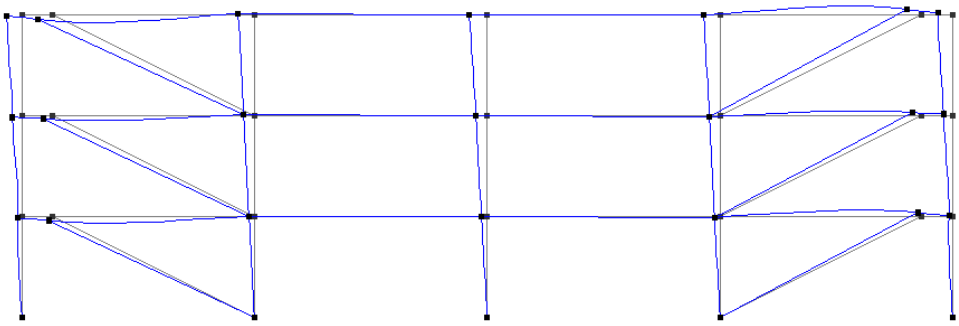

(a) 1st Mode

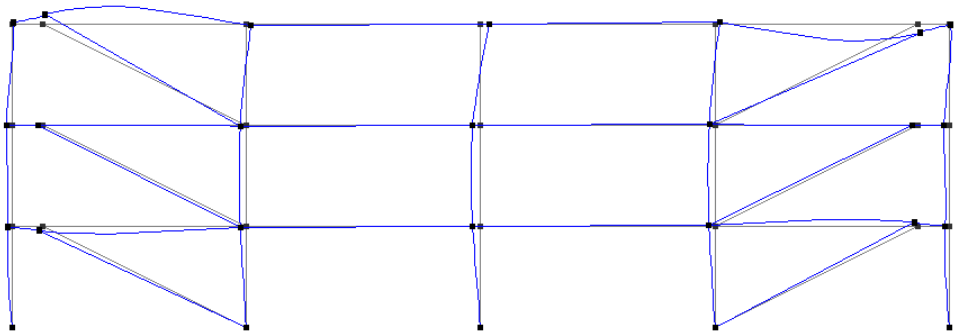

(b) 2nd Mode

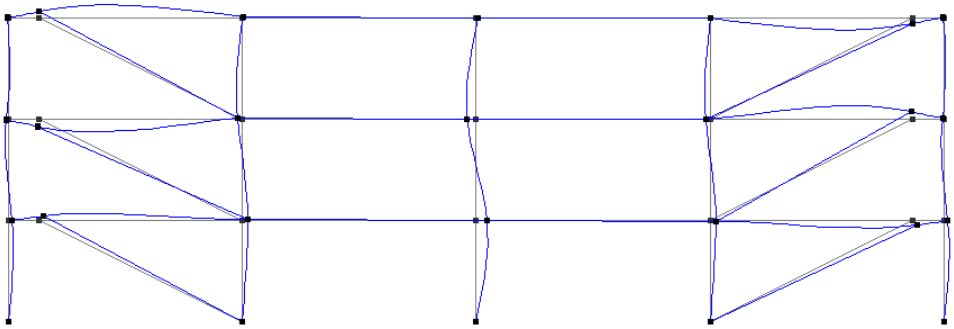

(c) 3rd Mode

Figure 7- 5. First three mode shapes of the 3-story prototype EBF building

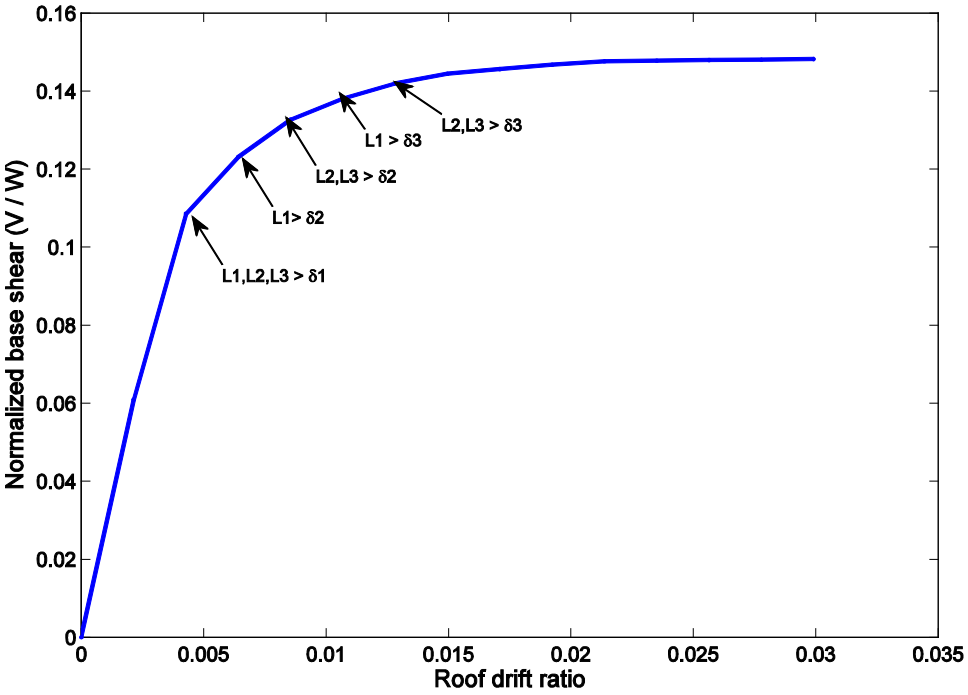

Figure 7- 6. Push-over curve of the prototype EBF building

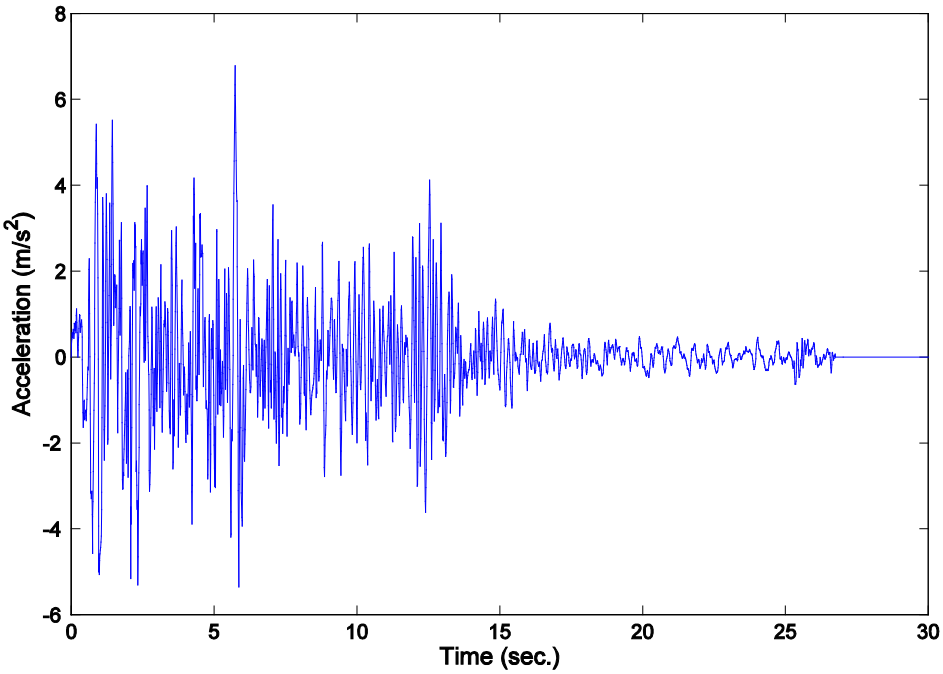

Figure 7- 7. Ground acceleration time history of the LA01 earthquake record (DBE level)

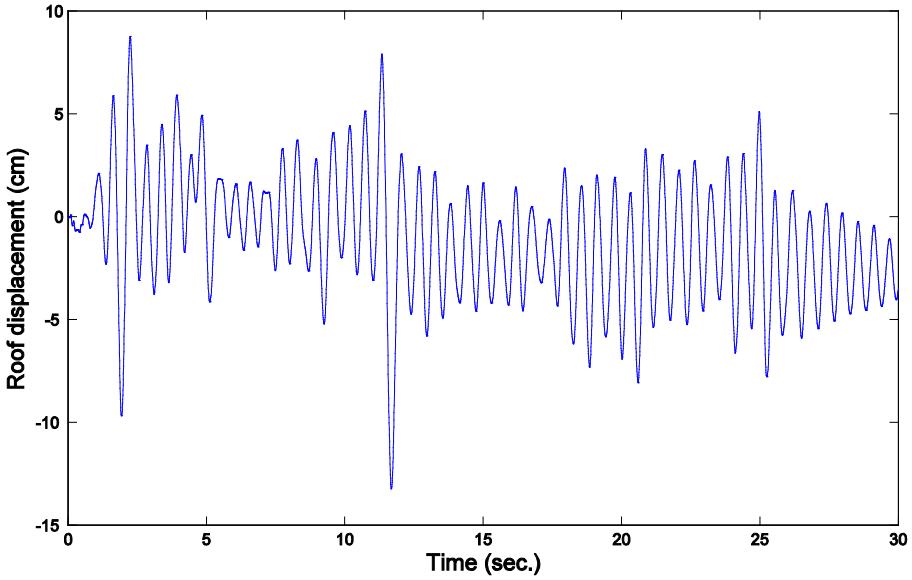

Figure 7- 8. Roof displacement time history of the prototype EBF building subjected to LA01 earthquake record (DBE level)

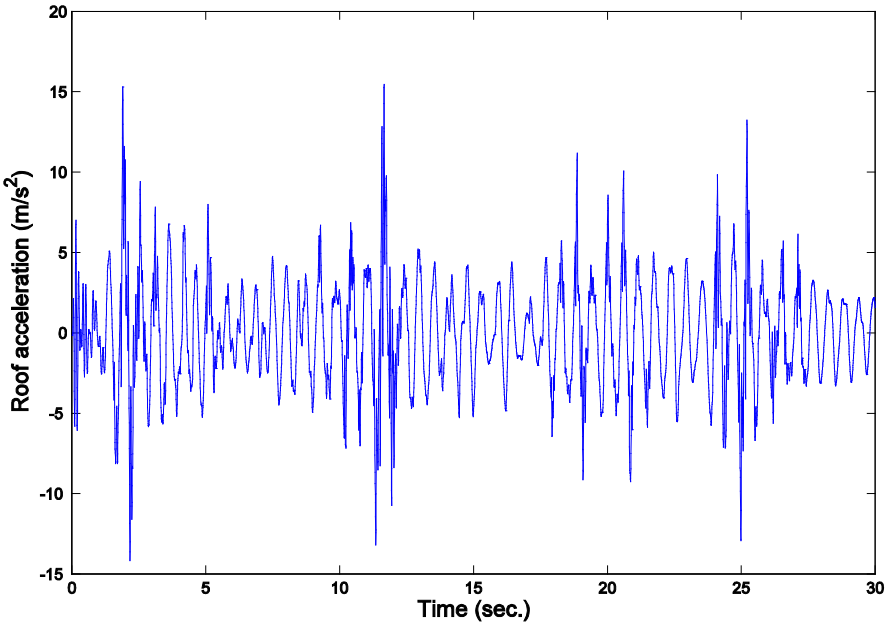

Figure 7- 9. Roof acceleration time history of the prototype EBF building subjected to LA01 earthquake record (DBE level)

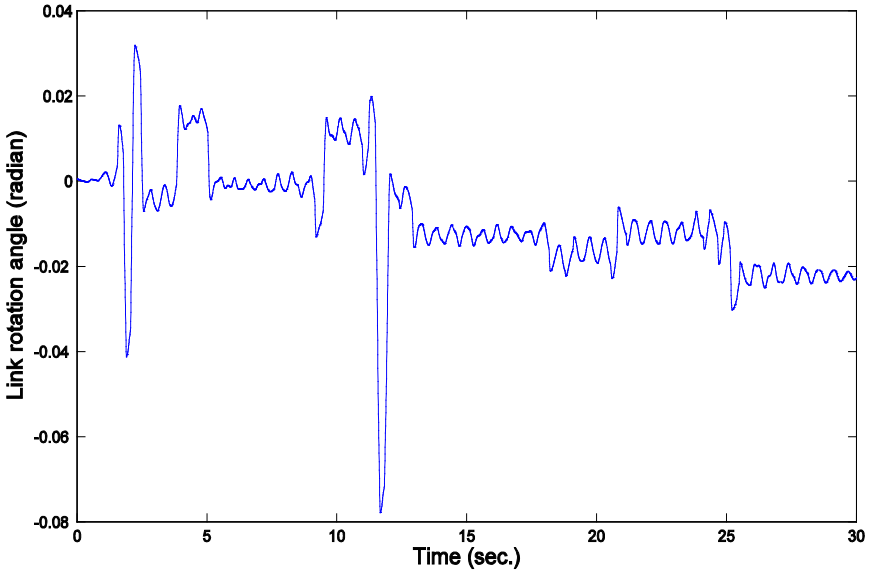

(a) L1L link rotation angle γ_a

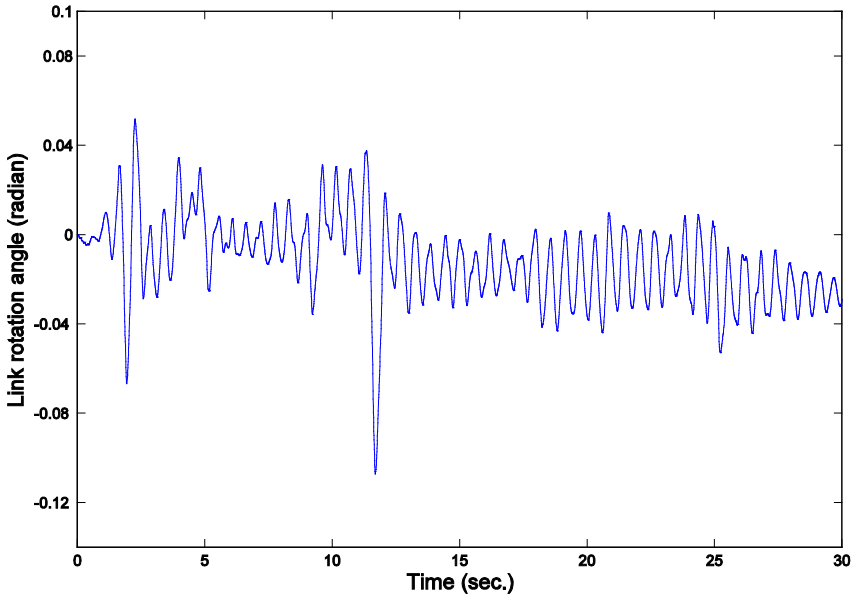

(b) L1L link rotation angle γ_p

Figure 7- 10. Typical shear link (L1L) rotation angle (γ_a and γ_p) time history of the EBF building subjected to LA01 earthquake record (DBE level)

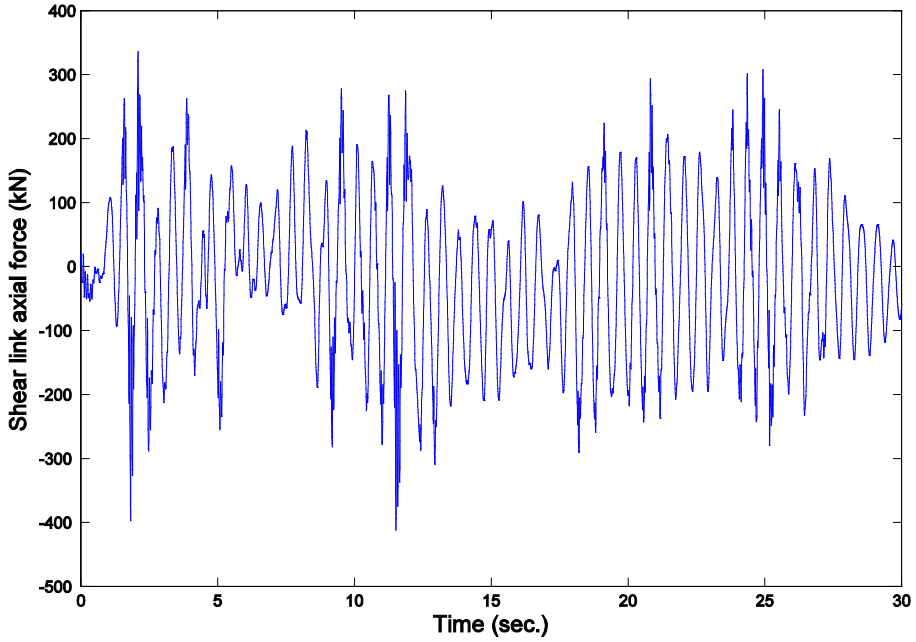

Figure 7- 11. Axial force time history of the shear link L1L in the prototype EBF building subjected to LA01 earthquake record (DBE level)

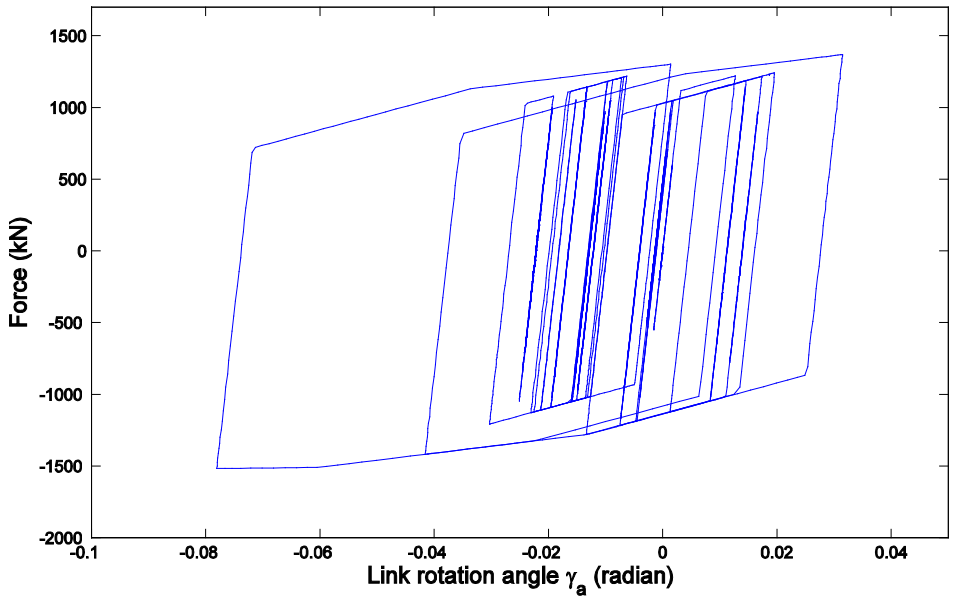

Figure 7- 12. Hysteresis (shear force vs. γ_a) loop of L1L shear link subjected to LA01 earthquake record (DBE level)

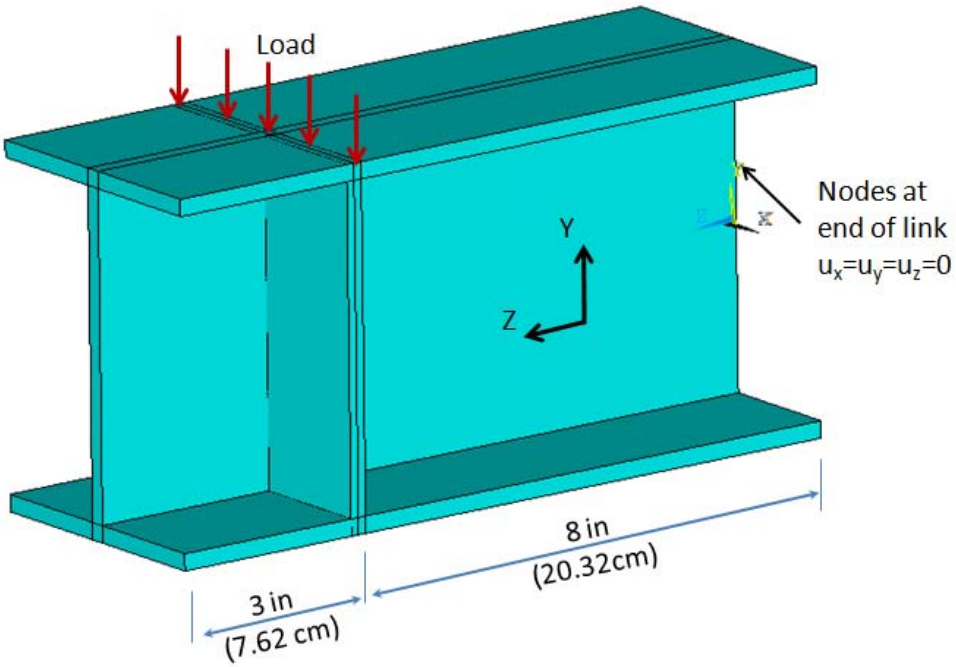

Figure 7- 13. Schematics of the FEM model of 1/3-scaled shear link in ANSYS v.13 (only part of the link is modeled; length is not 1/3 scaled to provide more space for sensor installation)

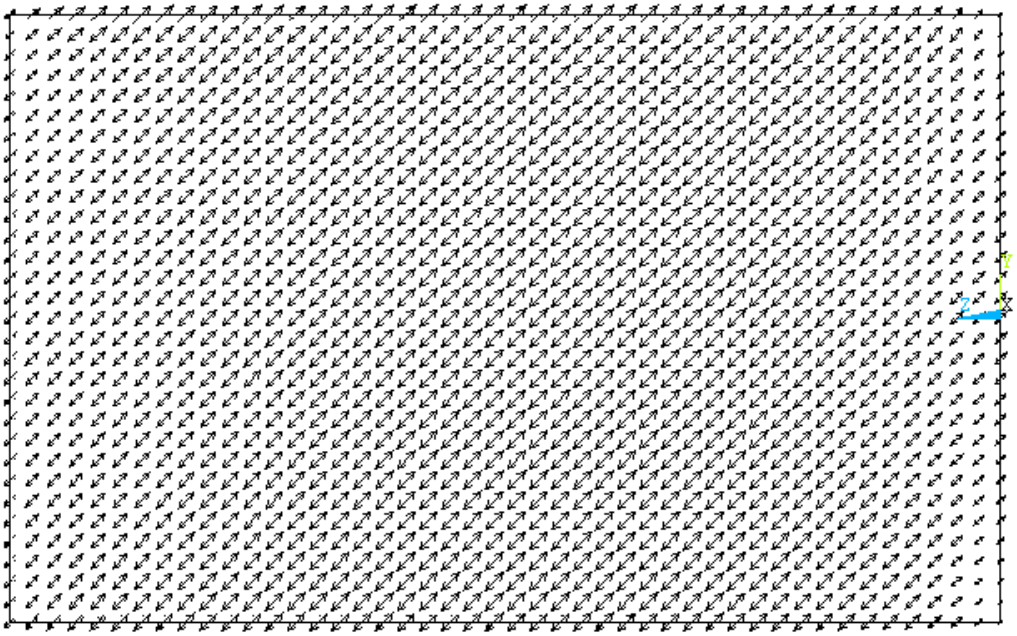

Figure 7- 14. Vector plot of first principal strain on the web at link rotation angle of 0.08 rad.

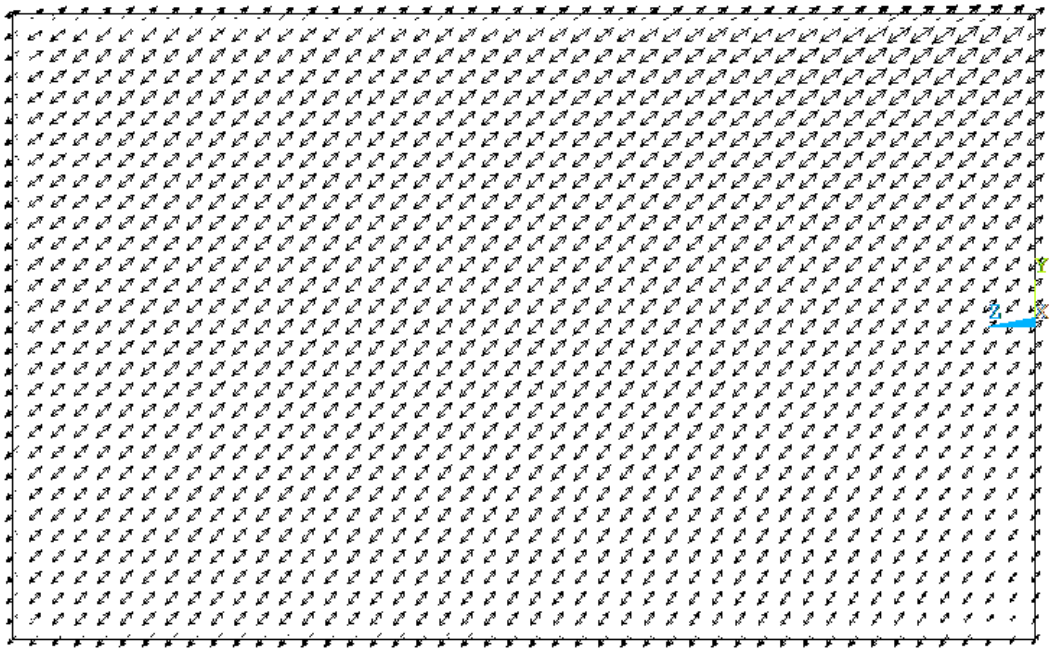

Figure 7- 15. Vector plots of first principal strain from linear elastic analysis (by applying a 1-kips load)

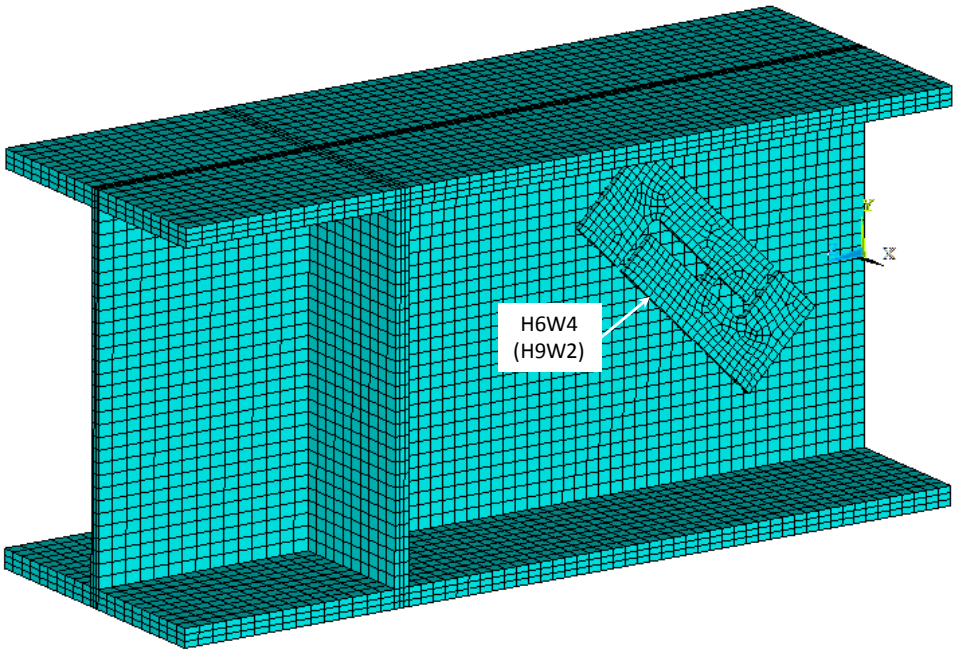

(a) Case 1: BT strain sensor oriented at 45 degree (to z axis)

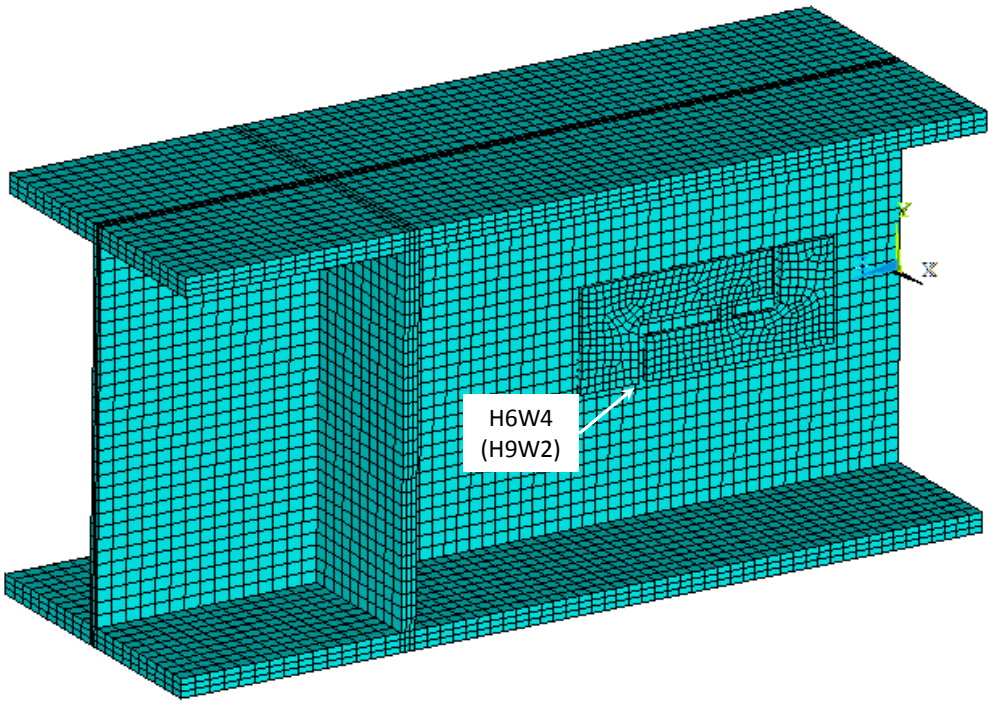

(b) Case 2: BT strain sensor oriented at zero degree

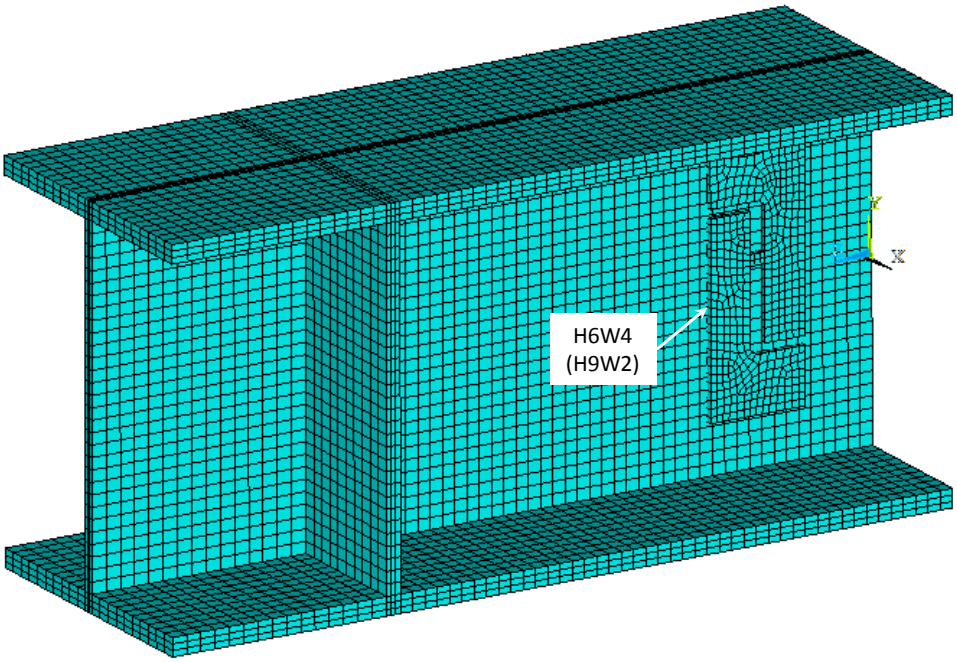

(c) Case 3: BT strain sensor oriented at 90 degree

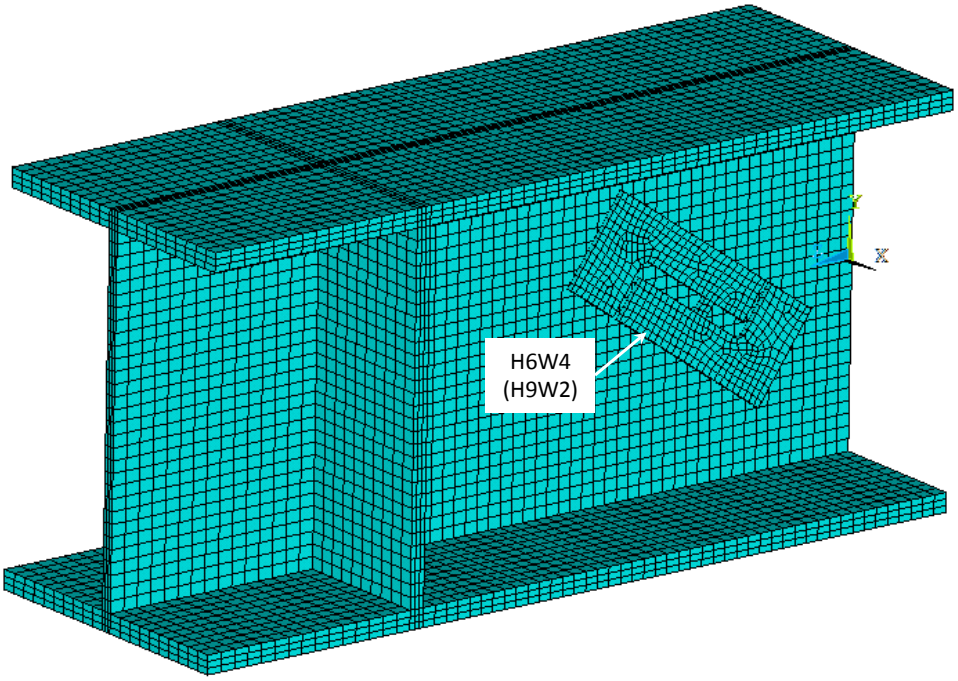

(d) Case 4: BT strain sensor oriented at 35 degree

Figure 7- 16. FEM models with integrated BT strain sensors oriented at different angles to the longitudinal axis (z axis) of shear link

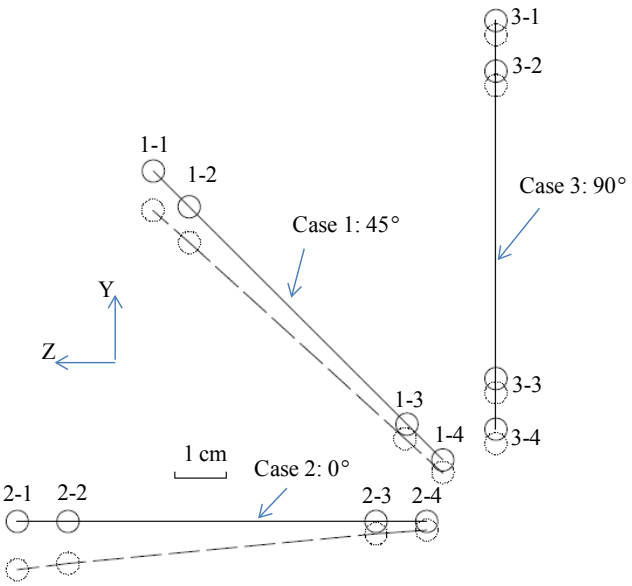

Figure 7- 17. Schematics of the BT strain sensor attachment point movement when link rotation angle changes from zero to 0.08 rad
(circles shown in figure indicates the attachment screws)

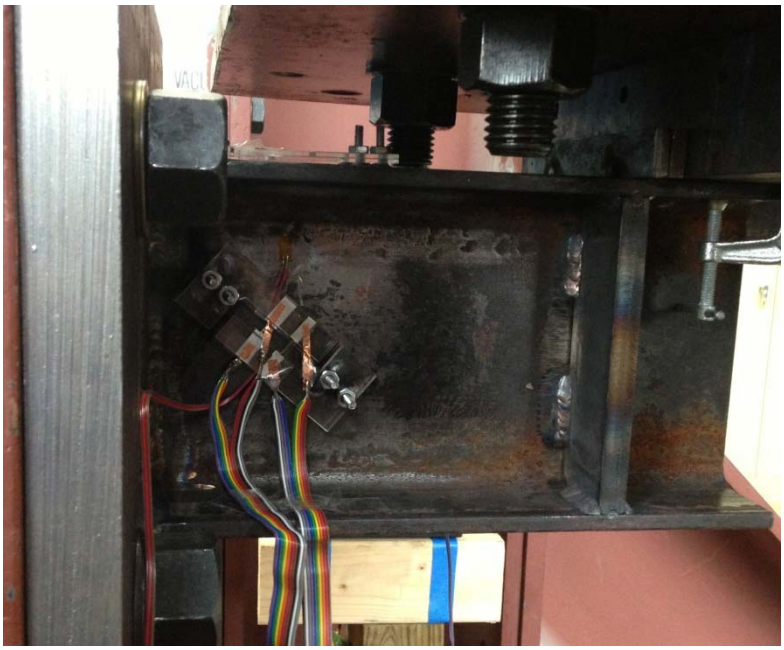

Figure 7- 18. Photo of the BT strain sensor oriented at 45 deg. on the shear link specimen web

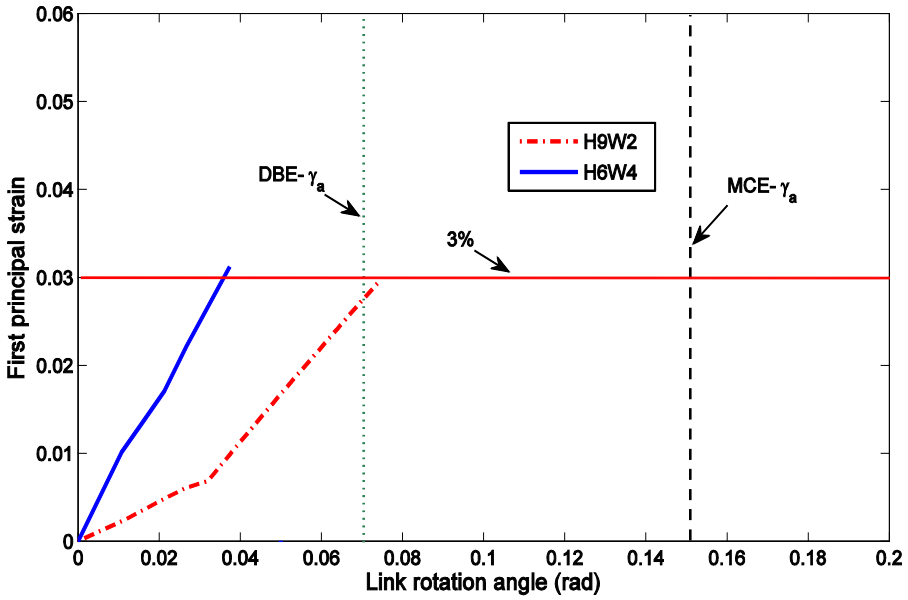

(a) Case 1: BT strain sensor oriented at 45 degree (to z axis)

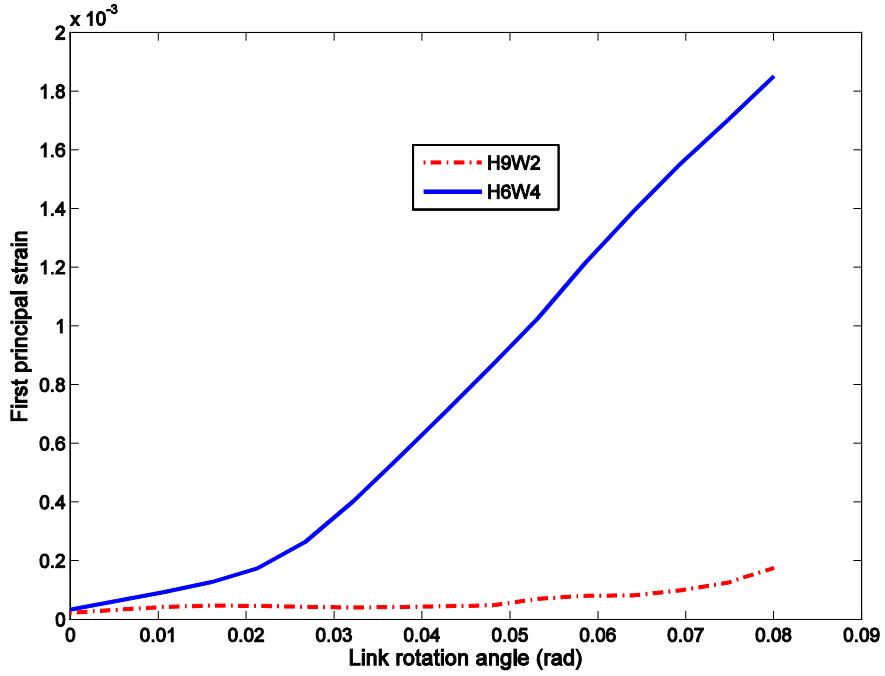

(b) Case 2: BT strain sensor oriented at 0 degree (to z axis)

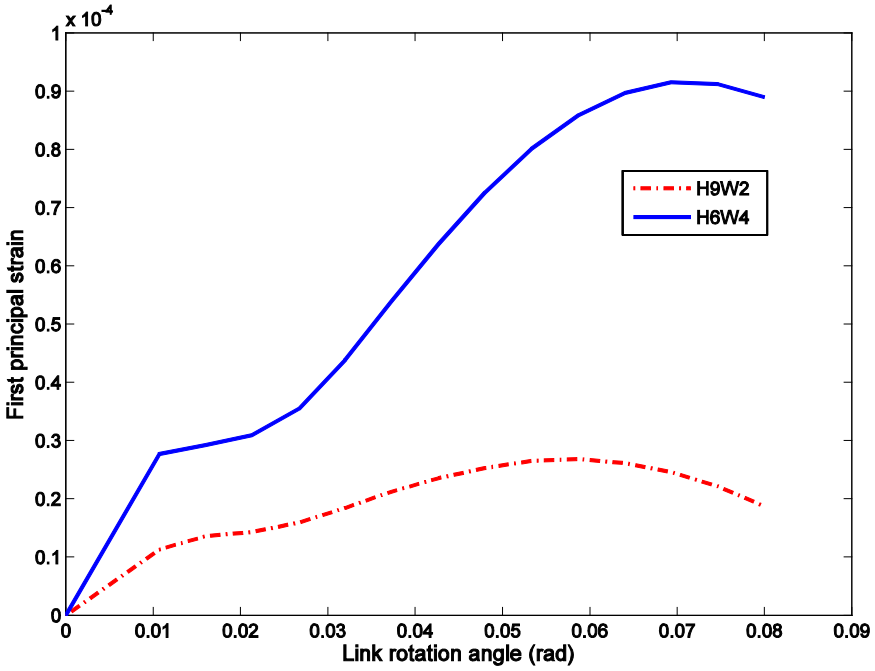

(c) Case 3: BT strain sensor oriented at 90 degree

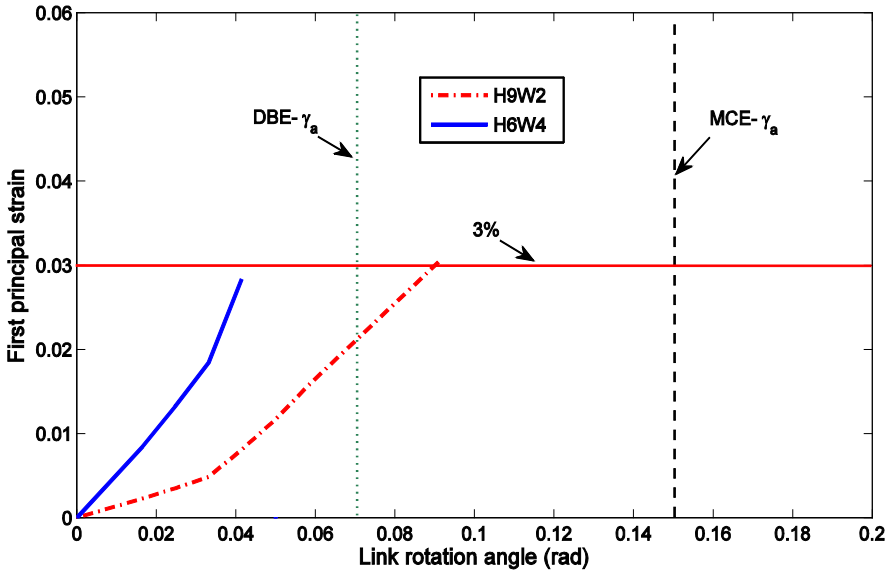

(d) Case 4: BT strain sensor oriented at 35 degree

Figure 7- 19. Evolution of maximum value of the first principal strain in the brittle bar of BT strain sensors with increasing link rotation angle (γ_a)

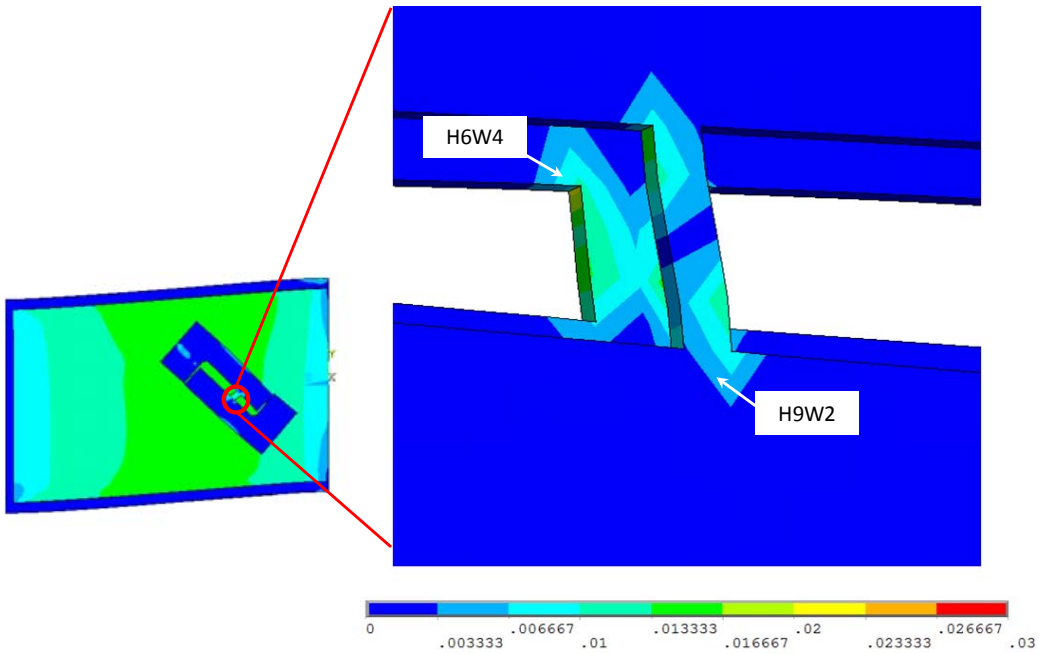

(a) Case 1: BT strain sensor oriented at 45 degree (to z axis)

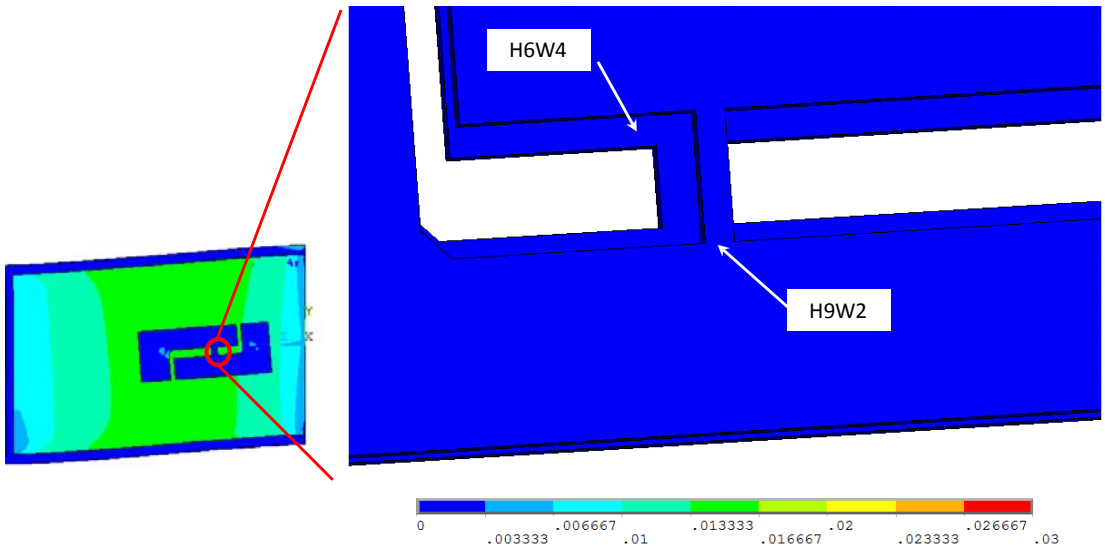

(b) Case 2: BT strain sensor oriented at 0 degree

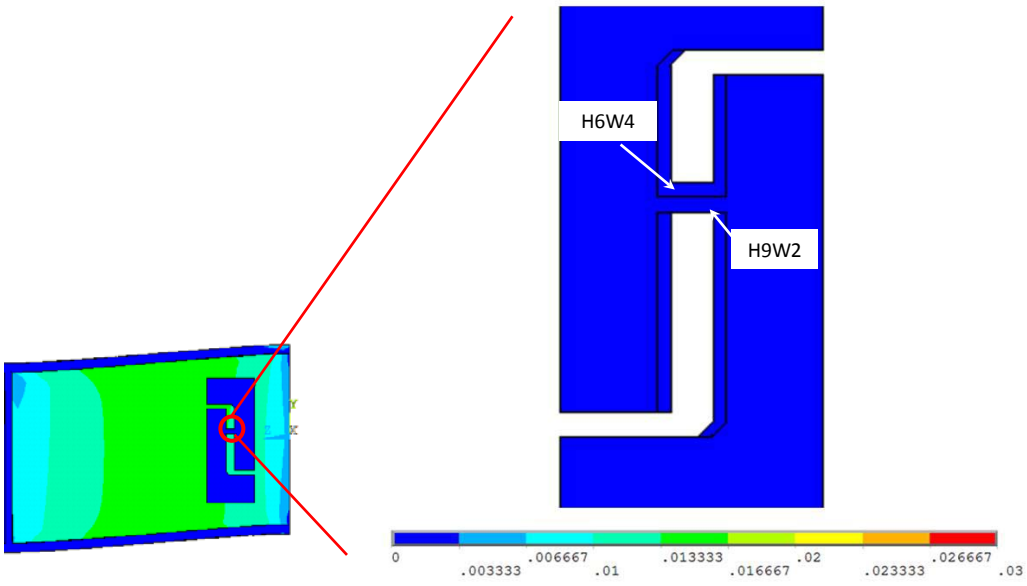

(c) Case 3: BT strain sensor oriented at 90 degree

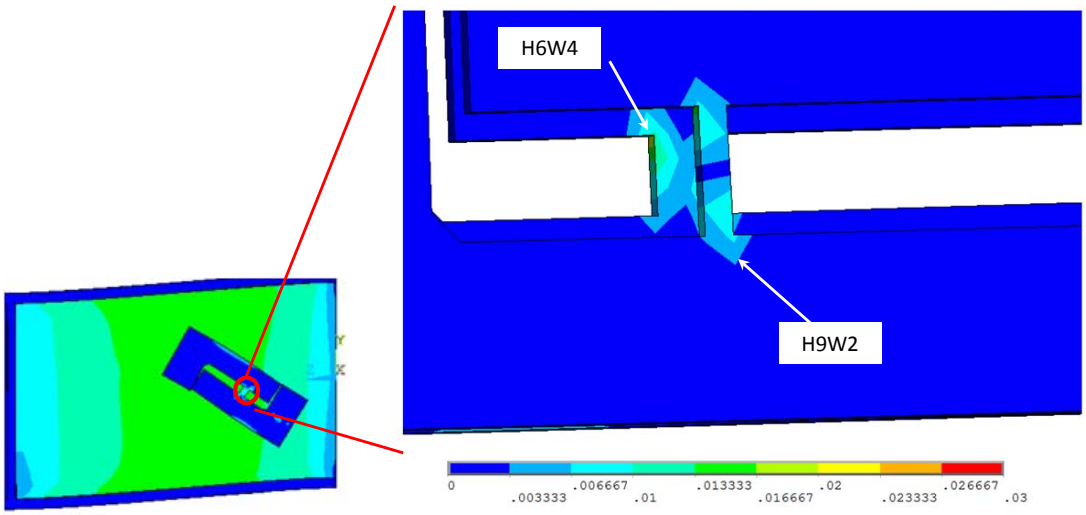

(d) Case 4: BT strain sensor oriented at 35 degree

Figure 7- 20. Contour plots of first principal strain in the BT strain sensors (with two brittle bars: H6W4 and H9W2) when link rotation angle reaches 0.03 rad.

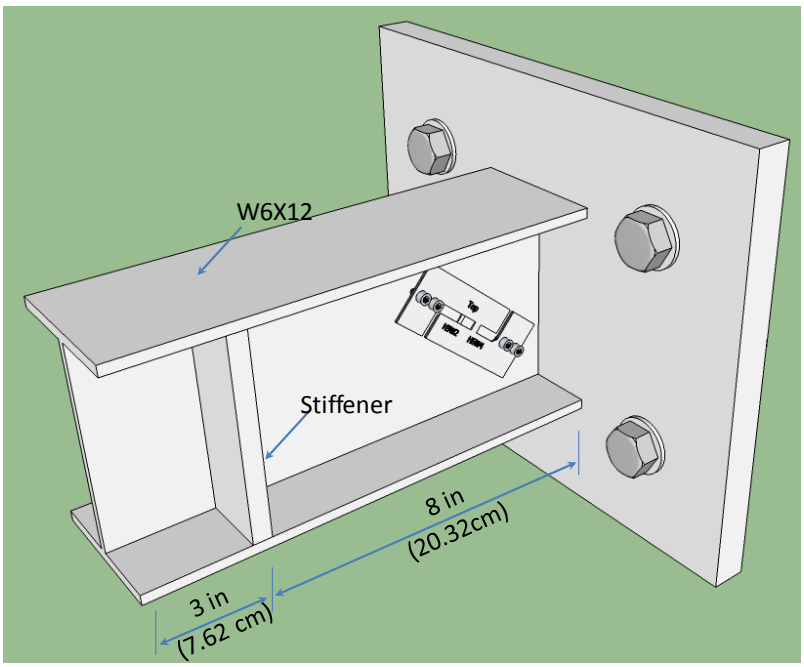

(a)

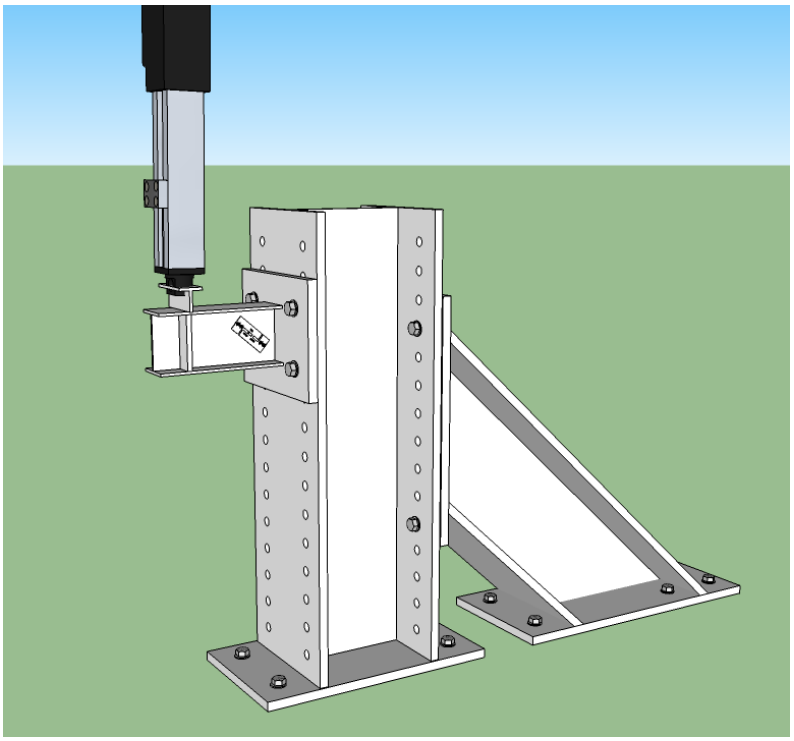

(b)

Figure 7- 21. Schematic of test setup for validating the WSCA system on shear link: (a) shear link specimen; (b) test setup with actuator and reaction frame

Figure 7- 22. Close-up view of BT strain sensor installed on shear link web

.

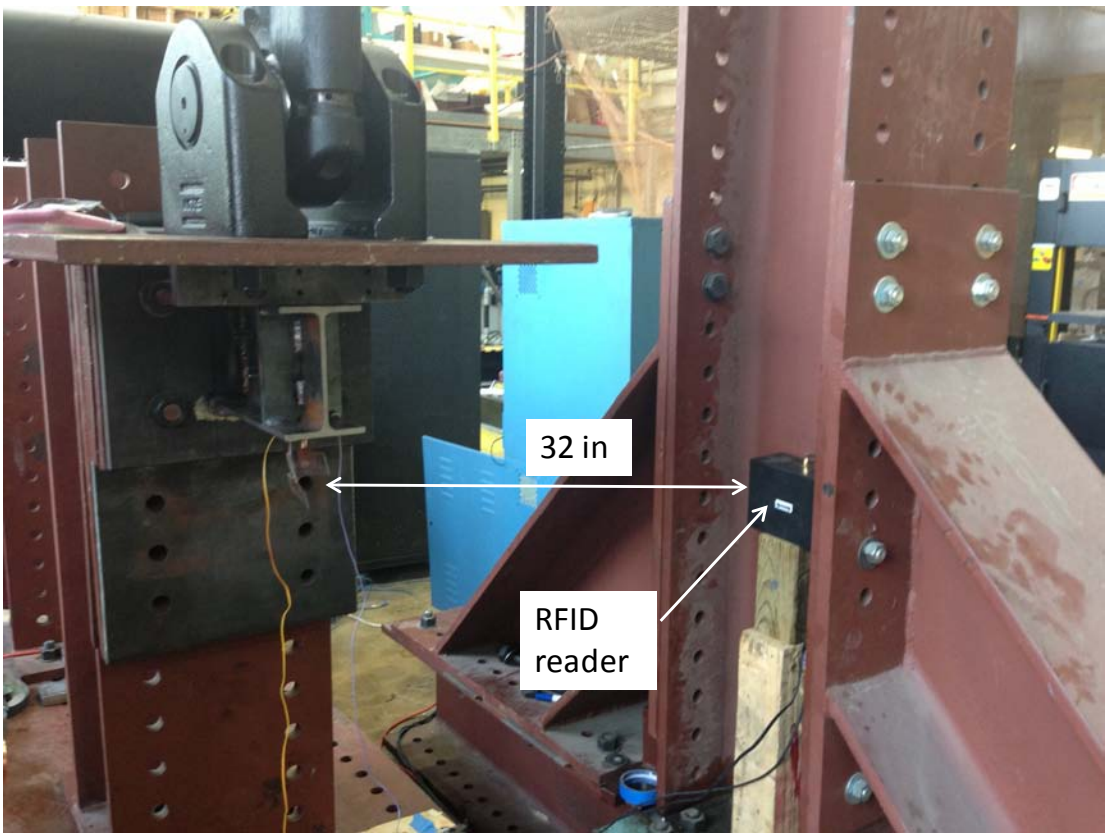

Figure 7- 23. Test setup for validating the WSCA system on shear link

Figure 7- 24. Premature failure of shear link specimen due to local flange fracture

Figure 7- 25. Test setup for compression test of stub column specimen
(legend: (1) data acquisition system user interface for strain gage measurement; (2) BIM user interface (Revit Structure); (3) RFID reader; (4) stub column specimen with BT strain sensors)

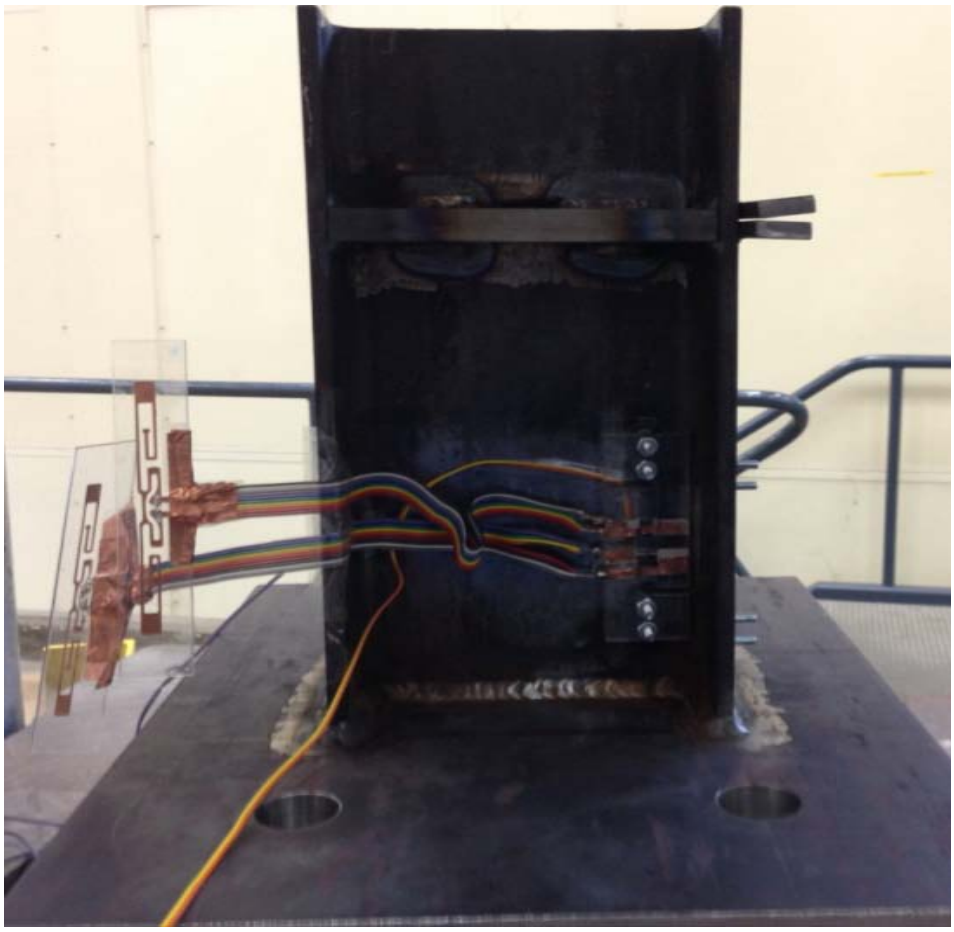

Figure 7- 26. Close-up view of BT strain sensors on stub column specimen

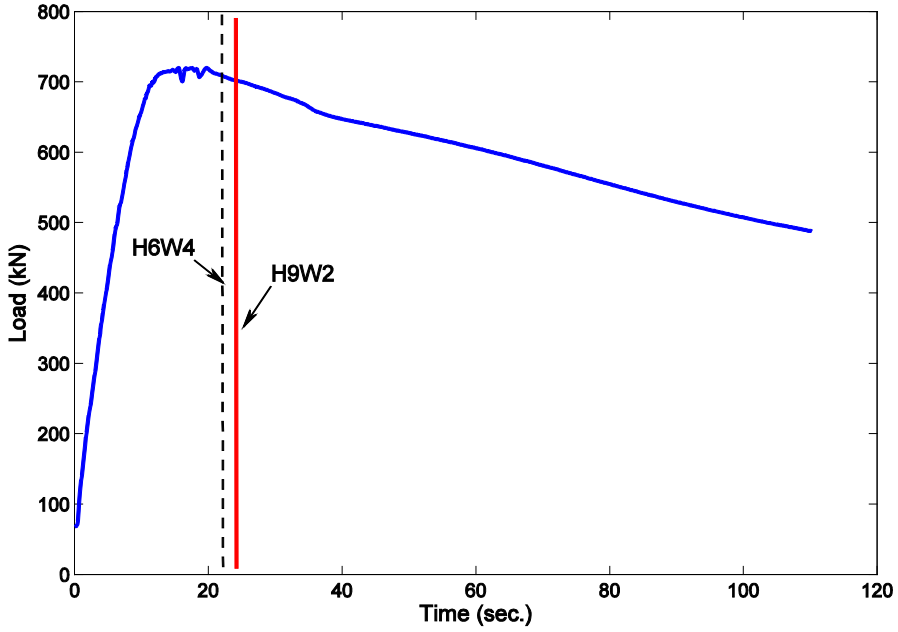

Figure 7- 27. Axial load applied to stub column specimen (vertical line indicates triggering of BT strain sensor)

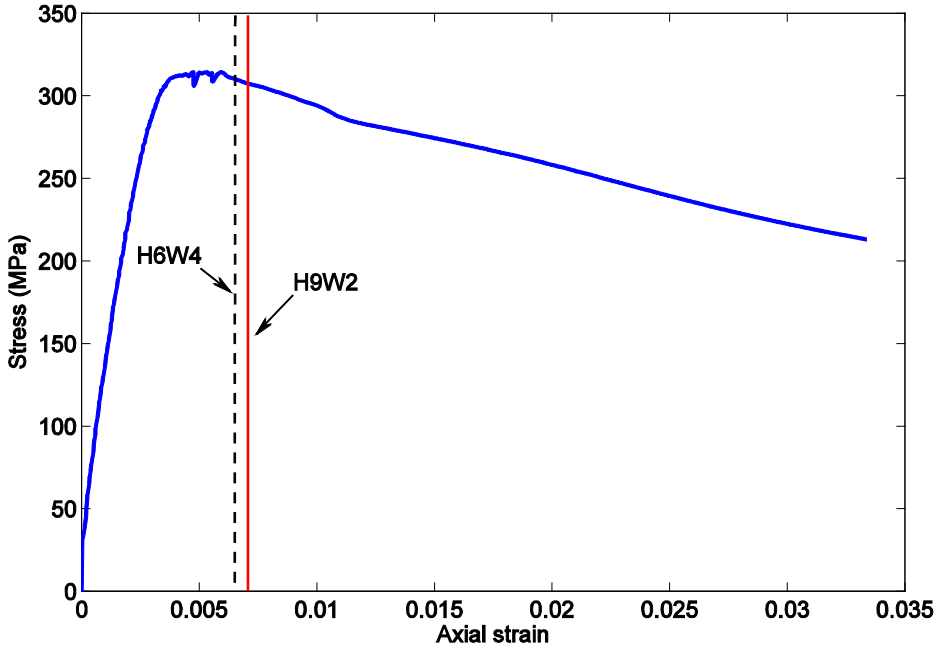

Figure 7- 28. Axial stress (load divided by cross-section area vs. strain (derived from crosshead displacement divided by stub column length) plot for stub column specimen (vertical line indicates triggering of BT strain sensor)

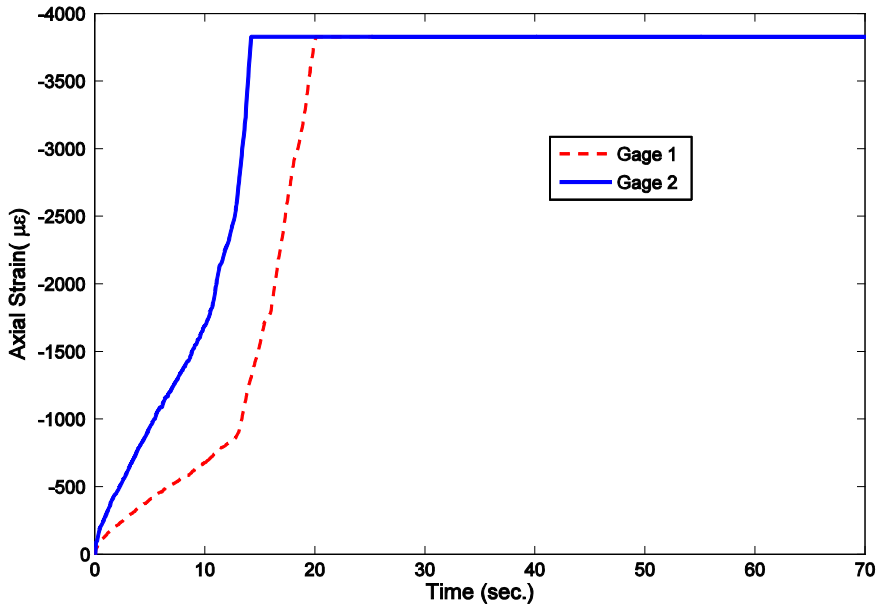

Figure 7- 29. Measured strain from two metal foil strain gages in stub column specimen

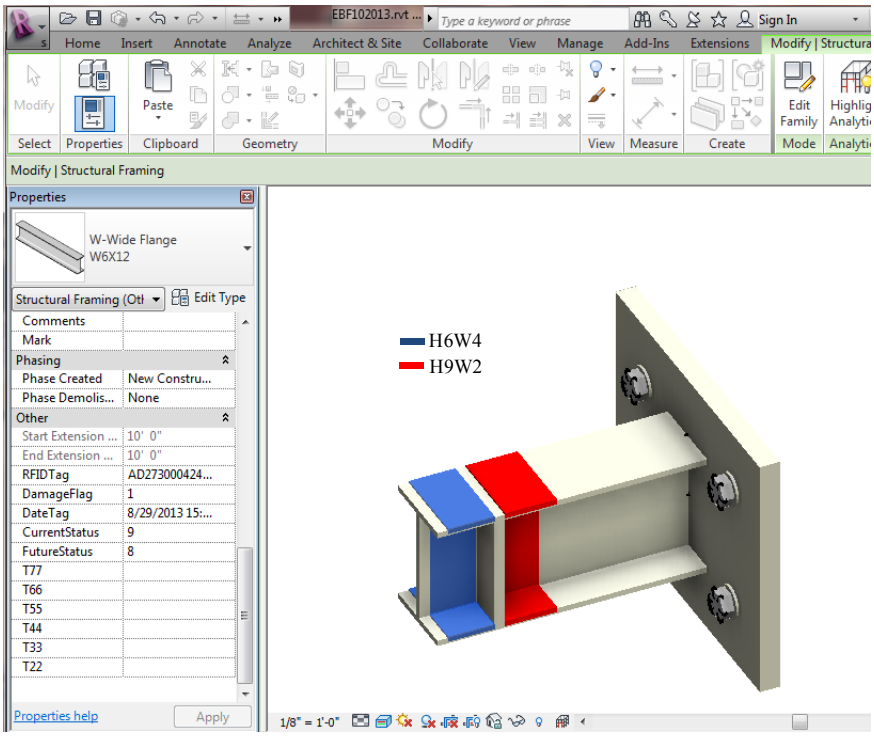

Figure 7- 30. Screen shot of BIM (Revit structure) user interface (color highlights signify the triggering of BT strain sensor)

Figure 7- 31. Photo of buckled stub column specimen

Chapter 8: Summary, Conclusions and Recommendations

8.1. Research summary

The main goal of this research is to develop a wireless structure condition assessment (WSCA) system that builds on an integrated BIM environment for an automated and graphical approach to structural condition monitoring, prognosis and health management. This WSCA system also facilitates the implementation of resilient structure concept. To achieve this goal, two major efforts have been made in this research: (1) development of a low-cost radio frequency identification (RFID) based wireless breakage-triggered strain sensor that can be interrogated on an demand basis from the BIM environment. (2) development of essential component technologies to enable the integration of BIM and structural health monitoring (SHM) technologies. A BIM for SHM portal is at the heart of this integration. A summary of specific research works performed in this study are presented as follows,

- A literature review on RFID assisted BIM technology and information exchange between BIM and SHM-related software programs was performed and the review is summarized in Chapter Two.
- A passive wireless, low-cost breakage-triggered (BT) strain sensor for detection of threshold strain level exceedence is proposed and its performance is characterized in Chapter Three. The principle of operation of the BT strain sensor and results of experimental demonstration were discussed in this chapter. Two types of brittle materials, acrylic and epoxy paint, were tested for the BT strain sensor. For important application of buckling detection in

tubular members, epoxy paint patch was investigated by compression test of paint buckets. BT strain sensors that can detect multiple threshold strain levels were also examined experimentally.

- With RFID based wireless sensors being developed in this research, a sensor-driven SHM system that integrates BIM, sensors, finite element (FE) analysis, and database technology was presented in Chapter Four. A prototype bridge model was developed using the BIM software (Revit Structures) to demonstrate sensor data storage and display, FE analysis, photorealistic visualization, prognosis, and structural condition rating in an integrated 3D visual setting.
- Chapter Five presents the concept of resilient structure design by concentrating SHM on fuse members. To demonstrate this concept of integrating SHM with resilient structure design, numerical analysis of a long-span steel arch structure subjected to earthquake excitation was conducted. This steel arch truss has strategically selected fuse zone in which structural deformation and damage could be concentrated. This strategy of concentrated damage zone will facilitate rapid structural condition assessment and this concept of focused SHM on fuse members will also be demonstrated later using the RFID based wireless strain sensor developed in this research.
- The performance of the WSCA system was tested in Chapter 6 through a hybrid simulation test conducted on a truss structure. The performance of the BT strain sensor installed on a large-scale structural tubular member was examined experimentally. The various aspects of the WSCA system including

the integration of the wireless sensors (e.g., BT strain sensors) and the BIM-based computing environment were investigated.

- In Chapter Seven, a three-story eccentrically braced frame (EBF) building was chosen as the prototype structure to demonstrate the resilient structure concept with the use of the WSCA system. An FE analysis was conducted on the prototype EBF subjected to an ensemble of 20 earthquake records in order to collect the information to guide the design of the BT strain sensor. An experimental test of the WSCA system mounted on a reduced-scaled shear link specimen was performed to demonstrate the use of and evaluate the performance of the WSCA system.

8.2. Conclusions

Based on the research findings, the following concluding remarks can be drawn,

- From the experimental results presented in Chapter 3, it is shown that by adding a bypass to the IC chip on the RFID tag, its responding power to the RFID reader would change. This feature can be utilized to detect whether a threshold strain is surpassed in the monitored structure by relating the strain to the change in the RFID antenna property.
- Two brittle materials, acrylic and epoxy paint, that were used for the BT strain sensor in this study, each have their own advantages and drawbacks. In this study, both materials have been demonstrated to break at a pre-determined threshold strain level and can be satisfactorily used for the BT strain sensor. In conjunction with the RFID technology, the BT strain sensor can fulfill the

goal of rapidly scanning the strain condition at the monitoring location and wirelessly transfer the data to BIM database at request.

- BIM can serve as an ideal 4-dimensional graphical computing environment for SHM and management practice which constantly involves considerable amounts of sensor data of different modalities. The ability to visualize the inspection and monitoring information collected in the life cycle of a structure provides engineers and decision makers with a photorealistic view of the SHM process, visualizing current condition of structural elements, structural reliability, maintenance work to schedule, response of structures under natural hazardous events such as earthquakes.
- Installing fuse members, especially self-centering members, at strategically weakened zone of steel structures can effectively control the responses of the steel structures under earthquake. The use of conventional fuse members exhibiting bilinear hysteresis results in residual displacement in the steel arch structure. Self-centering fuse members with flag-shaped hysteresis is very effective to eliminate the residual displacement. The strengths of fuse members usually have to be reduced (compared to the critical load of its original substituted member) to prevent the failure (e.g., buckling) of their neighboring members in the arch structure. The structural weakening strategy can concentrate the ductile deformation of the overall structure at favorable locations where inspection and rapid structural repair with member replacement are convenient to perform.

- RFID based BT strain sensor can be installed on the pre-defined fuse member for easy inspection. This study provides a strategy for selecting the fuse member location to form target fuse zones in steel structures.
- Through the validation test of truss member made of PVC tube, the performance of BT strain sensor for detection of preset threshold strain level was validated on a large-scale structural member. It is found that the BT strain sensor's failure mode is identical to that observed in the countertop tests reported in Chapter 3. The breakage of the brittle bar in the sensor can trigger the RFID tag connected. The WSCA system was validated through hybrid testing of a truss structure under monotonic loading. The trigger strain levels for each configuration were close to the design values. BIM user interface automatically highlighted the trigger strain level on the concerned member and displayed the updated properties of the selected member once the BT strain sensor was triggered.
- The resilient structure concept was demonstrated with the use of the WSCA system implemented on the shear link of a 3-story EBF building. It was found that the orientation of the BT strain sensor installed on the web of shear link directly affects the deformation in the BT strain sensor and thus the trigger strain level of the sensor. The link rotation angle could be related to the triggering time point of the BT strain sensor. In the experimental test, the WSCA system successfully detected the breakage of the two BT strain sensors on the web plate and highlighted the element in the BIM model with different

colors and updated the corresponding member properties of the BIM model automatically.

- The WSCA system is validated in the two experimental case studies. The custom-developed middleware program in the WSCA system exchanged and updated SHM information automatically as expected.

8.3. Recommendations for future works

This study focuses on developing a wireless structural condition assessment system integrated in BIM environment. Further research work could be conducted in the following areas,

- The BT strain sensor developed for the WSCA system has been validated in this study through experimental tests. The BT strain sensor can provide reliable strain level indication through the breakage of its brittle bar. The epoxy paint patch approach was also demonstrated to be able to detect the local buckling of tubular structure. More experiments are needed to fine tune the BT strain sensor for buckling detection.
- The current strain measurement range of the BT strain sensor can be tuned from 0.6% to 1.2%. This working range could be reduced to below 0.2% if a more brittle material can be found.
- Full scale experimental test of BT strain sensors are desired for characterizing their performance on link elements. This study used a 1/3-scaled shear link specimen but premature fracture happened due to an accident during the test. Testing of the BT strain sensors on longer links that has larger flexural deformation is also interesting to do in future study.

Bibliography

AASHTO. (2011). AASHTO Guide Manual for Bridge Element Inspection, 1st Edition, American Association of State Highway and Transportation Officials (AASHTO), Washington, DC, USA, ISBN Number: 1-56051-497-8.

AISC. (2010). Seismic Provisions for Structural Steel Buildings. ANSI/AISC 341-10. Chicago, IL, USA.

Applied Technology Council (ATC) (2013). Improvements to BIM Structural Software Interoperability. ATC-75 report. Redwood City, California, USA.

Arce, G. (2002). "Impact of higher strength steels on local buckling and overstrength of links in eccentrically braced frames." MS Thesis, Univ. of Texas at Austin, Austin, Texas, USA.

ASCE. (2010). "Minimum design loads for buildings and other structures." ASCE/SEI 7-10/ANSI, Reston, VA, USA.

Autodesk. (2011). Revit 2012 API- Developer's Guide, Autodesk, Inc., San Rafael, CA, USA.

Azhar, S. (2011). "Building information modeling (BIM): Tends, benefits, risks, and challenges for the AEC industry." *Leadership and Management in Engineering*, 11(3):241-252.

Azhar, S., Nadeem, A., Mok, J., and Leung, B. (2008). "Building information modeling (BIM): A new paradigm for visual interactive modeling and simulation for construction projects." *Proceeding of First International Conference on Construction in Developing Countries*, Karachi, Pakistan, 435–446.

Bai, L., and Zhang, Y. (2010). "Progress collapse simulation of roof truss structures with hybrid testing technique." *Proceedings of the International Association for*

Shell and Spatial Structures (IASS) Symposium 2010, November 8-12 2010, Shanghai, China.

Balanis, C. (2004). Antenna Theory: Analysis and Design, John Wiley & Sons, New Jersey, USA.

Bazjanac, V. (2004). "Virtual building environments (VBE)—Applying information modeling to buildings." URL (last accessed on Nov. 7, 2013): http://repositories.cdlib.org/lbnl/LBNL-56072.

Beck, K. (2012). "The State of Wisconsin: BIM – Digital FM handover pilot projects." *Journal of Building Information Modeling*, pp. 22 - 23.

Blandford, G. (1997). "Review of progressive failure analyses for truss structures." *J. Struct. Engrg., ASCE*, 123(2):122–129.

Butler, J., Vigliotti, A., Verdi, F., and Walsh, S. (2002). "Wireless, passive, resonant-circuit, inductively coupled, inductive strain sensor." *Sensors and Actuators A: Physical*, 102(1-2): 61–66.

Casciati, F., and Faravelli, L. (2004). "Experimental characterisation of a Cu-based shape memory alloy toward its exploitation in passive control devices." *J. Phys. IV France*, 115: 299–306.

Catbas, F., Susoy, M., and Frangopolc, D. (2008). "Structural health monitoring and reliability estimation: Long span truss bridge application with environmental monitoring data." *Engineering Structures*, 30(9): 2347–2359.

Cesare, M., Santamarina, C., Turkstra, C., and Vanmarcke, E. (1992). "Modeling bridge deterioration with Markov chains." *Journal of transportation engineering*, 118(6): 820-833.

Chen, J., Pujol, S., Yau, D., and Miao, D. (2010) "Integrated RFID and sensor networks for structural monitoring." RFID and Sensor Networks, Chapter 21, Edited by Zhang Y. *et al*., CRC Press, Florida, USA.

Chin, J., Rautenberg, J., Ma, C., Pujol, S., and Yau, D. (2009). "An experimental low-cost, low-data-rate rapid structural assessment network," *IEEE Sensors Journal*, 9(11): 1361-1369.

Christotopolulos C., Filiatrault A., and Folz B. (2002). "Seismic response of self-centering hysteretic SDOF system." *Earthquake Engineering and structural dynamics*, 31(5): 1131-1150.

Christopoulos, C., and Pampanin, S. (2004). "Towards performance based seismic design of MDOF structures with explicit consideration of residual deformations." *ISET J. Earthquake Technology*, 41(1): 53-73.

Clark, P., Aiken, I., Kasai, K., Ko, E., and Kimura, I. (1999). "Design procedures for buildings incorporating hysteretic damping devices." *Proceedings of the 68th Annual Convention*, Structural Engineers Association of California, Sacramento, CA, USA.

Crisfield, M. (1990). "A consistent co-rotational formulation for non-linear three-dimensional beam elements." *Comp. Method in Appl. Mech. & Engrg*., 81(2):131-150.

Crisfield, M., and Moita, G. (1996). "A unified co-rotational framework for solids, shells and beams." *Int. J. Solids Structures*, 33(20-22): 2969-2992.

Daliri A., Galehdar A., John S., Wang C., Towe W., and Ghorbani K. (2012) "Wireless strain measurement using circular microstrip patch antennas." *Sensors and Actuators A: Physical*, 184: 86–92.

De-Souza, R. (2000). "Force-based finite element for large displacement inelastic analysis of frames." Ph. D. Thesis, University of California, Berkeley, CA, USA.

Deavours, D. (2009). "Analysis and design of wideband passive UHF RFID tags using a circuit model." *2009 IEEE International Conference on RFID*, 283-290.

Desroches R., and Smith B. (2004). "Shape memory alloys in seismic resistant design and retrofit: a critical review of their potential and limitations." *Journal of Earthquake Engineering*, 8(3): 415-429.

Dobkin, D. (2008). The RF in RFID: Passive UHF RFID in Practice, Newnes, Burlington, MA, USA.

Dolce, M., Cardone, D., and Marnetto, R. (2000). "Implementation and testing of passive control devices based on shape memory alloys." *Earthquake engineering and structural dynamics,* 29(7):945-968.

Eastman, C., Fisher, D., Lafue, G., Lividini, J., Stoker, D., and Yessios, C. (1974). An Outline of the Building Description System, Research Report 50, Institute of Physical Planning, Carnegie Mellon Univ., Pittsburgh, USA.

Eastman, C., Jeong, Y., Sacks, R., and Kaner, I. (2010). "Exchange model and exchange object concepts for implementation of national BIM standards." *J. Comput. Civ. Eng*., 24(1): 25–34.

Eastman, C., Teicholz, P., Sacks, R., and Liston, K. (2011). BIM Handbook: A Guide to Building Information Modeling for Owners, Managers, Engineers and Contractors, 2nd Edition, John Wiley & Sons, Hoboken, New Jersey, USA.

Ellingwood, B., and Dusenberry, D. (2005). "Building design for abnormal loads and progressive collapse." *Computer-Aided Civil and Infrastructure Engineering*, 20(3): 194–205.

El-Sheikh, A. (1999). "Effect of force limiting devices on behaviour of space trusses." *Engineering Structures*, 21: 34-44.

Ergen, E., Akinci, B., and Sacks, R. (2007). "Life-cycle data management of engineered-to-order components using radio frequency identification." *Advanced Engineering Informatics*, 21(4):356-366.

Estes, A., and Frangopol, D. (2003). "Updating bridge reliability based on bridge management systems visual inspection results." *J. Bridge Eng.*, 8(6): 374-382.

Filippou, F., Popov, E., and Bertero, V. (1983). "Effects of bond deterioration on hysteretic behavior of reinforced concrete joints." Report EERC 83-19, Earthquake Engineering Research Center, University of California, Berkeley.

Filippou, F., and Fenves, G. (2004), "Methods of analysis for earthquake-resistant structures." Earthquake Engineering: From Engineering Seismology to Performance-Based Engineering, (Editors: Bozorgnia, Y. and Bertero, V.), Chapter 6, CRC Press, Boca Raton, FL., USA.

General Service Administration (GSA) (2007). "GSA's national 3D-4D BIM program." US General Services. URL (last accessed on Nov. 18, 2012): http://www.gsa.gov/bim.

Ghobarah, A., and Ramadan, T. (1990). "Effect of axial forces on the performance of links in eccentrically braced frames." *Engineering Structure*, 12(2): 106-113.

Glover, B., and Bhatt, H. (2006). RFID Essentials, O'Reilly Media, Sebastopol, CA, USA.

Golabchi, A., and Kamat, R. (2012). "Interoperability issues between different BIM software products." University of Michigan, UMCEE Report No 2012-02.

Goldberg, E. (2003), "New tools deliver BIM data-Building model yields valuable information." *Cadalyst Magazine*, Dec. 2003.

Gupta, A., and Krawinkler, H. (1999). "Prediction of seismic demands for SMRFs with ductile connections and elements." Report SAC/BD-99/06, SAC Joint Venture, Sacramento, Calif.

Harrison, M., and Parlikad, A. (2006). "Lifecycle ID and lifecycle data management." AUTO-ID Labs, AEROIDCAM-005. URL (last accessed on Nov. 1, 2013): http:// www.aero-id.org/research_reports/AEROID-CAM-005-Lifecycle.pdf.

Isikdag, U., Aouad, G., Underwood, J., and Wu, S. (2007). "Building information models: A review on storage and exchange mechanisms." *Bringing ITC Knowledge to Work, 24th W78 Conference*, Maribor.

Jia, Y., Sun, K., Agosto, F., and Quinones, M. (2006). "Design and characterization of a passive wireless strain sensor." *Meas. Sci. Technol*., 17: 2869–2876.

Jin, J., and El-Tawil, S. (2003). "Inelastic cyclic model for steel braces." *ASCE J. Engrg. Mech.*, 129(5): 548-557.

Krishnan, S. (2010). "Modified elastofiber element for steel slender column and brace modeling." *ASCE J. Struct. Engrg.*,136(11): 1350-1366.

Kurama, Y., Sause, R., Pessiki, S., and Lu, L. (1999). "Lateral load behavior and seismic design of unbonded post-tensioned precast concrete walls." *ACI Struct. J*., 96(4): 622–632.

Li, Z., Zhang, Y., and Wang, C. (2011). "A sensor-driven structural health prognosis procedure considering sensor performance degradation." *Structures and Infrastructure Engineering*, 9(8):764-776.

Light, R., and Gossard, D. (1982). "Modification of geometric models through variational geometry." *Computer Aided Design*, 14(4): 209–214.

Loh, K., Lynch, J., and Kotov, N. (2008). "Inductively coupled nanocomposite wireless strain and pH sensors." *Smart Struct. Syst*., 4(5): 531–548.

Loo, C., Klmahgoub, K., Yang, F., Elsherbeni, A., Kajfez, A., and Elsherbeni, T. (2008). "Chip impedance matching for UHF RFID tag antenna design." *Progress In Electromagnetics Research*, PIER 81, 359–370.

Lynch, J., and Loh, K., (2006). “A summary review of wireless sensors and sensor networks for structural health monitoring.” *Shock Vib. Dig.*, 38(2): 91–128.

Mahin, S., Sakai, J., and Jeong, H. (2006). “Use of partially prestressed reinforced concrete columns to reduce post-earthquake residual displacements of bridges.” *Proc., 5th National Seismic Conf. on Bridges & Highways*, San Francisco, CA, USA.

Mansour, N., Shen, Y., Christopoulos, C., and Tremblay, R. (2008). “Seismic design of EBF steel frames using replaceable nonlinear links.” *Proc. 14th World Conference on Earthquake Engineering*, Beijing, China.

Mazzoni, S., McKenna, F., Scott, M., and Fenves, G. (2009). "The Open System for Earthquake Engineering Simulation (OpenSees) user command-language manual." Pacific Earthquake Eng. Research Center, Univ. Calif., Berkeley, CA. URL (last accessed on Nov. 7, 2013): http://opensees.berkeley.edu.

McKenna, F. (1997). “Object-oriented finite element programming: frameworks for analysis, algorithms and parallel computing.” Ph.D. Thesis, University of California, Berkeley, CA, United States.

McKenna, F., and Fenves, G. (2005). “Open system for earthquake engineering simulation.” Pacific earthquake engineering research center (PEER), Berkeley, California.

Menegotto, M., and Pinto, P. (1973). “Method of analysis of cyclically loaded RC plane frames including changes in geometry and non-elastic behavior of elements under normal force and bending, Preliminary Report.” *IABSE*, 13: 15-22.

Miller, D., Fahnestock, L., and Eatherton, M. (2011). “Self-centering buckling-restrained braces for advanced seismic performance.” *ASCE Structures Congress 2011*, Las Vegas, Nevada, USA.

Moghaddasi-B., N. (2011). "Performance evaluation of two new seismic resistant diagrid framing systems." Ph.D. Thesis, University of Maryland, College Park, MD, United States.

Morita, K., and Noguchi, K. (2006). "Crack detection methods using radio frequency identification and electrically conductive material." *Technical Memorandum of Public Works Research Institute*, No. 4022, Page 88.

Mosalam, K., Talaat, M., and Park, S. (2008). "Modeling progressive collapse & reinforced concrete framed structures." *Proc. 14th World Conference on Earthquake Engineering*, Beijing, China.

Motamedi, A., and Hammad, A. (2009). "Lifecycle management of facilities components using radio frequency identification and building information model." *Journal of Information Technology in Construction (ITcon)*, 14: 238-262.

NBIMS. (2007). United States national building information modeling standard version 1—Part 1: Overview, principles, and methodologies, US National Institute of Building Science Facilities Information Council, BIM committee. URL (last accessed on Nov. 7, 2013): (http://www.wbdg.org/pdfs/NBIMSv1_p1.pdf.

Neuenhofer, A., and Filippou, F. (1997). "Evaluation of nonlinear frame finite element models." *Journal of Structural Engineering, ASCE*, 123(7): 958-966.

Neuenhofer, A., and Filippou, F. (1998). "A geometrically nonlinear flexibility-based frame finite element model." *Journal of Structural Engineering, ASCE*, 124(6): 704-711.

Nikitin, P., and Rao, K. (2006). "Theory and measurement of backscattering from RFID tags." *IEEE antennas and Propagation Magazine*, 48(6): 212-218.

NXP Semiconductors. (2008). "An 1629 UHF RFID label antenna design-UHF anten na design." Application note, Rev. 1.0, NXP B.V., 2008. URL (last accessed on Nov. 7, 2013): http://www.nxp.com/documents/application_note/AN162910.pdf.

Okazaki, T., Engelhardt, M., Nakashima, M., and Suita, K. (2006). "Experimental performance of link-to-column connections in eccentrically braced frames." *J. Struct. Eng., ASCE*, 132(8): 1201-1211.

Pablo, R. (2009). "Risk assessment of highway bridges: a reliability-based approach." *The Technology Interface Journal*, 10(2).

Pampanin, S., Christopoulos, C., and Priestley, M. (2003). "Performance-based seismic response of frame structures including residual deformations. Part II: Multidegree-of-freedom systems." *J. Earthquake Eng.*, 7(1): 119–147.

Popov, E., and Engelhardt, M. (1988). "Seismic Eccentrically Braced Frames." *J. of Construction Steel Research*, 10: 321-354.

Pratt, M. (1993). "Geometric methods for computer-aided design." Fundamental Developments of Computer-aided Geometric Modeling, L. Piegl, ed., Academic Press, London, 271–320.

Ramadan, T., and Ghobarah, A. (1995). "Analytical model for shear-link behavior." *J. Struct. Eng., ASCE*, 121(11): 1574-1580.

Rankine, W. (1857). "On the stability of loose earth." *Philosophical Transactions of the Royal Society of London*, Vol. 147.

Rao, K., Nikitin, P., and Lam, S. (2005). "Antenna design for UHF RFID tags: a review and a practical application." *IEEE Transactions on Antennas and Propagation*, 53(12): 3870-3876.

Rehm, K. (2013). "Bridge inspection: primary element." Roads & Bridges, May 6, 20 13. URL (last accessed on October 24, 2013): http://www.roadsbridges.com/bridge -inspection-primary-element.

Reinhorn, A., Viti, S., and Cimellaro, G. (2005), "Retrofit of structures: strength reduction with damping enhancement." *Proceedings of the 37th UJNR Panel Meeting on Wind and Seismic Effects*, 16-21 May, Tsukuba, Japan.

Richards, P., and Uang, C. (2006). "Testing protocol for short links in eccentrically braced frames." *J. Struct. Eng. ASCE*, 132(8): 1183-1191.

Ricles, J., and Popov, E. (1987). "Dynamic analysis of seismically resistant eccentrically braced frames." Report No. VCBIEERC-87107, Earthquake Engrg. Res. Ctr., Univ. of California, Berkeley, California.

Ricles, J., Sause, R., Garlock, M., and Zhao, C. (2001). "Post-Tensioned seismic resistant connections for steel frames." *Journal of Structural Eng.*, *ASCE*, 127(2): 113-121.

Ruiz-Garcia, J., and Miranda, E. (2006a) "Evaluation of residual drift demands in regular multi-storey frames for performance-based seismic assessment." *Earthquake Engineering and Structural Dynamics*, 35(13): 1609-1629.

Ruiz-Garcia, J., and Miranda, E. (2006b) "Residual displacement ratios for assessment of existing structures." *Earthquake Engineering and Structural Dynamics*, 35(3): 315-336.

Schellenberg, A., and Mahin, S. (2006a) "Application of an experimental software framework to hybrid simulation of structures through collapse." *First European Conference on Earthquake Engineering and Seismology*, Geneva, Switzerland.

Schellenberg, A., Mahin, S., and Fenves, G. (2006b) "Application of an experimental software framework for international hybrid simulation." *4Th international conference on earthquake engineering*, Taipei.

Schellenberg, A., Kim, H., Mahin, S., and Fenves, G. (2008) "Environment independent implementation of a software framework for fast local and geographically distributed hybrid simulations." *The 14th World Conference on Earthquake Engineering*, Beijing, China.

Schellenberg, A., Mahin, S., and Fenves, G. (2009) "Advanced implementation of hybrid simulation." PEER report 2009/104, University of California at Berkeley, CA, USA.

Scott, M., and Fenves, G. (2010). "Krylov subspace accelerated Newton algorithm: applicationto dynamic progressive collapse simulation of frames." *ASCE Journal of Structural Engineering*, 136(5): 473-480.

Seo, C., and Sause, R. (2005) "Ductility demands on self-centering systems under earthquake loading." *ACI Structural Journal*, 102(2): 275-285.

Shepard, S. (2005). RFID: Radio Frequency Identification. McGraw-Hill, New York, USA.

Singh, V., Gu, N., and Wang, X. (2011). "A theoretical framework of a BIM-based multi-disciplinary collaboration platform." *Autom. Constr.*, 20(2): 134–144.

Skyetek (2012). SkyeModule M9 datasheet, Version 081313, Skyetek Inc., Denver, Colorado, USA.

Somerville, P., Smith, N., Punyamurthula, S., and Sun, J. (1997). "Development of ground motion time histories for phase 2 of the FEMA/SAC steel project." SAC/BD-97/04, SAC Joint Venture, Sacramento, CA, USA.

Song, G., Ma, N., and Li, H. (2006). "Applications of shape memory alloys in civil structures." *Engineering Structures*, 28(9):1266-1274.

Spacone, E., Ciampi, V., and Filippou, F. (1996). "Mixed formulation of nonlinear beam finite element." *Comput. Struct*., 58(1):71–83.

Susoy, M., Catbas, F., and Frangopol, D. (2008). "Evaluation of time-variant bridge reliability using structural health monitoring." *Proc. IMAC XXVI Conference & Exposition on Structural Dynamics - Technologies for Civil Structures*, Orlando, FL, USA.

Tada, M., and Suito, A. (1998). "Static and dynamic post-buckling behavior of truss structures." *Engineering Structures*, 20(4-6): 384-389.

Uang, C., and Nakashima, M. (2003). “Steel buckling-restrained braced frames.” Chapter 16 in Earthquake Engineering: Recent Advances and Applications, CRC Press, Boca Raton, FL.

Uriz, P., Filippou, F., and Mahin, S. (2008). “Model for cyclic inelastic buckling of steel braces.” *ASCE J. Struct. Engrg.*, 134(4): 619-628.

Van-Nederveen, G., and Tolman, F. (1992). "Modelling multiple views on buildings." *Automation in Construction,* 1(3): 215–224.

Viti, S., Cimellaro, G., and Reinhofrm A. (2006). “Retrofit of a hospital through strength reduction and enhanced damping.” *Smart Structures and Systems*, 2(4): 339-355.

Wang, T., McCormick, J., Yoshitake, N., Pan, P., Murata, Y., and Nakashima, M. (2009). “Collapse simulation of a four-story steel moment frame by a distributed online hybrid test.” *Earthquake Engrg. Struct. Dyn*., 37(6):955–974.

Wikipedia. (2013). Building Information Modeling, web link. URL (last accessed on October 31, 2013): http://en.wikipedia.org/wiki/Building_information_modeling.

Wong, A., Wong, F., and Nadeem, A. (2011) “Government roles in implementing building information modeling systems: Comparison between Hong Kong and the United States.” *Construction Innovation: Information, Process, Management*, 11(1): 61 – 76.

Yi, X., Wu, T., Wang, Y., Leon, R., Tentzeris, M., and Lantz, G. (2011). “Passive wireless smart-skin sensor using RFID-based folded patch antennas.” *International Journal of Smart and Nano Materials*, 2(1): 22-38.

Yi, X., Cho, C., Cooper, J., Wang, Y., Tentzeris, M., and Leon, R. (2013). “Passive wireless antenna sensor for strain and crack sensing - electromagnetic modeling, simulation, and testing.” *Smart Materials and Structures*, 22(8).

Zareian, F., and Medina, R. (2010). “A practical method for proper modeling of structural damping in inelastic plane structural systems.” *Computers & Structures*, 88(1-2): 45-53.

Zhu, S. and Zhang, Y. (2008). "Seismic analysis of concentrically braced frame systems with self-centering friction damping braces." *ASCE Journal of Structural Engineering*, 134(1): 121-131.